Poly-(methacrylic acid) brush silica nano-particles: Synthesis and application in analytical science

By

Marcello Iacono B.Sc.

Supervisor: Dr. Andreas Heise

A thesis submitted to Dublin City University

in fulfillment of the requirements

for the degree of

Doctor of Philosophy (PhD)

November 2014

Declaration

I hereby certify that this material, which I now submit for assessment on the programme of study leading to the award of a degree of Doctor of Philosophy is entirely my own work, and that I have exercised reasonable care to ensure that the work is original, and does not to the best of my knowledge breach any law of copyright, and has not been taken from the work of others save and to the extent that such work has been cited and acknowledged within the text of my work.

Signed: _____ (Candidate) ID No.: 59119608

Date: _____

Acknowledgement

It is with immense gratitude that I acknowledge the support and help of my supervisor, Dr. Andreas Heise. First of all, he gave me the possibility to realize a huge dream and he gave me the possibility to do my first steps in the fascinating world of the scientific research. During my work in the DCU campus and in the Chemistry department, a number of persons gave me a very strong daily support both on the research technical aspects and on the human point of view. In particular I would like to thank all of the technical staff Veronica; Brendan who gave me a great help with SEM transferred to me all the experience have now in the electronic microscopy and Mary – very helpful in providing support to our lab when GPC systems were having problems. Vinny, for your help with regards to the pump systems was greatly appreciated, Ambrose – always dependable and patient in providing consumables which keep our labs running, Damien – always provided great lab safety and had a magnificent ability to have a joke with and not take life too seriously, John – helping me for the NMR spectroscopy and IT help, Catherine – always a great help in ordering chemicals and ever so patient when I messed up my order. On the other side, I would express my gratitude to all the DCU library stuff and, I particular, to Barbara Rosinska, whose ability to find papers from a not properly cast reference is just mythic. I cannot find words to express my gratitude to the Prof. Apryll Stallcup, director of the Irish Separation Science Cluster who gave me a huge help and human support. I am in debt with Prof. Brett Paull and Dr. Damian Connolly for the huge scientific support on the analytical aspects of my work. Similarly I wish to thank everyone in Biomedical Diagnostic Institute and Josephine Ozoany for the daily support. I would to express my gratitude to the CRANN, advanced microscopy center and to the Dr. Ed Lavelle who welcomed my ideas on the new possible ELISA tests and who gave me access to his labs. Last but not least, each member of the fantastic Dr. Heise's Polymer Research Group: everyone in this team is at his own way very special and has been contributing to the distinctive human environment of this team: just a mix of hard work, justice and welcoming attitude.

This thesis is dedicated to my wife, Anne, who was able to support and push me every single day of my work even when I was not able to push anymore! Thank you Anne.

List of Publications

Gandhiraman, R. P.; Volcke, C.; Gubala, V.; Doyle, C.; Basabe-Desmonts, L.; Dotzler, C.; Toney, F.; Iacono, M. : Nooney, R. I.; Daniels, S.; Williams, D. E. J. Mater. Chem. 2010, 20, 41167

Volcke, C.; Gandhiraman, R. P.; Basabe-Desmonts, L.; Iacono, M.; Gubala, V.; Cecchet, F.; Cafolla, A. A.; Williams, D.E. Bioelectron. Biosens. 2010, 25 , 1295

Borase, T.; Iacono, M.; Syed, I. A.; Thornton, P. D.; Heise, A. *Polym. Chem.* 2012, 3, 1267

Posters and Presentations

Annual ISSC conference, Dublin City University, Feb. 2010.

Poster title: "Fabrication of nano-structured polymers for potential hilic applications phosphor-peptide enrichment".

Conference on Analytical Science Ireland (CASi), Dublin City University, Feb 2011.

Poster title: "Functional Polymer Grafted Nano-particles for the Modification of HPLC Stationary Phases".

2nd International Symposium on Functional Nano-materials, 6th & 7th September 2012, Dublin City University, Ireland.

Poster title: "Functional Polymer Grafted Nano-particles for the Modification of SPE Stationary Phases".

List of Abbreviations

^{13}C-NMR: Carbon based nuclear magnetic resonance

^{1}H-NMR: Proton based nuclear magnetic resonance

AGET-ATRP: Activators regenerated by electron transfer Atom Transfer Radical Polymerization

AIBN: Azobisisobutyronitrile

ARGET-ATRP: Activators re-generated by electron transfer Atom Transfer Radical Polymerization

ATRA: Transition-metal-catalyzed atom transfer radical addition

ATR-IR: Attenuated total reflectance infra red spectroscopy

ATRP: Atom Transfer Radical Polymerization

BP: Benzophenone

CS-SS: Critical silica super saturation concentration

DEPT-NMR: Distortionless enhancement of polarization transfer nuclear magnetic resonance

DRI: Differential refractive index

DLS: Dynamic light spectroscopy

DMSO-d_6: Deuterated dimethyl sulfoxide

DVLO model: Derjaguin, Verwey, Landau and Overbeek model

EDMA: Ethylene glycol dimethylacrylate

FB-SEM: Bright field secondary electron microscopy

FITC: Fluorescein isothiocyanate

G: Gravitational constant (6.673×10^{-11} N·(m/kg)^2

GMA: Glycidyl methacrylate

GPC: Gel permeation chromatography

HCl: Hydrochloric acid

HF: Hydrofluoric acid

k: Retention factor

L: Ligand

MAA: Methacrylic acid

Mt: Metal centre

N: Theoretical plate

NaOH: Sodium hydroxide

PDI: Polydispersity index

PP: Polypropylene

PPM: Polymeric porous monolith

PTFE: Polytetrafluoroethylene

r: Recovery

RCF: Relative centrifugal force

RT: Room temperature

SCA: Silane coupling agent

SEM: Secondary electron microscopy

SGM: Seeded growth method

SM: Stöber method

t-BMA: *tert*-Butyl methacrylic acid

TEM: Transmission electrons microscopy

TEOS: Tetraethyl ortho-silicate

TGA: Thermo-gravimetric analysis

TPMA: Tris(2-pyridylmethyl)amine

TVB: Total brush volume

UV-Vis light: Ultraviolet-Visible light

V_B: Breakthrough volume

Abstract

Brush polymeric nano-particles are systems of significant interest in a number of transversal fields ranging from fundamental science research up to the development of commercially oriented bench-top-made pilot prototypes. The reason of such attention is easily explained, i.e. the ability to transfer the “smartness” of polymeric chains onto a nano-surface is the open door for combining both the features of the nano-world and of the polymer world. Moreover, often the resulting properties are not just the sum of the component systems (the polymeric brush and the nano-surface). Indeed, the newly formed system can show new and un-precedented features not present in the single separate components.

In this work the formation of brush poly(acrylic acid) nano-particles and their use in a proof of concept system is analyzed. In particular, for the first time, a coherent unified summary of synthesis strategies, tools and approaches to monitor and remediate silica nano-particles based colloidal batches is presented (Chapter 2).
Using these nano-particles, in Chapter 3 the process of formation of the polymeric brush from the surface decoration with a novel silane coupling agent is detailed. The synthesis of this molecule bearing both the silanizable moiety (to be chemically linked on the silica nano-surface) and the radicalic polymerization initiator is originally performed using a click chemistry approach. The advantage of this choice was of double nature: on one hand, a reasonable amount of initiator was available to do a number of surface decoration tests and, in doing so, the definition of a robust protocol had been possible. Detailed analysis of brush thickness increase with the reaction time during the atom transfer radical polymerization completes the chapter.

The last two chapters are devoted to the applicative aspects of the just formed poly (methacrylic acid) silica nano-particles. Specifically, in Chapter 4, an easy and robust protocol to manufacture a cheap solid phase extraction device based on porous poly (EDMA-co-GMA) monoliths is presented. The elements of novelty in this chapter are the carefully monitored process of manufacture. This aspect is of particular interest as the monitoring of such kind of manufacture is not each time easily possible due the geometry of the devices. In the Chapter 5, the problem of the porous poly (EDMA-co-GMA) monoliths surface decoration is defined and discussed. In this context, the brush enhancement factor is defined and treated. The final part of the chapter demonstrates, for the first time, the positive impact on the solid phase extraction performances of the poly (acrylic acid) nano-brushed monolithic surfaces.

Contents

Chapter 1: Introduction

1 Introduction: The features of nano-world and the structure of this work

On December 29th 1959 at the California Institute of Technology Dr. Richard Feynman addressed the American Physician Society with an intriguing talk: "*There is plenty of room at the bottom*".[1] In this seminal talk he analysed the possibility to define and build objects at the nano-scale. Even though it is difficult to assign a definite date for the start of a research field, the year 1959 with its brilliant (and then famous) Dr. Feynman's talk has really inspired this new attention for the nano-scale. Nowadays, nano-technologies are a standalone field of research and it is possible to cite some examples of excellence. In academia and in a number of industries, nano-particles are proposed as drug delivery systems, for example in therapy to deliver treatments such as drugs or to heat directly diseased cells (nano-medicine).[2,3,4] For example, researchers have developed a technique for creating nano-particles that carry two different cancer-killing drugs into the body and deliver those drugs to separate parts of the cancer cell where they will be most effective.[5] Moreover, nano-particles are proposed in diagnostic techniques for rapid testing (potentially in a point-of-care device) and detection of diseases at an earlier stage. [6,7] This early detection offers the possibility of treating a disease earlier, avoiding more damage to the patient. Researchers in Duke University and genome researchers have been using nano-particles for early diagnosis of infectious disease based on the enhancement of the Raman scattering caused by the nano-particles.[8] Nano-particles are also used to develop new methods for fighting bacterial infections. [9,10] The applications of nano-particles in the fields of energy and electronics are far to be less important: Dr. Dunwei Wang at the Boston College, prepared web-like "nano-nets". This nano-material offers a unique structural strength, more surface area and greater conductivity, which produced a charge/re-charge rate five to 10 times greater than typical lithium-ion anode material, a common component in batteries for a range of consumer electronics.[11] Nano-particles also offer solutions to environmental problems as was shown by research at the Toyota Central R&D laboratories, which focused on the use of gold nano-particles in manganese oxide to reduce volatile toxic organic compounds in the air.[12] These are just a few of many examples where nano-

particles have contributed to the development of advanced materials but what makes nano-particles so special?

A particle with dimensions ranging from a few nm to a few µm is defined as a nano-particle. It can be typically made up of 10^3 to 10^9 atoms. A dispersion of nano-particles in a liquid is defined as a colloid. The nature of the forces between dispersed nano-particles rules the time stability of the colloids; if not stable, nano-particles can sediment, crystallize or flocculate forming macroscopic aggregates. The dimensional scale considered here is at the border line between the atomic world (ruled by quantum-mechanical laws) and the micro/macroscopic world (ruled by gravitational, frictional and inertial forces of classic mechanics). For example, if a cube of 1 m^3 is divided into n^3 sub-cubes of the same volume, the surface generated will increase from 6 x 1 m^2 to 6 x n^3 m^2. The total surface of the system will thus increase with a cubic power trend with n increasing. The forces predominantly acting on the cubes will change accordingly with the growth of the number n. Indeed, the single 1 m^3 cube in solution would be mainly governed by the gravitational/inertial forces but, with increasing n, the forces deriving from the interaction between the surfaces and the medium of suspension will gradually predominate over the gravitational/inertial forces. The first important property of a nano-particle-based system is its large surface compared to its mass: 1 g of silica nano-particles with a diameter of 100 nm has a surface area of more than 22 m^2. This has direct implications on the application fields for example in chemical catalysis or medical devices for drug delivery.[13] One of the challenges in the science of colloids is the precise control of the surface chemistry in a way to prevent any aggregation. Notably, at the nano-scale the frictional forces will also play an important role. In some cases, this is an advantage (e.g. for more or less permanently physically absorbed nano-articles on a surface) or it can be a problem (e.g. the non-specific binding of sensing nano-particles in cell or antigen recognition processes). What is the nature of these forces and how to subdivide a mass into fine enough nano-particles so as to assure the existence of a stable colloid? These two questions are intimately linked.

In the 1940s four scientists (Derjaguin, Verwey, Landau and Overbeek) developed a model (the DVLO model from the authors' initials) to justify the stability of nano-

particles in suspension as the balance of two opposing electrostatic forces: In the colloid, the van der Waals' forces tend to attract particles, while the presence of an electric double layer surrounding the particles at the particles-medium of suspension interface, tends to repel the two systems.[14] The van der Waals' forces are formed by dipole-dipole attractive interactions between two atoms, particles or surfaces and, on the other hand, the presence of an inter nano-particles repulsive force can be explained by the presence of a ionic double layer at the nano-particles/medium of suspension interface. Indeed, once the nano-particle is formed, a number of possible events can be envisaged deriving from interactions at the interface of the dispersion liquid/nano-particles surface (e.g. reactions with H^+ or OH^- ions, adsorption of lattice ions, and dissociations of surface groups) and, as a consequence, the outer nano-particle layer can be positively or negatively charged. In this case, ions with opposite charge with respect to the nano-particles surface can leave the bulk of the suspension liquid and locally concentrate on the nano-surface to minimize this electrostatic energy forming an electric double layer. Hermann von Helmholtz, in 1853, was the first to realize that two ionic layers of opposite polarity form at the interface between solvents and systems immersed in liquids (specifically, electrodes).[15] This model was then refined by Louis Georges Gouy in 1910 and David Leonard Chapman in 1913 with the definition of a diffuse model for the double layer where the counter-ions concentration is a function of the distance from the considered surface.[16,17] Finally, in 1924, Otto Stern revised this model in the case of highly charged double layers.[18] The presence of an electric double layer is responsible for the origin of inter-particle repulsive forces. Indeed, the eventual accumulation of ions deriving by the overlap of the two approaching nano-particles double layers would create a local increase in the osmotic pressure. As a consequence, some solvent from the bulk would come to dissolve (or, locally re-dilute) this ions accumulation preventing the surfaces approaching each other. The research line about experimental measurement of this double electric layer between surfaces and medium of suspensions is still in its early stage. For example, liquid ordering near flat solid surfaces to the depth of 1-3 nm has been well documented experimentally and theoretically, but whether similar liquid ordering would occur on a highly curved surface has only been speculated.[19] There is

almost no experimental data directly or indirectly showing the structuring of the liquid molecules on highly curved surfaces of nano-particles.

The measurements of colloidal forces for nano-particles of silica and alumina using atomic force microscopy (AFM) suggest that 10 nm silica particles are surrounded by about a ca. 1 nm hydration layer in electrolyte solutions but this finding needs to be confirmed by other laboratories and for other nano-particles.[20] It is possible that the size dependence of interfacial energy in nano-particles contributes to structuring of liquids immediately adjacent to nano-surfaces.

To maintain the stability of a colloidal system, the repulsive forces must be dominant and this can be achieved either by steric repulsion (by the use of polymers absorbed or grafted on the nano-particles surface) or by electrostatic stabilization (using permanent charges present on the surface of the system). This discussion delineates just the essential ideas of the DVLO model. The discussion of this model is far from general. After 50 years or more of studies dedicated to the real experimental measurement of these interactions there is not yet a definitive and general model.

Moreover, an increasing number of extra-DVLO-forces have been presumed or argued. Critical discussions on these extra-DLVO models proliferations have been recently made concluding that: *"... Where the theory apparently fails, new words to describe 'non-DLVO' forces have been invented. Extra-DLVO forces and words like hydration, structural, oscillatory, hydrophobic, depletion, fluctuation, protrusion forces infest the literature. Some are real enough but some have the status of phlogiston. All predictability has disappeared in a confused proliferation of parameters …* ".[21]

1.1 Stöber method: a simple approach to the synthesis of amorphous silica nano-particles

Colloidal systems of amorphous silica nano-particles can be synthesized by Stöber method (SM)[22], seeded growth method[23], water in oil micro-emulsions[24-26] or lysine-catalyzed synthesis.[27,28] These four techniques are actually based on the same chemical reactions: the hydrolysis and condensation of alkoxy derivatives of ortho-silicates and encompass a period of time from 1968 to nowadays. The SM is described by the three reactions in Figure 1.1. These three equilibria reactions describe the method at the level of the functional groups involved. It is evident from reactions (1) - (3) (see Figure 1.1) that the chemical species in the alcosol (or silica gels under certain conditions) evolves sequentially as the product of successive hydrolysis and condensation reactions (and the reverse reactions, esterification and alcoholic or hydrolytic de-polymerization). The intriguing feature of this simple sequence of reactions is that they explain a large number of experimental facts and, importantly, the experimental and structural variations obtained under different conditions.

The hydrolysis in (eq. 1.1) is a nucleophilic SN_2 attack of the oxygen contained in water on the silicon atom as proven in some studies based on the isotopic effect. [29] McNeil[30],Pohl and Osterholtz[31] have studied the hydrolysis of trialkoxysilanes in buffered aqueous solution and this reaction appears to be both acid and base catalysed. There is also a clear influence of steric effects on this reaction. Any steric hindrance of the alkoxy group retards the hydrolysis of alkoxysilane and consequently the hydrolysis rate is lowest for branched alkoxy groups.[32] Extremely interesting is a study of H. Schmidt focused on the inductive effects on this hydrolysis reaction. [33] Under acidic conditions (typically by using HCl) the hydrolysis rate increases with the degree of alkyl substitution, whereas under basic conditions (typically by using NH_3) the reverse trend is clearly observed. The consistent acceleration and retardation of hydrolysis under acidic or basic conditions, respectively, suggests that the hydrolysis mechanism is subject to inductive effects. As increased stability of the transition state will increase the reaction rate, the inductive effects are evidence for positively and negatively charged transition states or intermediates under acidic and basic conditions, respectively.

Under acidic conditions the hydrolysis rate decreases with each subsequent hydrolysis step, whereas under basic conditions the increased electron withdrawing

capabilities of Si-OH compared to Si-OR may establish a condition in which each subsequent hydrolysis step occurs more quickly as hydrolysis and condensation proceed. Last but not the least, the role of the solvents must be considered. The hydrolysis is both hydroxyl and hydronium ion catalysed, therefore solvents capable of forming hydrogen bonds with hydroxyl ions or hydronium ions rule the catalytic activity under basic and acidic conditions, respectively. Therefore aprotic solvents tend to render hydroxyl ions more nucleophilic, whereas protic solvents make hydronium ions more electrophylic. It is important to note that the esterification process in (Eq. 1.1) is a faster process under acidic conditions than under basic conditions.[34]

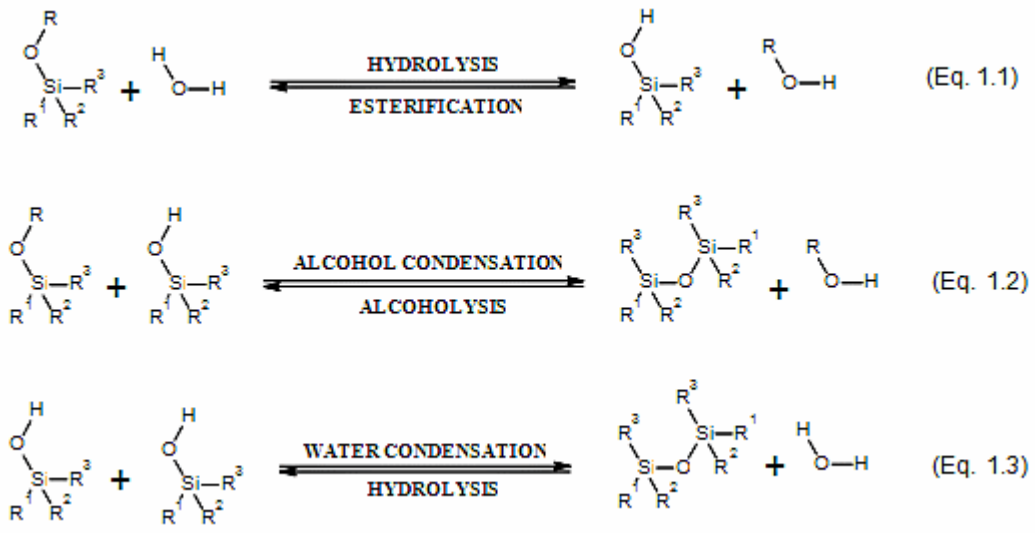

Figure 1.1: The three equilibria reactions describing the chemistry of the Stöber method. R^1, R^2 and R^3 are alkoxy groups.

The reaction mechanisms (Eq. 1.2) and (Eq. 1.3) are the core of this reaction system as both equilibria explain the formation of monomers, dimers, linear trimers, cyclic trimers, cyclic tetramers and higher order rings or oligo-networks. The experimental work on the clarification of these condensation mechanisms is still under questions. The most widely accepted mechanism for the condensation reaction involves the attack of a nucleophilic de-protonated silanols on a neutral silicate species to explain condensation in aqueous systems but other mechanisms have been postulated as

well. [35,36] Alcoholysis and hydrolysis of siloxane bonds (reverse of eq. 1.2 and 1.3), provide a means for bond breakage and reformation, allowing continuous restructuring of the growing polymers before final stable sols are formed. The hydrolysis reaction (dissolution of silica) exhibits strong pH dependence.

The interesting fact is that the silane derived rings form the elemental framework for the generation of discrete colloidal particles, which are commonly observed in aqueous systems.[37] This sequence of condensation requires both de-polymerization (ring opening) and the availability of monomers (species which may be produced by de-polymerization). However, in alcoholic solutions (especially at low pH), the de-polymerization rate (reverse of (Eq. 1.1-3), is very low. Iler speculated that, under conditions where de-polymerization is slow (so that the condensation is irreversible and siloxane bonds cannot be hydrolyzed once they are formed), the condensation process may resemble classical polycondensation of polyfunctional organic monomer resulting in a three dimensional molecular network.[37] Owing to the insolubility of silica under these conditions, the condensation polymer from siloxane chains cannot undergo rearrangement into particles. The frequency of the reverse reactions depends on processing conditions, and condensation may result in a spectrum of structures ranging from molecular networks to colloidal particles.

In contrast to the reaction (Eq. 1.1) the condensations reactions can proceed under thermal as well as under specific acid-base catalysis. An easy way to measure the overall condensation kinetics is to determine the time needed by the system to become a gel (gel time). In the specific case of the systems under discussion the gel time is minimized at pH 2.5 and non-gelling suspensions are obtained under more basic conditions. The easy interpretation of this fact is based on the consideration that at pH 2.5 there is the iso-electric point of the silica and at lower pH silanols groups are protonated while at higher pH silanol groups are de-protonated. At elevated pH where the gel times are increased, condensation reactions proceed but gelation does not occur. In this pH regime particles are formed which, after reaching a critical size, become stable due to mutual repulsion effects. This high pH region represents the conditions in which Stöber silica particles are formed. Figure 1.2 shows

a general graph correlating the pH with the gel time. There are mainly three zones. A metastable zone (pH range 0 - 4), where the gel time is increasing due the fact that the charge density on the particles is very low. This results in particle-particle collisions to be frequent and effective to form irreversible siloxane bonds from the silanols present on the surface. In the rapid aggregation zone (pH range 4 – 6) this trend is stronger. In the pH range 6 – 10 the charge on the particles surface is able to prevent collisions and aggregation. The graph also shows how NaCl would be able to destabilize a stable sol.

The species in equilibrium and their concentrations, the position of the equilibria and the final structural morphology (if any) of the nano-object formed are essentially ruled by two simple parameters: $[H_2O]/[Si]$ =R and pH. Indeed, with these two parameters it is possible to define two distinct extreme conditions. Condition A: acid-catalyzed hydrolysis with low R ratios produces weakly branched "polymeric" networks. Conditions B: base-catalyzed hydrolysis with large R produces highly branched "colloidal" particles. Intermediate conditions produce structures intermediate to these extremes. Since these structural variations can only result from a different sequence of the basic reactions (see Equations 2.1-3), the fundamental questions surrounding hydrolysis and condensation in silicates concern the factors determining the sequence of these reactions. This so distinctive trend of the alcosols/gels based on silicates is shown in Figure 1.2.[38]

It is clear that the initial random distribution of monomers, dimers and oligomers become organized into networks, clusters, or particles depending on the specific growth conditions. The silica polymerization in aqueous media is mainly described by a nucleation and growth model.[39] There are a number of theoretical models describing this just depicted sequence of events. The LaMer and Dinegar model (see Figure 1.3) for the first time introduced the idea of critical super-saturation concentration as the core mechanism as the basis of silica nano-particles formation.[40] At a critical degree of super-saturation, nuclei form and subsequently grow by the addition of monomer. The monomer is initially supplied by the supersaturated solution. As the degree of super-saturation diminishes, oligomers (which have been in solubility equilibrium with the higher monomer concentration) de-polymerize and

add to the growing nuclei. This idea, ruling the SM, is as well present in the SGM as it will be shown below. In the 1992 two other possible models appeared: the Bogush and Zukoski[41] model and the Bailey[42] model.

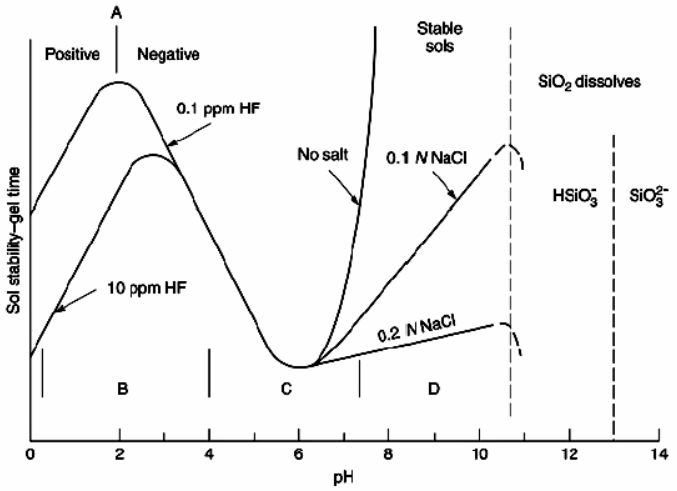

Figure 1.2: Effects of pH in the colloidal silica–water system, where A represents the point of zero charge; regions B, C, and D correspond to meta-stable gels, rapid aggregation, and particle growth, respectively. Positive and negative correspond to the charges on the surface of the silica particle. [43]

All models have some peculiar assets and limitations as well as points of overlap but in all different models there is an obvious general scheme involving the concept of super-saturated solutions and monomer addition on the particles surface. Computer simulations by Keefer[44] have confirmed the two aforementioned scenarios:

a) When the hydrolysis reactions are faster than the condensation reactions in acidic pH, the formation of polymer-like networks or sometimes, porous particle with small pores is preferred. This is the clear consequence of the presence of an intermediate barrier (due the interaction potential) preventing aggregations (this is termed as reaction-limited aggregation).

b) When the hydrolysis reactions are slower than the condensation reactions in alkaline pH, the formation of large, non-porous particles or, sometimes, colloidal gel with large pores is preferred. In this case there is no barrier and the interaction potential between the particles is purely attractive, meaning

the aggregation process is solely limited by mutual diffusion (or Brownian motion) of the particles (this is termed diffusion limited aggregation).

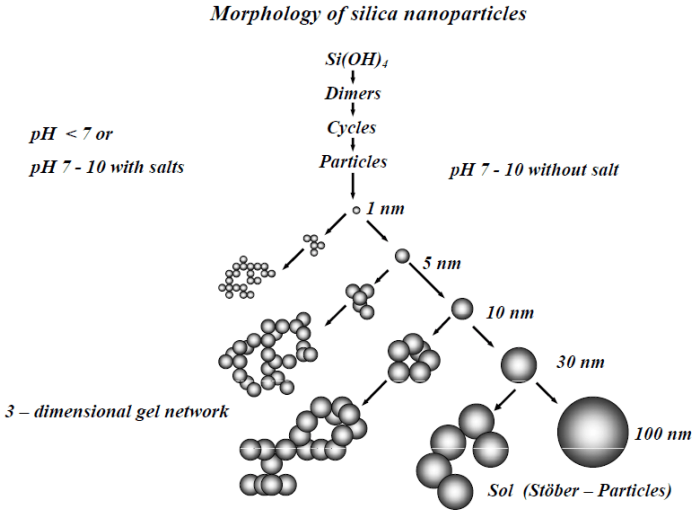

Figure 1.3: Relationship between pH and morphology of the Si-NPs.[13]

The qualitative aspects of the models are now clarified. A reaction of hydrolysis forms a super-saturated solution of silicic acid and a number of condensation steps promote the formation of initially fluffy aggregates and then of smoothed nano-particles (this is the so-called Ostwald ripening[45]) up to the point where all the oligomers are consumed and the charge on the particles prevent any further increment of the diameter.

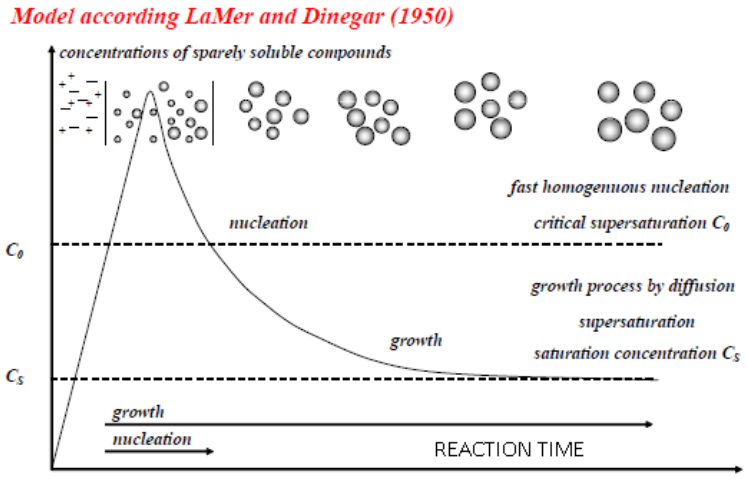

Figure 1.4: The LaMer and Dinegar model.[15]

1.2 The silica surface and the Zhuravlev model

The Zhuravlev model predicts the properties and the chemical species on the silica surfaces. Indeed, even if the bulk amorphous silica is – in principle - characterized by a quite strong chemical and physical stability, amorphous silica surfaces present unexpected variety of chemical Si groups depending on synthesis conditions, surface shape and eventual thermal treatments. The Zhuravlev model is crucial to understand how to "standardize" a silica surface before any chemical treatment before the grafting of initiators onto silica nano-particles as carried out in Chapter 3.

Amorphous silica (a non-crystalline form of silica) presents a bulk structure determined by random packing of $[SiO_4]^{4-}$ units. The bulk material and the surface of the same material present different inter-atomic and inter-molecular distances and arrangements. Silica nano-particles surface exhibits hydrophilic behavior but – after a proper calcinations process – this surface become hydrophobic.

A number of scientists in the 1930s defined a model for the condensation of silicic acid (one of the reactions involved in the synthesis of silica).[46,47] In particular, Kiselev was the first author able to clarify that the water evolving from the silica surface during measurements of the heat of wetting, beside the normally physically absorbed water, originates from OH groups that are chemically located on the silica surface. This was the first time that it was postulated that on silica surfaces not $[SiO_4]^{4-}$ or SiO_2 is present but silanols Si-OH. Only with the advent of infrared spectroscopy in the year 1948, Yaroslavsky[48] and Terenin[49] had the first analytical evidence of the existence of hydroxyl groups on the silica surface.

Nowadays, there are numerous methods unambiguously confirming the presence of silanol groups on the silica surface formed either during the condensation and polymerization of silicic acid to form nano-particles or by re-hydroxylation of de-hydroxylated silica. Of course, the driving force for this process is the formation of a complete tetrahedral configuration of the silicon atoms at the surface. With that

knowledge it was possible to explain the surface properties of amorphous silica as being determined by the presence of silanol groups. At a sufficient concentration these groups make such a surface hydrophilic. The OH groups act as the center of molecular adsorption during their specific interaction with solvents capable of forming donor–acceptor bonds. The removal of the hydroxyl groups from the surface of silica leads to a decrease in the adsorption, and the surface acquires more and more hydrophobic properties.[50]

The numerous experimental data on the behavior of the silica surfaces have been collected, confirmed and organized over 25 years by L. T. Zhuravlev.[51] The properties of a pure silica surface are defined by the concentration and the distribution of different types of OH groups, and on the presence of siloxane bridges and the macro/meso and micro porous structure of the silica.

The “Zhuravlev model” describes the energetic heterogeneity of the silica surface as a function of the pretreatment temperature of SiO_2 samples.

In the bulk and on a silica surface, it is possible to define the presence of

- physically sorbed water,
- isolated free Si-OH or geminal free $Si(OH)_2$,
- vicinal, or bridged, OH groups bound through the hydrogen bond,
- siloxane groups Si-O-Si bridges with oxygen atoms on the surface,
- structurally bonded water inside the silica skeleton and internal silanol groups.

The “core” physical phenomenon at the heart of the Zhuravlev model is the characteristic “memory effect” of the silica surface and its variations in hydroxyl coverage with respect to the temperature of preliminary thermal treatment in vacuum. Zhuravlev was able to define analytical techniques to discriminate between these different types of –OH groups, for example deuterium exchange, mass spectrometric thermal analysis in conjunction with the temperature-programmed desorption (the MTA-TPD method), infrared spectroscopy, and some others.

The concentration of -OH groups per nm^2 or the "silanol number" is the physical parameter normally used to describe a silica surface (see Equation 1.4).

$$\alpha_{OH} = \frac{\delta_{OH}^{S} \bullet N_A \bullet 10^{-21}}{S} \qquad (\text{eq.}1.4)$$

Equation 1.4: The silanol number. The specific surface area of the silica sample is determined by the Brunauer–Emmett–Teller (BET) method[52] by using low temperature adsorption of krypton (the area occupied by one Kr atom in a monolayer is 0.215 nm^2).[53] α_{OH} is the number of OH groups/mm^2, $\delta^S{}_{OH}$ are the mmol of OH groups/g of SiO_2, N_A is the Avogadro number in unit/mol, S is the specific surface area in m^2/g.

The silanol number when the surface is hydroxylated to the maximum degree is considered to be a physico-chemical constant (Kiselev-Zhuravlev constant) at 4.9 OH/nm^2. Figure 1.5 depicts the detailed Zhuravlev model stages A-E, which can be distinguished. In essence, it must be understood that a silica surface has a memory of its thermal history!

Initial stage: The SiO_2 surface is in a maximum state of hydroxylation and all the different types of silanol groups (see Figure 1.5: isolated singles in black, geminals in blue, vicinals in red) are present. The surface is covered by multiple layers physically adsorbed water (the surface OH groups and adsorbed water are permeated with an H-bond network). The internal OH groups are present inside the SiO_2 skeleton.

Stage A: Complete removal of multiple layers of physically adsorbed water (this process is reversible upon the introduction of an excess of water). A single layer of water is physically adsorbed.

Stage B: The surface is in a maximum state of hydroxylation and all the different types of silanol groups are present. The surface is covered with a single (or less) layer of adsorbed water and tends to dry completely towards the end of this stage. The surface silanol groups are predominantly bound via H-bonds. The internal OH groups are present inside theSiO_2 skeleton. This stage is reversible.

Stage C: The overall degree of surface hydroxylation decreases significantly. Even if all the different types of silanol groups are present, the concentration of isolated single OH groups increases reaching a maximum at 400°C. To be noted, the concentration of vicinal bridged OH groups decreases at about 400°C as do all internal OH groups.

Stage D: The concentration of isolated single and germinal OH groups decreases and at temperatures close to about 800–900°C the silica surface becomes free of geminal OH groups. The internal OH groups disappear completely from the silica skeleton and the concentration of siloxane bridges increases considerably and whole areas on the silica surface become covered by Si-O-Si. The removal of surface germinal silanols and internal OH groups is complete. Even if isolated single silanols still remain on the surface, at room temperature the process is hardly reversible upon the introduction of an excess of water and it takes a considerable time for the reverse process to be completed. However, at 100°C this process becomes reversible and it proceeds quite rapidly.

Stage E: Complete removal of all OH groups from the silica surface and complete coverage of the SiO_2 surface with Si-O-Si groups.

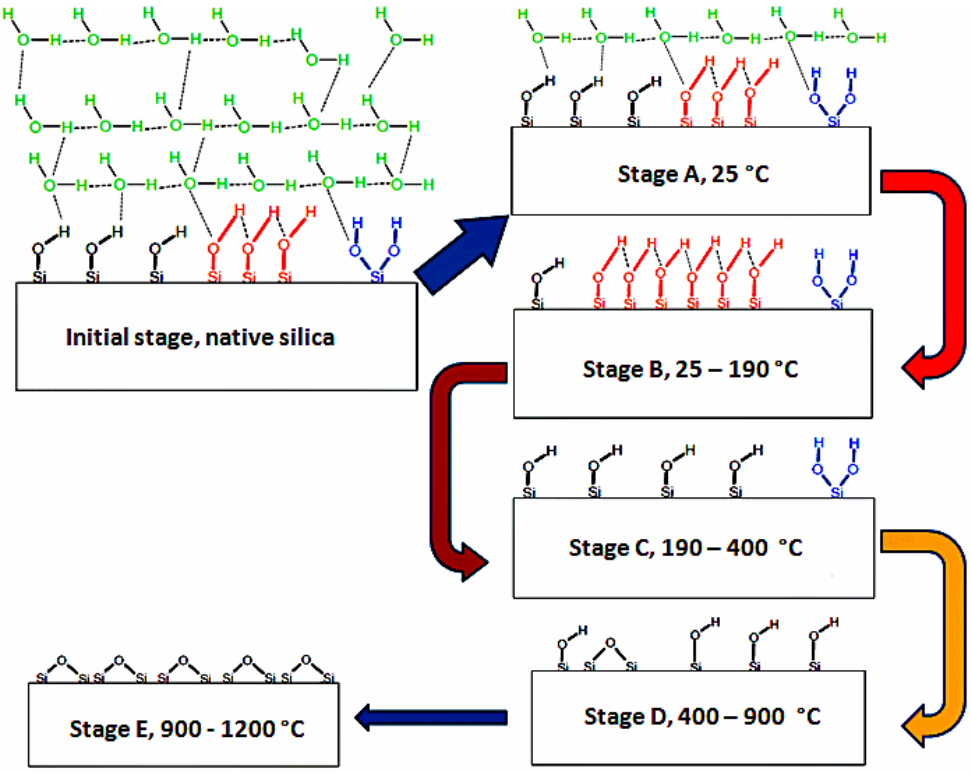

Figure 1.5: The change of silica surface silanol groups as a function of the thermal treatment according to the Zhuravlev model.

1.3 Atom transfer radical polymerization (ATRP)

Mitsuo Sawamoto[54] and Krzysztof Matyjaszewski[55] independently published two seminal papers in 1995 and 1996, respectively, casting the bases for Atom Transfer Radical Polymerization (ATRP). This new technique has had an exceptional influence on the development of polymerization chemistry since 1996: At that time, only polymerization mechanisms involving addition (anionic and cationic) and ring-opening reactions were well defined in terms of molecular weight and polydispersity.[56, 57] The use of a living polymerization based on radicals was the "next frontier in the world of polymer synthesis": An initial group of researchers developed a number of not yet generally valid living radical polymerization examples from 1982 to 1994 indeed.[58-66] The pivotal point in this research line was, in the well-known framework of the free radical polymerization, to control termination reactions and to reach fast rates of initiation with respect to the rate of radical propagation and polymer chain growth. A polymerization system with virtually absent termination reactions, even once all the starting monomer is consumed, would indefinitely continue to produce

chain growing reactions if new aliquots of monomer are added. From this feature, the term “living” was firstly used by Michael Szwarc in 1956.[67] On the other hand, to have fast rate of initiation with respect to the rate of chain propagation would have a beneficial impact on the uniformity of the polymer chain length as all the active sites of radical propagation are formed before any chain growth. In this way, there are not new initiation sites forming during the chain growth and all the polymer chains have the same expected length at the end of the reaction. The primary reasons for the difficulty to control radical polymerizations include the high reactivity or low stability of free radicals and their facile cross-coupling and/or disproportionation reactions.

ATRP is a process about stabilization of radicals as dormant species and the use of redox complexes to inhibit the typical and undesired radical side reactions. This new process can be conceived as a virtually infinite and periodic repetition of the first instants (or ms) of a free radical process (when the termination reactions are not yet predominant) ruled by a statistically persistent (and low in concentration) number of active radicals in equilibrium with their dormant counterpart. The driving force for the development of this new technique was the need for the synthesis of uniform macromolecules with controlled size, topology, composition and functionality where all chains are instantaneously initiated and grow concurrently without significant occurrence of chain breaking reactions, such as termination and transfer.

The ATRP process is first of all a catalytic reaction based on a transition metal species (Mt) able to expand its coordination sphere and increase its oxidation number. Cu(I) or Cu (II) are the most frequently used transition metals, but other metals including Ru, Fe, Mo, Os can also be employed.[68] The second important component in this process is the ligand (L). The ligand has a direct influence on the activity of the metal center, indeed, in the case of Cu (I)/L complexes exhibits variations of the activation rate constant (see k_{act} , Figure 1.6) over 7 orders of magnitude. In particular it has been clarified that in the case of N-based ligands the activities of the Cu(I)/ligands complexes are highest for tetra-dentate ligands, lower for tridentate ligands, and lowest for bi-dentate ligands.[69] The control in ATRP depends first of all on the appropriate equilibrium between the activation process (generation of radicals, see

k_{act}, Figure 1.6) and the deactivation process (see k_{deact}, Figure 1.8): Indeed, $K_{ATRP}=k_{act}/k_{deact}$ rules the concentrations of radicals and so, the rate of polymerization, polydispersity and the undesired side reactions (terminations and disproportionation). The complex Mt^Z/L, at the start of the reaction, reacts with the so-called initiator, a chemical species able to promote the formation of radicals. The initiator's chemical structure (typically an alkyl halide) and its concentration relative to the monomer are two of the main parameters to be considered. For example, the equilibrium constants are largest for tertiary alkyl halides and smallest for primary alkyl halides. The activities of alkyl bromides are several times larger than those of the analogous alkyl chlorides. The number of growing polymer chains is proportional to the initiator concentration. The faster the initiation is, the fewer termination and transfer steps will be resulting in narrow molecular weight distributions of the polymeric products.[70] The shape or structure of the initiator can determine the architecture of the final product. For example, initiators with multiple alkyl halide groups on a single core can lead to a star-like polymer shape.[71]

The transition metal complex (Mt^Z/L) is responsible for the homolytic cleavage of an alkyl halogen bond $R_{initiator}$-X which generates the corresponding higher oxidation state metal halide complex X-Mt^{Z+1}/L (with a rate constant k_{act}) and an organic radical $R_{initiator}$*. This formed radical can propagate with monomer (k_p), terminate as in conventional free radical polymerization by either coupling or disproportionation (k_t, k_d), or be reversibly deactivated (k_{deact}) in this equilibrium by X-Mt^{Z+1} /L to form a halide-capped dormant polymer chain. Radical termination is diminished in ATRP as a result of the persistent radical effect[72,73], and, for this reason, the ATRP equilibrium ($K_{ATRP} = k_{act}/k_{deact}$) becomes strongly shifted towards the dormant species (see Figure 1.5). Notably in ATRP many monomers can be used such as styrenes, acrylates and methacrylates, acrylamides, and acrylonitrile, monomers with hydroxy and amino groups only to cite some of them.

Some groups interfering with the catalyst system (such as carboxylic acids) can be blocked and unprotected after the polymerization process. Another factor defining the enormous potential of this technique is also the variety of reaction media

compatible with this kind of reaction. ATRP can be performed in bulk, in many polar and non-polar organic solvents, in CO_2, or in water. Water-soluble monomers (both neutral and ionic) can be polymerized by ATRP in protic (aqueous) media, provided that a proper catalyst selection is made. The range of temperature spans from sub-ambient to over 130°C.[74] Typically, no pressure is required, but, in some cases, increasing the pressure significantly enhances the rate of polymerization, while retaining control over the polymerization.[75]

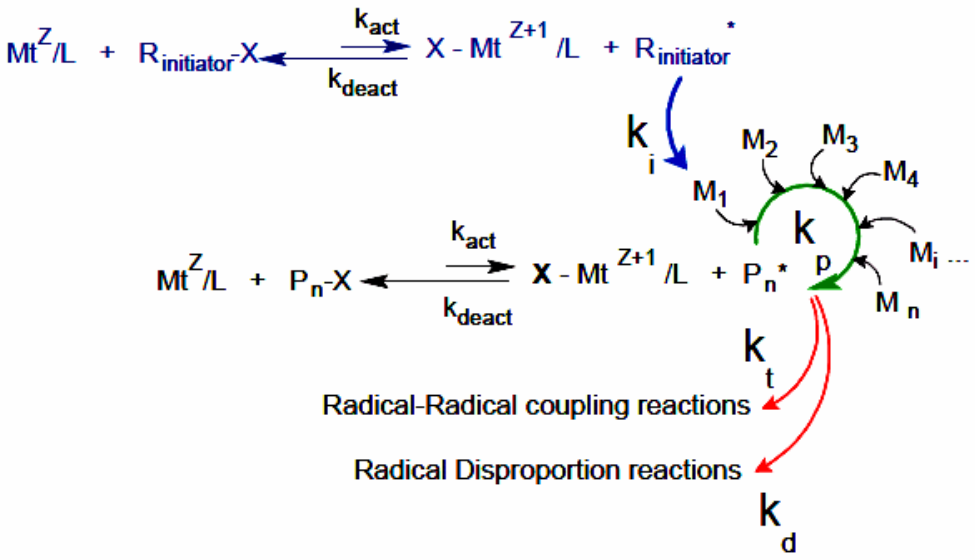

Figure 1.6: ATRP general scheme and expression of the rate of polymerization. In the upper blue reaction, the t=0 (blue arrow, the primary generated radicalic species), green arrow: the polymeric chain growth, red arrow: termination processes. The ATRP scheme can be seen as the confluence point of the free radical polymerizations and the ATRA mechanisms (see Figure 1.7). In the scheme "/L" symbolize the ligand(s) on the metal centre. The rate constants are in $M^{-1}s^{-1}$.

A well developed ATRP system is typically able, under normal conditions, to control termination reactions down to the 1 to 10 % of the whole polymer population.[76] The selectivity of this system involving radical reactions has been explained in terms of the persistent radical effect by Fisher.[77] The degree of control in ATRP is strongly affected by the position of the equilibrium (K_{ATRP}) and by all the other rate constants. K_{ATRP} depends on the solvent, temperature, monomer (i.e., structures of RX and R^*), and structure of the metallic catalyst species. According to reactions scheme in Figure

1.5, neglecting termination reactions due to persistent radical effect and using a fast equilibrium approximation, the rate law for ATRP can be derived as follows:

$$R_p = -\frac{d[M]}{dt} = k_p \bullet [M] \bullet [P_n^*] = k_p \bullet [M] \bullet K_{ATRP} \bullet \frac{[R_{initiator} - X] \bullet [Mt^Z/L]}{[X\,Mt^{Z+1}/L]} \quad \text{(Eq. 1.5).}$$

In the Equation 1.5 the rate of polymerization is approximated in terms of k_p, (monomer propagating rate coefficient), [M] (monomer concentration), $K_{ATRP}=k_{act}/k_{deact}$ (ratio of the rate constant of activation and deactivation), concentration of halide initiator, and the ratio of the activator and deactivator systems.

Molecular weight distribution, on the other hand, or polydispersity index (PDI = M_w/M_n) in ATRP depends on the propagation rate constant (k_p), deactivation rate constant (k_{deact}), monomer conversion (p), and concentrations of dormant species, monomer and deactivator (X–Cu(II) according to Equation 1.6:

$$\frac{M_w}{M_n} = 1 + \left(\frac{[P_n - X] \bullet k_p}{k_{deact} \bullet [X\,Mt^{Z+1}/L]} \right) \bullet \left(\frac{2}{p} - 1 \right) \quad \text{(Eq. 1.6).}$$

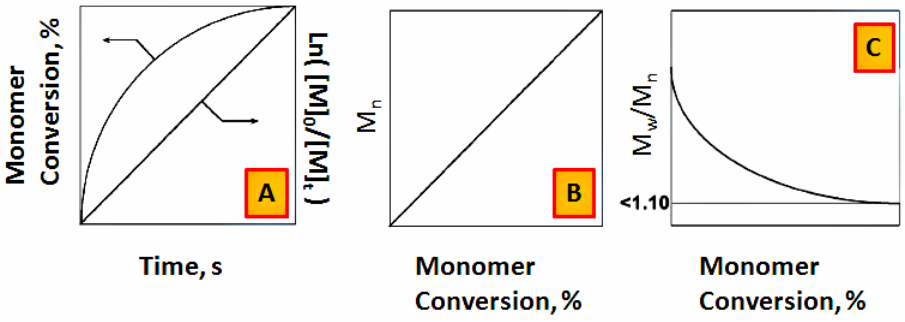

Figure 1.7: Insert A: typical linear variation of conversion with time in semi-logarithmic coordinates observed in metal-mediated ATRP (typically copper). Inset B: polymer molecular weight vs. conversion and Inset C: molecular weight distribution (Mw/Mn) or polydispersity index (PDI).

The ATRP technique represents a significant step forward in the livingness and control of polymeric reactions. Nevertheless, the catalyst can be harmful or add undesired color to the polymer. For these reasons time/money consuming methodologies are typically part of the work up protocols of the ATRPs. These can include removal of

the catalyst using ion exchange resins, extractions with water or polymer precipitation, use of biphasic systems, solid supported catalysts.[78] Lowering the metal catalyst concentrations was therefore a main research aim for the next generation ATRP. The strategy to achieve this has been proposed by Matyjaszewski: copper (II) that accumulates as a persistent radical during ATRP can be continuously reduced to the corresponding copper (I) complex if a reducing agent unable to initiate new polymer chains is present. This is the so-called activator regenerated by electron transfer ARGET-ATRP.[79] This modification of the ATRP technique has a number of advantages:

a) The ARGET ATRP system can be prepared handling air stable catalyst (notably Cu(II) halides): the use of the air sensitive CuBr is no more necessary.
b) The amount of catalyst can be reduced to ppm as the C(II) is regenerated by the reducing system.
c) The need of demanding metal purification steps is greatly reduced or eliminated.
d) ATRP can be performed in flasks and well sealed vials with no specific oxygen depletion steps: Indeed, the reducing agent, added in a large excess, typically [reducing agent]/[Metal]=1:10) (and tolerated by the ATRP) can work as oxygen scavenger.

ARGET-ATRP relies on the use of a very active copper catalyst used in minute amounts in the presence of excess reducing agent that reacts slowly. Under these conditions, activators are continuously regenerated and even parts per million amounts of catalysts can lead to a successful ATRP.[80-87] A large excess of reducing agent is not affecting the process and reactions can be carried out without any de-oxygenation, in flasks fitted with rubber septa or even in simple jars. Another benefit of that is the significantly reduced amount of catalyst used (see Figure 1.7), a solution that opens possibilities in applications sensible to the presence of metals as in biomedicine.[82]

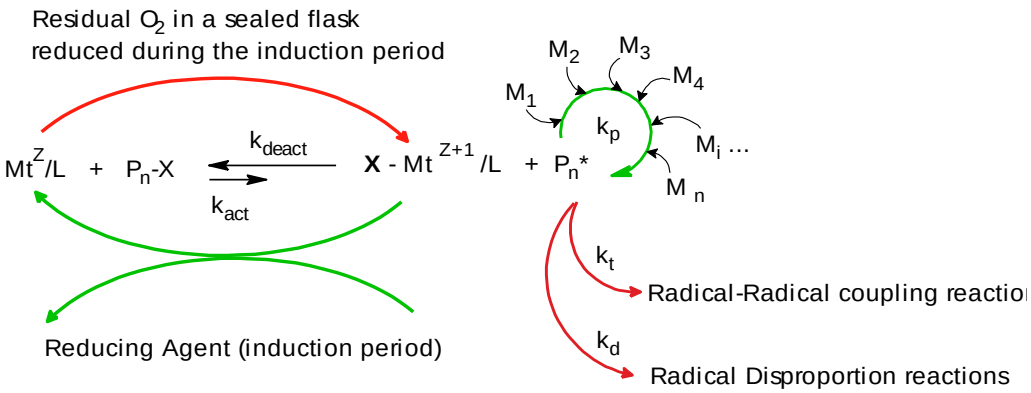

Figure 1.8: The ARGET-ATRP scheme (initiation step omitted for clarity). On the left, red arrow: the residual oxygen being consumed; green arrow: the reducing agent oxygen-antagonist pathway.

1.4 Solid phase extraction with porous polymeric monoliths

Solid phase extraction (SPE) is an excellent technique for the selective extraction, concentration and purification of analytes from complex matrixes.[83-85] This technique is routinely used in environmental chemistry[86-88], in food/agriculture industries[89-92] and in the pharmaceutical or bio-technological sectors. [93, 94] The extraction process is ruled by physico-chemical interactions between the analytes and the solid phase. SPE overcomes many of the problems associated with liquid/liquid extraction such as incomplete phase separations, less-than-quantitative recoveries, use of expensive glassware and large quantities of organic solvents. Extractions are carried out using cartridges housing a solid phase (SP) (see commercial example in Figure 1.9 Inset A). The technique is, in general, a four-step process (see Figure 1.9, Inset B, steps a, b, c and d). The SP, equilibrated with a solvent, is eluted with the loading solution containing the analyte (impurities are eventually retained as well). The analyte, after a washing step, is collected during a final elution. Nowadays, SPE-related technologies occupy an important part of the commercial sector inherent to the purifications media. In the last 25 years, automated (and expensive) systems, non-automated systems, and related aftermarket SPE products affirmed in the pharmaceutical industry (with a 2012 market share of nearly one third of the all SPE market).[95]

Monolithic porous polymeric SPs are a new appealing alternative to the less performing particle-packed cartridges.[96-103] Noeland was the first to use the term "monolith" (originating from the Greek μονο-λιτησ combining the two words "μονο", i.e. single, continuous piece of a material, and "λιτησ", i.e. stone) in 1993.[104] Indeed, a monolith is a single piece of porous material that is formed of interconnecting flow-through channels from one end of the system to the other. Svec described polymer monoliths as poorly organized micro-globule structured materials with only large pores present.[105] This kind of extraction system rapidly became a standard.[106] One of the factors driving the success of monolithic materials is the possibility to mold inside a housing (typically made in polypropylene (PP) or soda-lime glass), produce polymeric monoliths with a tailored morphology to form disks, membranes or cylinders[107] and at the same time imposing nano-porous structures with a predictable size.[108]

In particle-packed columns, mass transfer processes during the purification/extraction are ruled by diffusion while in monolithic materials the mass transfer is ruled by faster convection phenomena. A monolith eliminates two problems of the particle-packed columns, i.e. the slow diffusion of solutes into pores/interstices (wherein stagnant mobile phase is present) and the large interstitial volume between particles.[109] In monoliths, the eluent is forced to flow through pores and not through the particles interstices and this further enhances the mass transfer rate. [110] A constant interaction between the eluent and the stationary phase is assured and an increased mass transfer results, even when high flow rates are used.

In Figure 1.10 the differences between particle-packed and monolithic solid phases are detailed. The particle-packed cartridges (see Figure 1.10, Inset A) features high flow resistance with consequent limited ability to shorten chromatography run times, increased back pressure, limited lifetime of pumps, seals and column and the possible bed splitting is shortening column life and reducing reproducibility. The monolithic column (see Figure 1.10, Inset B) features shorter run times, lower back pressures, less stress on the system and column, high flow rates due to high porosity, no inlet bed settling, increased reliability, reproducibility, and lifetime.

It is interesting to analyze the Inserts C, D and E in Figure 1.10: The same starting materials are used to prepare both particle based bed and monolithic bed. In particular, (see Inset C, Figure 1.10) the pore size profiles of the two poly (EDMA-co-GMA) derived materials show the bigger pores of the monolithic material if compared to the pore of the particles based bed. These morphological differences are a direct consequence of the different polymerization conditions. For monoliths, unstirred mold conditions are used while the particles beds were produced in a colloidal (and well stirred) system. The morphology of the monoliths is, indeed, a direct consequence of the porogenic solvents used during the synthesis (effective only in unstirred molds).

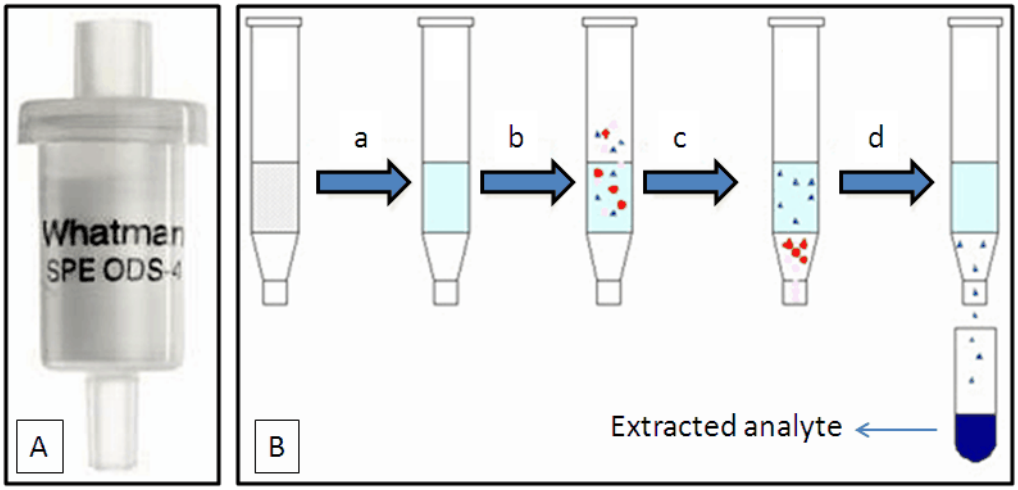

Figure 1.9: Inset A: GE Whatman 6804-0405 Solid Phase Extraction Cartridge; Inset B: SPE steps (a: solvent equilibration, b: loading, c: washing, d: elution.). The impurities are in red while the analyte of interest is in blue. The process can be performed by gravity, by centrifugation, or applying vacuum / pressure. Each cartridge is developed for a specific operative set-up.[113]

The physico-chemical mechanisms involved in the SPE techniques are essentially of the same nature as the ones involved in the liquid chromatography. Table 1.1 shows the energies involved in all the separation processes included in SPE.[114] The numbers in Table 1.1 are a useful qualitative guide to design experiments for testing and to develop new materials to be used as solid phases in a SPE process or to understand why the SPE process may, sometimes, present problems. For example it explains why the analyte final desorption (see Figure 1.8, Inset B, step d) is not always

straightforward as a strong interaction can be attractive for the loading step, but more difficult to break during the displacement phase.

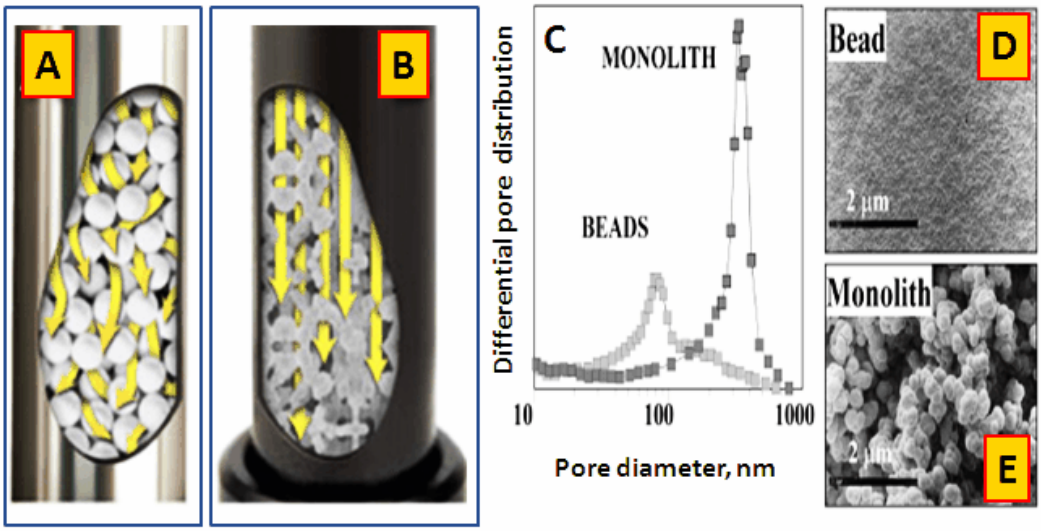

Figure 1.10: Inset A, particle-based column: mass transport ruled by diffusion processes. Inset B: monolithic porous column: mass transport ruled by convection processes. The yellow arrows visualize the different eluent pathways inside the columns.[115] Inset C: Differential pore size distribution curves of poly (EDMA-co-GMA) beads and monolith prepared from identical polymerization mixtures.[116] Inset D: Particles based polymeric solid phase SEM micrograph (Scale 2 µm). Inset E: Polymeric porous monolith phase.

Table1.1: The nature of the interaction during a SPE process

Interaction type	Energy (kcal /mol)
Dispersion	1–5
Dipole–induced dipole	2–7
Dipole–dipole	5–10
Hydrogen bonding	5–10
Ionic	50–200
Covalent	100–1000

1.5 References

[1] www.youtube.com/watch?v=4eRCygdW--c (accessed 20.05.2014)

[2] Hood, J. L.; Jallouck, A. P.; Campbell, N.; Ratner, L.; Wickline, S. A. *Antivir. Ther.* **2013**, *18*(1) , 95

[3] Thaxton, C. S.; Leo I.G. *Proc. Natl. Acad. Sci. U. S. A.* **2013**, *11*(7), 2511

[4] Shea, L.; Miller, S. *Nat. Biotechnol.* **2012**, *30*(12), 1217

[5] Jiang, T.; Mo, R.; Bellotti, A.; Zhou, J.; Gu, Z. *Adv. Funct. Mater.* **2014**, *24* (16), 2295

[6] web.mit.edu/newsoffice/2012/noninvasive-diagnostics-for-cancer-1216.html (accessed 04.04.2013)

[7]https://news.brown.edu/pressreleases/2008/05/biomedical-nanotechnology (accessed 03.04.2014)

[8] Wang, H. N.; Fales, A. M.; Zaas, A. K.; Woods, C. W.; Burke, T.; Ginsburg, G. S.; Vo-Dinh, T. *Anal. Chim.Acta* **2013**, *786*, 153

[9] Bertram, J. P.; Williams, C. A.; Robinson, R.; Segal, S. S.; Flynn, N. T.; Lavik E.B. *Sci. Transl. Med.* **2009**,*1* (11) *, 11*

[10] www.smartsilver.com/products (accessed 01.04.2014)

[11] Zhou, S.; Liu, X.; Wang, D. *Nano Lett.* **2010**, *10*(3), 860

[12] Sinha, A. K.; Suzuki, K.; Takahara, M.;Azuma, H., Nonaka, T.; Fukumoto, K. *Angew. Chem. Int. Ed*. **2007**, *46*, 2891

[13] Covington, M. *Phys. Rev. Lett.* **1997***, 79*, 277

[14] Derjaguin, B.; Landau, L. *Acta Physicochim. URSS* **1941**, 14, 633

[15] Helmholtz, H. *Ann. Phys. (Berlin, Ger.)* **1853***,* 165, *6*, 211

[16] Brett, C. M.A.; Brett, A. M. O. Electrochemistry: principles, methods, and applications.
Oxford Univ. Press: Oxford, UK, **1993**

[17] Bard, A. J.; Faulkner, R. F. Electrochemical methods, 2nd ed., John Wiley: New York, **2000**

[18] Pearson, R. *Chem. Rev.* **1990**, *90* (5), 813

[19] Israelachvili, J. N. *Intermolecular and Surface Forces* **,** Academic Press: San Diego, USA, **1992**

[20] Drelich, J.; Long, J.; Xu, Z.; Masliyah, J. *J. Colloid Interface Sci.* **2006**, *303*, 627

[21] Ninham, B. W. *Adv. Colloid Interface Sci.* **1999**, *83*, 1

[22] Stöber, W.; Fink, W.; Bohn, E. *Colloids Interface Sci. Ser.* **1968**, 26, 62

[23] Nyffenegger, R.; Quellet, C.; Rickla, J. *Colloids Interface Sci. Ser.* **1993**, 159, 150

[24] Yamauchi, H.; Ishikawa, T.; Kondo, S. J. *Colloids Surf.* **1989**, 37, 71

[25] Osseo-Asare, K.; Arriagada, F. *J. Colloids Surf.* **1990**, 50, 321

[26] Espiard, P.; Mark, J. E.; Guyot, A. *Polym. Bull.* **1990**, 24, 173

[27] Davis, T. M.; Snyder, M. A.; Krohn, J. E.; Tsapatsis, M. *M. Chem. Mater.* **2006**, 18, 5814

[28] Snyder, M. A.; Lee, J. A.; Davis, T. M.; Scriven, L. E.; Tsapatsis, M. *Langmuir* **2007**, 23, 9924

[29] Khaskin, I. G. *Dokl. Akad. Nauk SSSR* **1952**, 85, 129

[30] McNeil, K. J.; Di Caprio, J. A.; Walsh, D. A.; Pratt, R. F. *J. Am. Chem. Soc.* **1980**, 102, 1859

[31] Pohl, E. R.; Osterholtz, F. D. Molecular characterization of composite interfaces, eds. H. Ishida and G. Kumar, Plenum: New York, p. 157, **1985**

[32] Vorankov, M. G.; Mileshkevich, V. P.; Yuzhelevski, Y. A. The siloxane bond, Consultants Bureau, New York, **1978**

[33] Schmidt, H.; Scholze, H.; Kaiser, A. *J. Non-Cryst. Solids* **1984**, 63, 1

[34] Brinker, C. J.; Keefer, K. D.; Schaefer, D. W.; Assink, R. A.; Kay, B. D.; Ashley, C. S. *J. Non-Cryst. Solids* **1984**, 63 , 45

[35] Iler, R. K. The chemistry of silica, Wiley: New York, **1979**

[36] Pohl, E. R.; Osterholtz, F. D. Molecular characterization of composite interfaces, eds. H. Ishida and G. Kumar, Plenum: New York, p. 157, **1985**

[37] Bergna, H. E.; Roberts, W. O. Colloidal Silica, Fundamentals and Application, Surfactant Science Series, vol. 131, chapter 5, CRC Taylor & Francis: New York, **2006**

[38] Brinker, C. J.; Scherer, G. W. Sol-Gel-Science, The Physics and Chemistry of Sol-Gel-Science, Academic Press: San Diego, **1990**

[39] Iler, R. K. The chemistry of silica, Wiley: New York, **1979**

[40] La Mer, V. K. ; Dinegar, R. H. *J. Amer. Chem. Soc.* **1950**, 72, 4847

[41] Bogush, G. H.; Zukoski, C. F. *Colloids Interface Sci. Ser.* **1992**, 142, 19

[42] Bailey, J. K.; Mecartney, M. L. *Colloids Interface Sci. Ser.* **1992**, 63, 151

[43] Iler, R. K. The chemistry of silica: solubility, polymerization, colloid and surface properties, and biochemistry; eds. Wiley: New York, **1979**

[44] Keefer, K. D. Better ceramics through chemistry II, eds. C.J. Brinker, D.E. Clark and D.R. Ulrich, Mat. Res. Soc.: Pittsburgh, p. 295, **1986**

[45] Ostwald, W. *Zeitschrift für physikalische Chemie* **1897**, **22,** 289

[46] Hofmann, U.; Endell, K.; Wilm, D. *Angew. Chem.* **1934**, *47*, 539

[47] Carman, P. C. *Trans. Faraday Soc.* **1940**, *36*,964

[48] Yaroslavsky, N. G. *Zh. Fiz. Khim* **1950**, 24, 68

[49] Yaroslavsky, N. G.; Terenin, A. N. *Dokl. Akad. Nauk SSSR* **1949***, 66*, 885

[50] Kiselev A.V. (Ed.), Surface Chemical Compounds and Their Role in Adsorption Phenomena **1957**, Moscow State University Press, Moscow, pp 90 and 199

[51] Zhuravlev, L. T. *Colloids Surf. A* **2000**, *173*, 1

[52] Brunauer, S. *The Adsorption of Gases and Vapors*, vol. 1, Princeton University Press: Princeton, NJ, **1945**

[53] Kiselev, A. V.; Korolev, A.; Petrova, R. S.; Shcherbakova, K. D. *Kolloidn. Zh.* **1960**, *22*, 671

[54] Kato, M.; Kamigaito, M.; Sawamoto, M.; Higashimura, T. *Macromolecules* **1995**, *28*, 1721

[55] Wang, J.; Matyjaszewski, K. *J. Am. Chem. Soc.***1995**, *117*, 5614

[56] Szwarc, M.; Levy, M.; Milkovich, R. *J. Am. Chem. Soc.* **1956**, *78*, 2656

[57] Szwarc, M. *Nature* **1956**, *178*, 1169

[58] Otsu, T.; Yoshida, M. *Makromol. Chem. Rapid Commun.* **1982**, *3*,127

[59] Otsu, T.; Yoshida, M.; Tazaki, T. *Macromol. Chem. Rapid Commun.* **1992**, *3*, 133

[60] Oka, M.; Tatemoto, M. *Contemporary Topics in Polymer Science***,** vol. 4, Plenum: New York; **1984**, p 763

[61] Solomon D. H.; Rizzardo, E.; Cacioli, P. *Polymerization Process and Polymers Produced Thereby*, U.S. Patent Number 4,581,429, **1986**

[62] Druliner, J. D. *Macromolecules* **1991**, *24*, 6079

[63] Georges, M. K.; Veregin, R. N.; Kazmaier, P. M.; Hamer, G. K. *Macromolecules* **1993**, *26*, 2987

[64] Mardare, D.; Matyjaszewski, K. *Macromol. Rapid Commun.* **1994**, *15*, 37

[65] Greszta, D.; Mardare, D.; Matyjaszewski, K. *Macromolecules* **1994**, *27*, 638

[66] Mardare, D.; Matyjaszewski, K. *Macromolecules* **1994**, *27*, 645

[67] Szwarc, M. *Nature (London)* **1956**, *178*, 1168

[68] Lena, F.; Matyjaszewski, K. *Prog. Polym. Sci.* **2010**, *35*, 959

[69] Tang, W.; Kwak, Y.; Braunecker, V.; Nicolay, V.; Tsarevsky, M.; Coote, M. L.; Matyjaszewski, K. *J. An. Chem. Soc.* **2008**, *130*, 10702

[70] Matyjaszewski, K; Xia, J. *Chem. Rev.* **2001**, *101*(9), 2921

[71] Matyjaszewski, K.; Tsarevsky, N. V. *Nat. Chem.* **2009**, *1*(4), 276

[72] Fischer, H. *Chem. Rev.* **2001**, *101*, 3581

[73] Tang, W.; Tsarevsky, N. V.; Matyjaszewski, K. *J. Am. Chem. Soc.* **2006**, *128*, 159

[74] Seeliger, F.;Matyjaszewski, K. *Macromolecules* **2009**, *42*(16), 6050

[75] Wang, Y; Schroeder, H.; Morick, J.; Buback, M.; Matyjaszewski, K. *Macromol. Rapid. Commun.* **2013**, *34*(7), 604

[76] Matyjaszewski, K.; Kajiwara, A. *Macromolecules* **1998**, *31*, 548

[77] Fisher, H. *Chem. Rev.* **2001,** *101,* 3581

[78] Tsarevsky, N. V.; Matyjaszewski, K. *Chem. Rev.* **2007**, *107*, 2270

[79] Matyjaszewski, K.; Jakubowski, W.; Min, K.; Tang, W.; Huang, J.; Braunecker, W. A.; Tsarevsky, N. V. *Proc. Natl. Acad. Sci. U. S. A.* **2006**, *103*(42), 15309

[80] Jakubowski, W.; Min, K.; Matyjaszewski, K. *Macromolecules* **2006**, *39*, 39

[81] Jakubowski, W.; Matyjaszewski, K. *Angew. Chem.* **2006**, *45*, 4482

[82] Matyjaszewski, K.; Dong, H.; Jakubowski, W.; Pietrasik, J.; Kusumo A. *Langmuir* **2007**, *23*, 4528

[83] Hennion, M. C. *J. Chromatogr. A* **1999**, 856, 3

[84] Colin, F.; Poole, C. F.; Ajith, D.; Gunatilleka, G. R. *J. Chromatogr. A* **2000**, 885, 17

[85] Żwir-Ferenc, A.; Biziuk, M. *Polish J. of Environ. Stud.* **2006***, 15(5), 677*

[86] Di Corcia, A.; Marchetti, M. *Anal. Chem.* **1991**, 63, 580

[87] Bigley, F. P.; Grob, R. L. *J. Chromatogr.* **1985**, 60, 407

[88] Maskarinec, M. P.; Manning, D. L.; Harvey, R. W. *J Chromatogr*. **1984**, 302, 51

[89] Anastassiades, M.; Lehotay, S. J.; Schenck, F. J. *J. AOAC Int.* **2003** , *86*(2), 412

[90] Lehotay, S. J.; de Kok, A.; Hiemstra, M.; Van Bodegraven, P. *J. AOAC Int*. **2005**; *88*(2), 595

[91] Lehotay, S. J.; Mastovska, K.; Lightfield, A. R. *J. AOAC Int.* **2005**; *88*(2): 615629

[92] Lehotay, S. J. *Proceedings AOAC Annual Meeting*, St. Louis, MO, U.S.A., **2004**

[93] Fuh, R. M.; Wu, T. Y.; Lin, T. Y. *Talanta* **2006**, 68, 987

[94] Christie, W. W. *J. Lipid Res.* **1989**, 30, 1471

[95] Industrial Report: "*Laboratory Sample Preparation Techniques: Breaking the Productivity Bottleneck - Prep Chromatography, Extraction & Concentration",* Strategic Directions International Inc., Los Angeles, CA, U.S.A., **2012**

[96] Unger, K. K.; Skudas, R.; Schulte, M. *J. Chromatogr. A* **2008**, 1184, 393

[97] Svec, F. F. *J. Chromatogr. A* **2010**, 1217, 902

[98] Vladh, E. G.; Tennikova, T.B. *J.Chromatogr. A* **2009**, 1216, 2637

[99] Guiochon, G. *J. Chromatogr. A* **2007**, 1168, 101

[100] Nordborg, A.; Hilder, E. F. *Anal. Bioanal. Chem.* **2009**, 394, 71

[101]Svec, F. *J. Sep. Sci.* **2004**, 32, 3

[102] Michael, W. H.; Roberts, C. M.; Ongkudon, G. M.; Danquah, M. K. *J. Sep. Sci.* **2009**, *32*(15-16), 2485

[103]Li, X.; Zhi-Guo, S.; Yu-Qi, F. *Anal. Bioanal. Chem.* ***2011****, 399*(10)*,* 3345

[104] Noel, R.; Sanderson, A.; Spark, L. Cellulosics, in "Materials for selective separations and other techniques", J.F. Kennedy, G.O. Phillips, P.A. Williams Eds: New York, pp. 17-24, **1993**

[105] Svec, F. *J. Sep. Sci.* **2004,** 27, 747

[106] Viklund, C.; Svec, F.; Frechet, J. M. C.; Irgum, K. *Chem. Matter.* **1996**, 8, 744

[107] Nordborg, A.; Hilder, E. F. *Annu. Rev. Anal. Chem.* **2004**, 4, 197

[108] Peters, E. C.; Petro, M.; Svec, F. ; Frechet, J. M. *J. Anal. Chem.* **1997**, 69, 3646

[109] Svec, F. *J. Sep. Sci.* **2004**, 27, 1419

[110] Eeltink, S.; Geiser, L.; Svec, F.; Frechet, J. M. J. *J. Sep. Sci.* **2007**, 30, 2814

[111] Vlakh, E.; Tennikova, T. *J. Sep. Sci.* **2007**, 30, 2801

[112] Wu, R.; Hu, L.; Wang, F.; Ye, M.; Zou, H. *J. Chromatogr. A* **2008**, 1184, 369

[113] http://www.gelifesciences.com (accessed 20.06.2014)

[114] Hennion, M. C. *J. Chromatogr. A* **1999**, 856, 3

[115] http://chromservis.cz/group/stationary-phases (accessed 08.03.20130)

[116] Svev, F. *J. Sep., Sci.* **2004***,* 27, 747

Chapter 2: A practical users' manual for the synthesis of well-defined and colloidally stable silica nano-particles

2 The Stöber method (SM) and the seed growth method (SGM): Two easy ways for the synthesis of nano-particles

In 1956, Kolbe described for the first time the formation of silica particles by reacting tetraethyl silicate in alcoholic solutions with water in the presence of certain bases. [1] He observed the formation of spherical silica nano-particles. However, the experimental conditions were not well established and most of the times the final product was just a gel and the nano-particles formation was a side product. Based on this first experimental evidence, Werner Stöber and Arthur Fink in the Department of Radiation Biology and Biophysics, Medical School, University of Rochester, and Ernst Bohn in the Max-Planck-Institut für Experimentelle Medizin, Gottingen, Germany, disclosed for the first time a systematic study of the parameters for these kinds of reactions. [2] The reagents and the parameters involved in this seminal study are listed in Table 2.1. For the first time, the controlled growth of spherical silica particles of uniform size was possible by means of hydrolysis of alkyl silicates and subsequent condensation of silicic acid in alcoholic solutions. Particle sizes obtained in suspension ranged from less than 50 nm up to 2 μm in diameter with a high morphological uniformity. With the use of electron microscopes the uniform shape and size of the silica nano-particles was confirmed. To be noted, this high uniformity was possible by simple mixing of reagents and the use of a thermal baths. In Figure 2.1 there is the graph summarizing how the [NH_3] and [H_2O] relates to the spherical nano-particles diameter when the tetraethyl orthosilicate (TEOS) concentration is 0.280 M.**Erreur ! Signet non défini.**

As the reaction proceeds, the silicate esters in the initially clear colorless alcohol/water solution are hydrolyzed forming a super saturated solution of salicic acid. In this stage the solution starts to show a typical opalescence due the formation of the nano-particles. The simple observation of this opalescence can be used as the first easily accessible indicator to judge the completeness of the nano-particles formation.

A typical example is depicted in Figure 2.2 showing frames of the same system taken at time intervals from an author's experiment. The more and more pronounced opalescence of the reaction solution with time can easily be seen. The stability of the alcosol is evident from the fact that no sedimentation or aggregation of the nano-particles has been observed during one year or more.

Table 2.1: Reagents and the parameters involved in the original Stöber method

Reagent - Parameter	Note
Alcohols	MeOH, EtOH, n-Propanol and their mixtures
Ammonia	Saturated alcoholic solutions, titrated just before use,[NH_3] range = 0 – 8 M
Water	[H_2O] range = 0 – 15 M
Alkyl silicates (TEOS)	[TEOS] = 0.280 M
Temperature	Room Temperature and isothermal conditions
Time	Variable with concentrations, 1 min to hours

Some general trends can be observed in the Stöber method [2]:

- Reaction rates slow down with increasing of molecular weight of the alcohols used. Nano-particle diameter is increasing with the molecular weight of the alcohols used (being other reaction parameter unmodified).
- The nano-particles shape uniformity is decreasing with the molecular weight of the alcohols used and more uniform shape can be reached using alcohol mixtures.
- The condensation rate depends strongly upon the water content of the system: maximum particle size was obtained at water concentrations around 6 M.
- In the absence of ammonia, the silica flocculates in irregularly shaped particles and no spheres could be observed in electron microscopy. Thus,

ammonia apparently influenced the morphology, and creates spherical particles whenever it was present during the reaction.

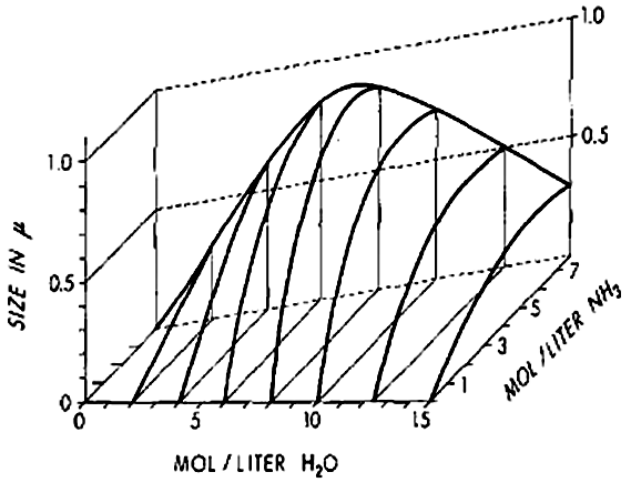

Figure 2.1: [NH_3] and [H_2O] vs. nano-particles diameter[23]

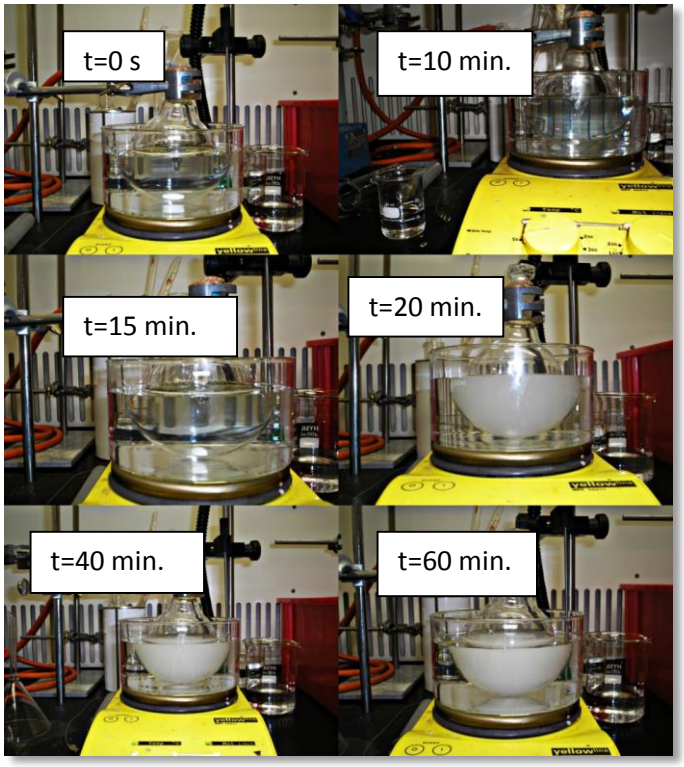

Figure 2.2: A system using the Stöber method conditions during the progressive silica NP formation

While the Stöber method is easy to perform and produces stable and reproducible nano-particles, a number of questions were at that time still not answered:

1) What are the actual mechanisms for the formation of the nano-particles? In particular, how it is possible, starting from silicic acid $Si(OH)_4$ to arrive at the final nano-sphere?
2) Why in each of the considered reaction conditions the final system reached equilibrium and a final nano-particles diameter? In particular, what is the role of the stabilizing forces at the interface between the silica nano-particles surface and the solution?
3) What are the best conditions to use alcosol suspensions; in particular, what are the best work-up methods able to avoid silica nano-particles damage and condensation when it is desired to decorate their surfaces?

Another appealing method for the synthesis of silica nano-particles is the "seeded growth method" (SGM). The main driving force in this research field was the need for nano-particles able to exhibit fluorescence. This is an emerging research area involving potential biological and photonic applications such as imaging, optical bar-coding, sensing, and optically-active materials.[3-8] The main synthetic problem arising when attempting the formation of silica nano-particles with a dye (or any other chemical species) embedded inside the SiO_2 network, is that the dye will never be stably trapped inside the silica nano-particle. This problem was clearly defined by van Blaederen and Vrij. [9] A number of failed tests on the absorption of the dye fluorescein isothiocyanate (FITC) involving systems of growing silica nano-particles, confirmed the need to conjugate the FITC with the orthosilicate precursors used to generate the nano-particles: Indeed, only in this case the FITC would be stably and chemically embedded in the silica network.

In SGM, the conditions of reaction are controlled in order to form an initial and fixed concentration of silica nuclei in suspension. To this system is then added, under strict conditions of flow rate the proper amount of alkoxy-silane. In this way, it is possible to reach the desired nano-particles diameter. In principle, the final products of a Stöber method derived nano-particle and a SGM derived nano-particle are the same. Nevertheless, what is very interesting in the SGM is the possibility to change the type

of alkoxy-silane used during the process. This is important to chemically link one of the 4 sites of an alkoxy-silane with the desired dye molecule enabling to cast dye-doped silica nano-particles. It also allows using several kinds of dyes or other molecules during the formation of layers. With SGM it is thus possible to synthesize multi dye-doped systems with chemically embedded molecules inside the SiO_2 network. In particular, it is possible to control the presence of dyes (or others molecules) in three different nano-particle segments: inside the nucleus, in the diverse over-imposed shells and on the surface of the nano-particles. Figure 2.3 shows an example of this kind of nano-particles (see Inset A) with FITC and a surface Ruthenium dye. [10]

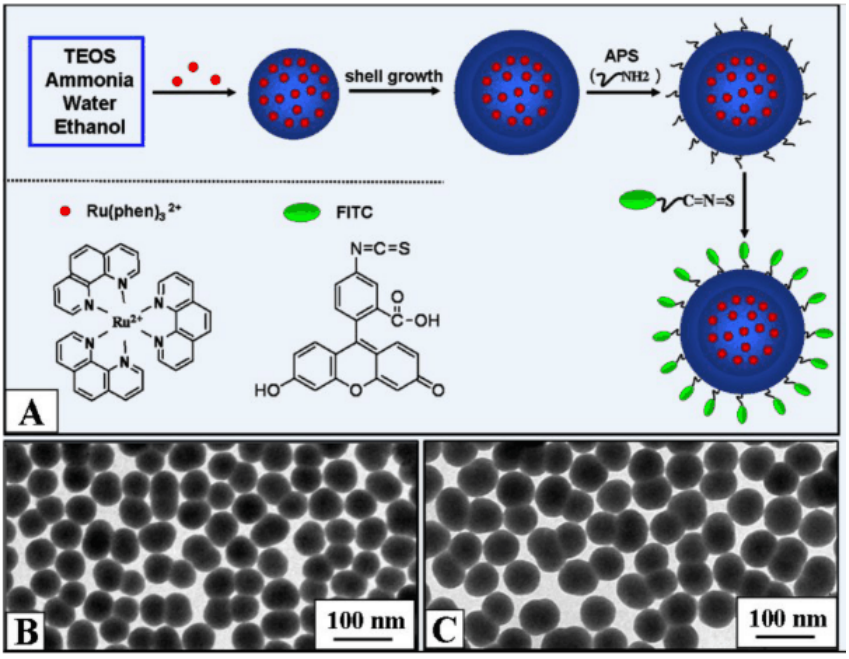

Figure 2.3: Nano-particles (see insert A) with FITC and a surface ruthenium dye. The nano-systems are compartmentalized in three zones: core, shells and surface. [11]

The SGM is a special technique where the alkoxysilane is added in aliquots and not at once. There is no new chemical reaction to be examined compared to the SM. The only difference is in the parameter time and in the lower [TEOS] involved. The technique is based on the concept of critical condensation concentration . The just-formed silica nuclei are left stabilizing for 24 hrs and then the time controlled addition

of successive aliquots of alkoxysilane will determine the increase of the particle diameter. Two of the main parameters to be considered are the time between each alkoxysilane aliquot and the concentration of alkoxysilane. Indeed, the time between each alkoxysilane aliquot must be sufficient for the development of monomers and theirs condensation, i.e. the concentration of alkoxysilane must be systematically remain under the critical condensation concentration. A higher concentration of alkoxysilane would promote the formation of new nuclei and the formation of a new population of diameters and the suspension would lose its so peculiar (and desired) mono-dispersity.

The first seminal work on the seed growth method builds on the contrast existing between of the LaMer model and the Bogush/Zukosky model to depict the phenomena related to the SM. [12]

- The LaMer model defined the picture of a surface reaction-limited particles growth where the nucleation occurs only within a short time interval at the beginning of the process and the growth happens by molecular addition of monomers to the silica nano-particle surface. On this matter very interesting is the work by Matsoukas and Gulari.[13]

- In contrast to this concept, Bogush and Zukoski defined a model based on a growth driven by the aggregation of small particles continuously generated and aggregated to form larger nano-particles supported by electrical measurements during the silica nano-particles formation. [14] In this case, self-sharpening of the size distribution is attributed to a size-dependent aggregation step. It is worthwhile to note how Bailey and Mecartney[15], using cryo-TEM technique, detected in a systematic study on SM alcosol suspensions, the ubiquitous presence of a low density 10-20 nm silica nano-particles and, above this diameter the presence of high density silica nano-particles. These experimental observations confirm the Bogush and Zukoski model meaning that oligomers and nuclei are formed continuously during the synthesis.

In this chapter are experiments correlating [NH_3] and the diameter/mass content of the Si-NPs in the context of the Stöber method and the seed growth technique are discribed. Moreover, a model to numerically define the quality of each synthesized colloids and to implement the strategies to reduce out-of-spec batches is presented.

2.1 Results and Discussion

In Figure 2.4 a graph from a Stöber`s original work on the synthesis of amorphous silica nano-particles is shown.[2]

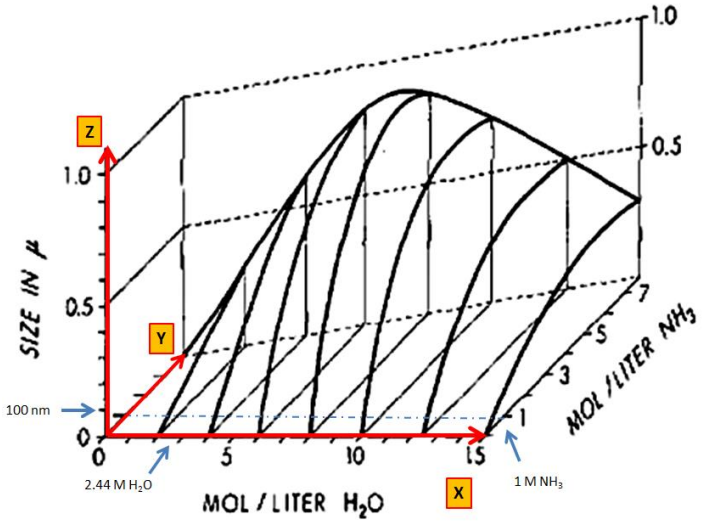

Figure 2.4: [NH_3] and [H_2O] vs. nano-particles diameter. [2] The X axis goes from 0 to 15 M in H_2O, the Y axis goes from 0 to 8 M in NH_3 and the Z axis goes from 0 to 1 µm in nano-particles diameter size. If the region of the space contained in X = 0-2.44 M, Y = 0-1 M and Z = 0-100 nm is considered (this is the region of formation of silica nano-particles with the diameters of interest in this work; to be noted, blue arrows indicate the specific points on the pertinent axes) the possibility to read on the graph the proper [NH_3] and [H_2O] value to target a nano-particle diameter from 20 to 80nm is negatively affected by the perspective of the graph. The three blue arrows (2.44 M in H2O on the OX axes, 1 M in NH3 on the OY axes and 100 nm in nano-particles diameter on the OZ axes) delimitate the region of the space considered in the Figure 2.5.

The points of this surface derive from a large number of tests and describe how the concentration of water and ammonia define the size of the silica nano-particle being the tetraethyl-orthosilicate (TEOS) concentration constant. In this graph, nano-particle diameters up to 800-1000 nm are considered. While summarising a number of facts and data pertinent to this technique, this graph would be not particularly

handy to be used in the practical laboratory activity as a graphical/numerical tool to make decisions on the relevant concentrations to target a specific nano-particle diameter. The use of this graph is in a way questionable if a reliable correlation between concentrations and diameters is needed in order to plan the nano-particle synthesis. Indeed, the used perspective deforms the shape of the shown surface and, moreover, in the diameter range from 0 to 100 (see the lower left corner in Figure 2.4), the readability is actually poor. Moreover, in Stöber's paper no direct numerical model or tool it is presented to be used for this purpose.[2] The first part of the data presented in this discussion is intended to solve this specific operative problem. In particular, the region of the graph defined by X = 0 – 2.44 M in H_2O, Y = 0 – 1 M in NH_3, Z = 0 – 100 nm is considered (see the Figure 2.5). The plane passing through the points O Z Z_1 Y_1 cuts the discussed curve defining a pathway going from O to Z_1. The projection of this curve on the plane passing through X Y_1 Z_1 is the graphical and numerical model discussed and defined in this study. The red curve XZ_1 in Figure 2.5 is actually the numerical model under discussion.

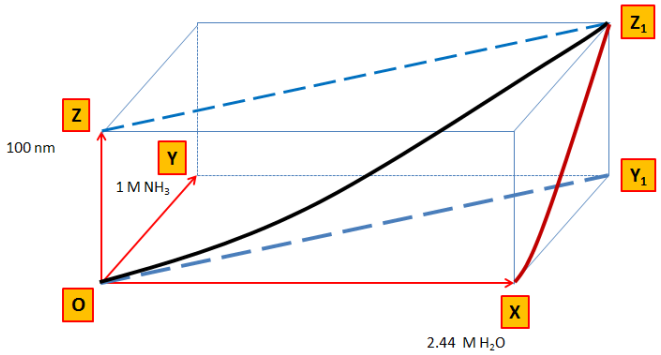

Figure 2.5: The X = 0 – 2.44 M in H_2O, Y = 0 – 1 M in NH_3, Z = 0 – 100 nm sub-region of the graph in Figure 2.5 is presented (the surface in Figure 2.5 is actually not explicitly showed). The black curve O Z_1 is the intersection of the plane passing in O Z Z_1 Y_1 with the curve showed in the Figure 2.5. The red curve passing in X Z_1 is the projection of the black curve on the plane passing in X Z_1 Y_1. The angle formed by the plan O Z Z_1 Y_1 and the axes OX is defined by the $[NH_3]/[H_2O]$ ratio (0.41). The value $[NH_3]/[H_2O]$= 0.41 is an arbitrary choice hold during all the discussion.

This curve is statistically defined as the best fit curve of 5 repeated tests. Specifically, five Stöber syntheses were performed varying $[NH_3]$ from 0.2 to 1.0 M at fixed [TEOS]= 0.280 and $[NH_3]/[H_2O]$= 0.41. For each system, the diameter of the formed silica nano-particles is measured by dynamic light scattering (DLS). These five correlated systems under study have been, at the same time, used to measure the

mass of the silica nano-particles in the final colloidal suspensions (expressed as mg of nano-particles per mL of alcosol) and the zeta potentials in mV. These two measurements require specific operative procedures. In order to measure the mass content, the proper cleaning of the colloidal batches need to be assured so to eliminate any intermediate TEOS derived oligomer present as this not particle-correlated mass would give a systematic error on the mass determination as detailed in the experimental section. On the other hand, monitoring of the zeta potential implies to work at a well-defined and stable pHs.

Table 2.2 shows the set of data (defined as set SM) deriving from these five systems. While the corresponding experimental points in Figure 2.6 show the [NH_3] vs. diameter (on the left) and mass content (on the right) correlation graphs derived from the mentioned statistical regressions (red lines).

For the SGM, similarly, three systems were examined at different tetraethyl orthosilicate concentrations ([TEOS] = 50, 100 and 150 mM). In each one of these systems, the ammonia concentration is varied ([NH_3] = 0.2, 0.4, 0.6, 0.8 and 1.0 M) and, as in the SM case, nano-particles diameter, mass content and zeta potential was measured. This data is defined as SGM1, 2 and 3 for the [TEOS] = 50, 100 and 150 mM respectively. The statistical treatment is the same as in the SM case. In Table 2.3, there is the experimental data relative to set SGM1, 2, and 3. The error bars definition is the same as the SM.Figure 2.7-9, similarly to the Figure 2.6, show the experimental data for the set of data SGM1, SGM2 and SGM3 (black points and error bars) along with the the [NH_3] vs. diameter and mass content correlation graphs derived by the mentioned statistical regressions (red lines). It is important to clarify here that the SGM nano-particles display no chemical or physical difference with respect to the SM nano-particles. The only difference is in the lower concentration of TEOS used during the synthesis. Indeed, if [TEOS] is no bigger than 0.150 M, the SGM-derived amorphous silica nano-particles are susceptible of further diameter increment if the critical silica concentration is not exceeded. The diameters of these nano-particles can be incremented by adding, at the proper rate, aliquots of fresh TEOS and for this reason the method is defined as “seeded growth method”. In fact, these SGM-derived nano-particles are seen as seeds to be grown by superposition of further silica

shells. These just discussed graphs are intended to be a direct visual tool to define the experimental parameters in any future SM and SGM test. If, for example, a silica nano-particle with a diameter of 50 nm is desired, it is now possible to derive from these graphs the proper [NH_3], [TEOS]. In a specific case, from Figure 2.6, a 50 nm diameter would correspond [NH_3] =0.8 and [TEOS] =100 nm. Moreover, the error bar on the expected diameter populations can be estimated. The same kind of graphical derivation of experimental parameters is also clearly applicable for the expected mass content per mL. To be explicitly noted here, the DLS method used, the Contin algorithm, implies growing error bars for bigger diameters due to the specific numerical data treatment. It is here important to clarify how, in the set of data SM, SGM1, 2, and 3 the zeta potentials are all measured under the same conditions (0.1 M Bis-Tris buffer solution at pH 9.0) but, on the other hand, if the specific work up conditions are considered, the systems differs if different diameters are considered and for this reason the values are not strictly comparable. Indeed, two different work-up methods (dialysis for "small" diameters and centrifugation for "large" diameters) were used. For this reason the small decrease in zeta potentials with the diameter increase valid for all the four sets of data should not be used to define simplistic correlation models. Nevertheless, the zeta potential ranges are confirming the good colloidal stability of the studied systems. These white opaque suspensions were stable for 1 to 2 years in a well-sealed hydrofluoric acid pre-treated and cleaned glasses jar with no macroscopic signs of aggregation. Eventually, at the nano-scale, aggregates are detectable by electron microscopy. The mathematical description of the graphical modeling is further detailed in Table 2.4, listing coefficients and error bars for the sets SM, SGM1, 2 and 3. It is worthwhile to note how the adjusted R^2 coefficients of determination (see table 2.5) are confirming the quality of the fits on the statistical point of view (*Note: The goodness of fit can be evaluated by coefficient of determination, R^2. See Origin 8® Reference in Polynomial fit*). With the analysis of the statistical models presented in the table 2.4 and 5 is completed the first part of this critical survey of the Stöber and seeded growth methods to synthesize silica nano-particles. For the first time in the literature, the graph from the seminal Stöber publication[2] is more easily readable in both graphical way (by visual inspection of the just furnished graphs) and analytical way (by using the derived statistical models).

Table 2.2: Experimental data for the Stöber Method (Set SM) (Note: Each experimental value for the diameter and error bar is the mean of 10 repeated tests and each test is based on 270 averaged scans. Similarly, the experimental values of the mass content and error bar determination are based on the mean of 10 repeated tests on each of the 5 systems. The error on ammonia and TEOS concentration (kept constant at 0.280 M) is assumed to be null. In each of these five tests the $[NH_3]/[H_2O]$ = 0.41 is kept constant as in all the tests discussed in this study.

Set SM: Stöber method derived systems				
Test	$[NH_3]$, mol/L	Nano-particles diameter, nm	Nano-particles mass per mL of alcosol, mg/mL	Zeta potential at pH=9.0, mV
1	0.2	10.53±1.53	22.0±0.05	-42
2	0.4	22.00 ±2.93	22.4±0.05	-38
3	0.6	32.67 ±5.57	22.7±005	-38
4	0.8	43.07±7.60	22.90±0.05	-40
5	1.0	53.03 ±9.93	23.08±0.05	-35

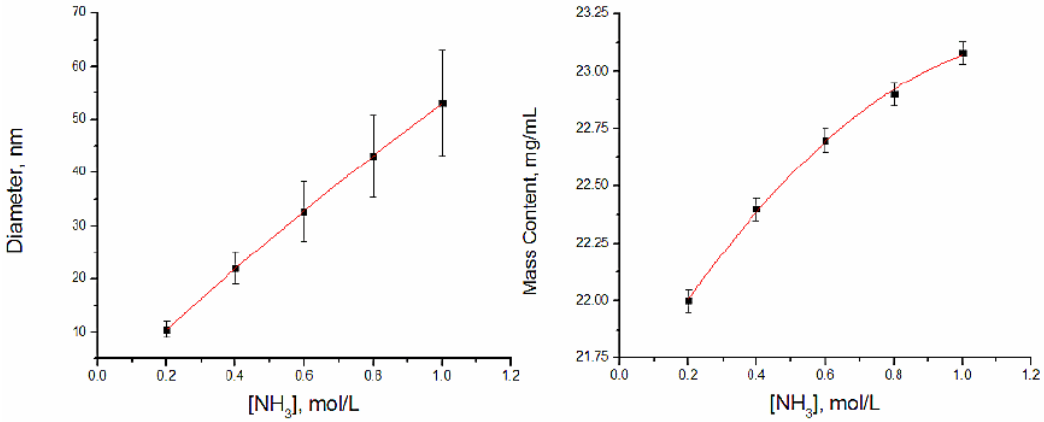

Figure 2.6: Set SM ([TEOS] = 0.280 M; from the data in Table 2.2). Experimental points and error bars (in black) for diameter (left-hand side) and mass content (right-hand side) vs. $[NH_3]$ (these are the experimental points in Table 2.2). Red lines are the data fitting curves (see Table 2.4 for details on these curves). The statistically derived red curve in left side graph is the red curve under study, X Z_1 in Figure 2.5. To be noted, to a certain extent (mainly determined by the just discussed value $[NH_3] / [H_2O]$ = 0.41) the model, valid in the 20-80 nm diameter range, can be extrapolated up to almost 200 nm diameters. Indeed, as per visual inspection of Figure 2.4, the just defined mathematical models (a monotone mathematical function of the second order) will be perfectly valid. Of course, for $[NH_3] / [H_2O] > 0.41$ and diameters bigger than 200 nm other similar models can be derived by a new set of experiments.

Table 2.3: The experimental data for the Seeded Growth Method (SGM)

Seeded Growth Method: experimental data, [TEOS]=0.050 M (SGM1)				
Test	$[NH_3]$, mol/L	Nano-particles diameter, nm	Nano-particles mass per mL of alcosol, mg/mL	Zeta potential at pH=9.0, mV

1	0.2	17.53±2.9	1.0±0.05	-44
2	0.4	28.30±4.67	1.5±0.0.5	-42
3	0.6	36.17±6.13	2.2±0.05	-42
4	0.8	43.37±7.47	2.79±0.05	-38
5	1.0	49.07±7.93	3.14±0.05	-35
Seeded Growth Method: experimental data, [TEOS]=0.100 M (SGM2)				
Test	[NH_3], mol/L	Nano-particles diameter, nm	Nano-particles mass per mL of alcosol, mg/mL	Zeta potential at pH=9.0, mV
6	0.2	17.23±2.57	3.66±0.05	-42
7	0.4	31.43±5.13	3.92±0.05	-43
8	0.6	44.57±7.4	4.24±0.05	-44
9	0.8	53±9.37	4.5±0.05	-38
10	1.0	58.93±10.83	4.8±0.05	-34
Seeded Growth Method: experimental data, [TEOS]=0.150 M (SGM3)				
Test	[NH_3], mol/L	Nano-particles diameter, nm	Nano-particles mass per mL of alcosol, mg/mL	Zeta potential at pH=9.0, mV
11	0.2	18.93±4.17	7±0.05	-42
12	0.4	37.07±6.33	7.9±0.05	-45
13	0.6	50.03±8.00	8.7±0.05	-39
14	0.8	59.43±10.1	9.5±0.05	-35
15	1.0	68.47±8.83	10.1±0.05	-34

The second point of this study is the diameter growth trends of the silica nano-particles. Specifically, if a stable colloidal suspension of amorphous silica nano-particles is fed with an incremental aliquot of TEOS (without reaching the silica saturation limit in order to avoid extra-added nucleation and loss of diameter mono-dispersity). Does the diameter growth feature any specific trend?

The experimental data from the Set SGM1, 2 and 3 (see Table 2.2) allows calculating the diameters growth trends if the data is re-arranged. In particular, if the test 1, 6 and 11 in Table 2.2 are reviewed, they can be considered as a single experiment at [NH_3]= 0.2 M where the [TEOS] is progressively increased from 50 mM to 100 mM up to 150 mM. The same re-organization can be made in correspondence of the [NH_3] = 0.4, 0.6, 0.8 and 1 M and five sets of data is so formed.

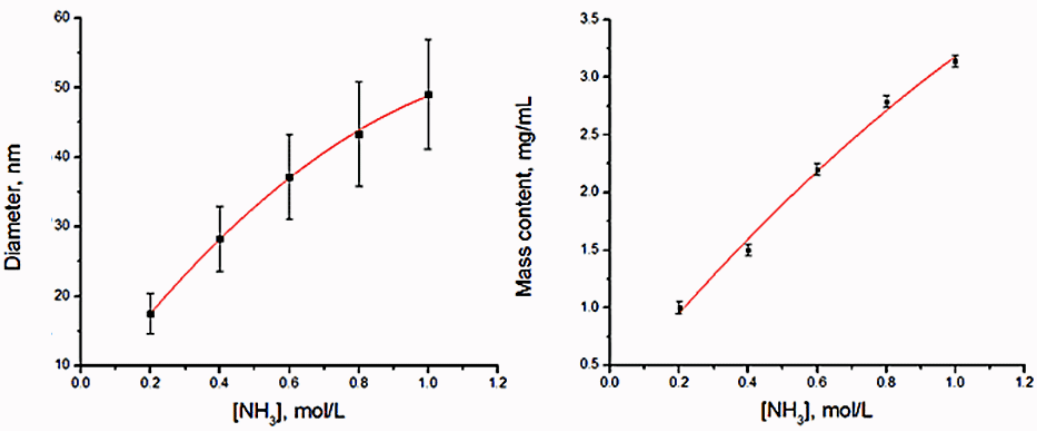

Figure 2.7: Set SGM1 ([TEOS] =50 mM): diameter (left) and mass content vs. [NH_3]. Weighed best fit curve in shown in red. (Test 1 to 5 in Table 2.3)

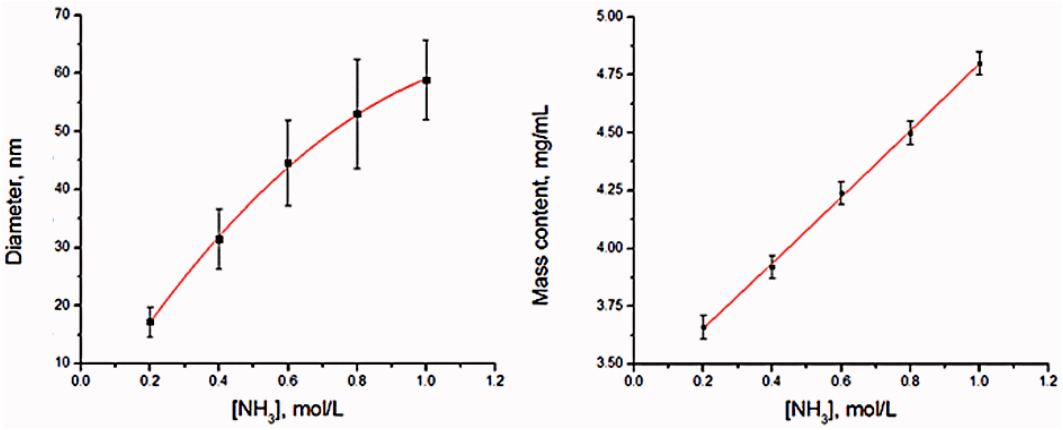

Figure 2.8: Set SGM2 ([TEOS] =100 mM): diameter (left) and mass content vs. [NH_3]. Weighed best fit curve in shown in red. (Test 6 to 10 in Table 2.3)

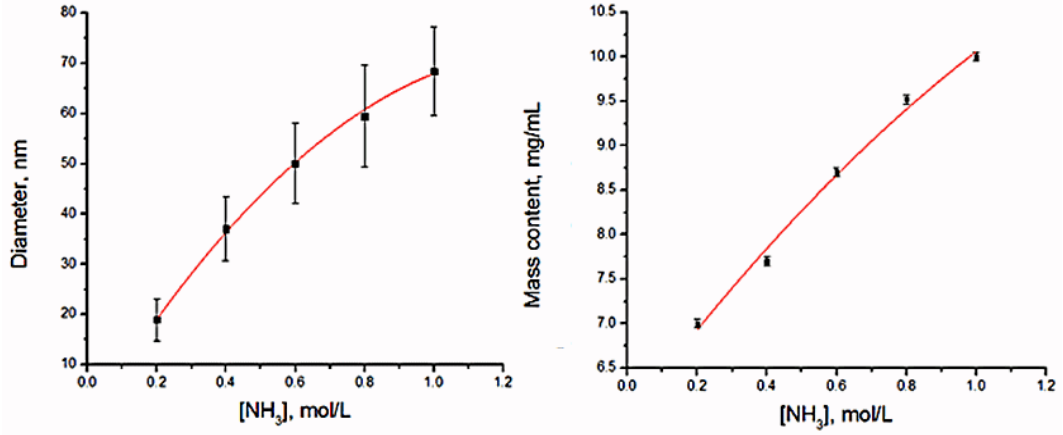

Figure 2.9: Set SGM3 ([TEOS] =150 mM): diameter (left) and mass content vs. [NH_3]. Weighed best fit curve in shown in red. (Test 11 to 15 in Table 2.3)

Table 2.4: Mathematical models for diameter/ mass content vs. ammonia concentration correlations in SM and SGM tests; weighted best fit coefficients are showed.

Mathematical modelling for diameter growth vs. [NH_3]	**Mathematical modelling for mass content growth vs. [NH_3]**
$\text{Diameter} = A + B \bullet [NH_3] + C \bullet [NH_3]^2$ A in [nm], B in [L nm/mol], C in [L^2nm/mol^2] Diameter in [nm]	$\text{Mass} = D + E \bullet [NH_3] + F \bullet [NH_3]^2$ D in [mg], E in [L nm/mol], F in [L^2nm/mol^2] Mass [mg]

Table 2.5: Weighed best fit coefficients for the mathematical models presented in Table 2.4

	Coefficients of the weighed best fit [30]	**Set SM**	**Set SGM1**	**Set SGM2**	**Set SGM3**
Diameter growth model	A, [nm]	0.000	4.961	-0.430	-1.586
	σ_A, [nm]	0.000	8.423	8.369	11.449
	B,[L nm/mol]	53.788	67.711	95.198	111.756
	σ_B, [L nm/mol]	1.179	40.284	42.104	52.783
	C, [L^2nm/mol^2]	0.100	-	-35.701	-42.259
	σ_C, [L^2nm/mol^2]	1.950	36.673	37.324	46.501
	Goodness of the fit (adjusted R^2)	1.000	1.000	0.999	0.999
Mass content model	D, [mg]	21.548	0.250	3.376	5.928
	σ_D, [mg]	0.107	0.107	0.107	0.107
	E, [L mg/mol]	2.487	3.664	1.387	5.239
	σ_E, [L mg/mol]	0.409	0.409	0.409	0.409
	F, [L^2mg/mol^2]	-0.964	-0.732	0.036	-1.107
	σ_F, [L^2mg/mol^2]	0.334	0.334	0.334	0.334
	Goodness of the fit (adjusted R^2)	0.998	0.994	0.999	0.993

The plots in Figure 2.10 show the particles diameter vs. the TEOS concentration for the 5 different ammonia concentrations obtained from Table 2.3 and it confirms graphically how a higher [NH_3] implies a higher diameters growth trends (higher

slopes). Indeed, lower diameter silica nano-particles grow at slower rates as the direct experimental evidence shows. This trend is numerically expressed by the slope of the linear fits on the experimental points in Table 2.6. This feature is in total agreement with the experimental observations, e.g., for the synthesis of 200 nm diameter silica nano-particles, the final opalescence is reached in 15-20 minutes but for 25 nm diameter silica nano-particles the final opalescence is reached in 10-15 hours.

Surprisingly, the data from the intercepts confirms that for each [NH_3] there is a minimum theoretical achievable diameter obtained by extrapolation at [NH_3]= 0 M (see Table 2.6, Intercept). This can be justified by the Bogush and Zukoski[16] model, i.e. the nano-particles grow following a process driven by the aggregation of small continuously generated particles to form larger nano-particles. Indeed, the first formed population of nano-particles (at the start of the synthesis) is actually described in terms of these minimum diameter silica nano-particles. Then, the growth in diameter is reached by progressive aggregation.

From Figure 2.10 it can also clearly be understood what the impact of an accidentally inaccurate preparation of a suspension on the final expected diameters would be. The impact of a deviation in [TEOS] on the final nano-particles diameter grows with [NH_3] while a deviation in [NH_3] would have more marked impact at lower diameters as apparent from Figure 2.7-9.

The final section of this discussion details a possible approach to detect and remediate eventual problems affecting SM or SGM derived batches. Typically, two scenarios are possible: Either the monitoring of a SM derived batch before the final time-consuming work up, or the monitoring of a SGM derived batch to increase the starting diameter of the nano-particles. In this way, at the same time, a strategy to monitor the “quality” of a batch is defined and to critically remediate the problems in future batches in the cases the batch needs to be discarded.

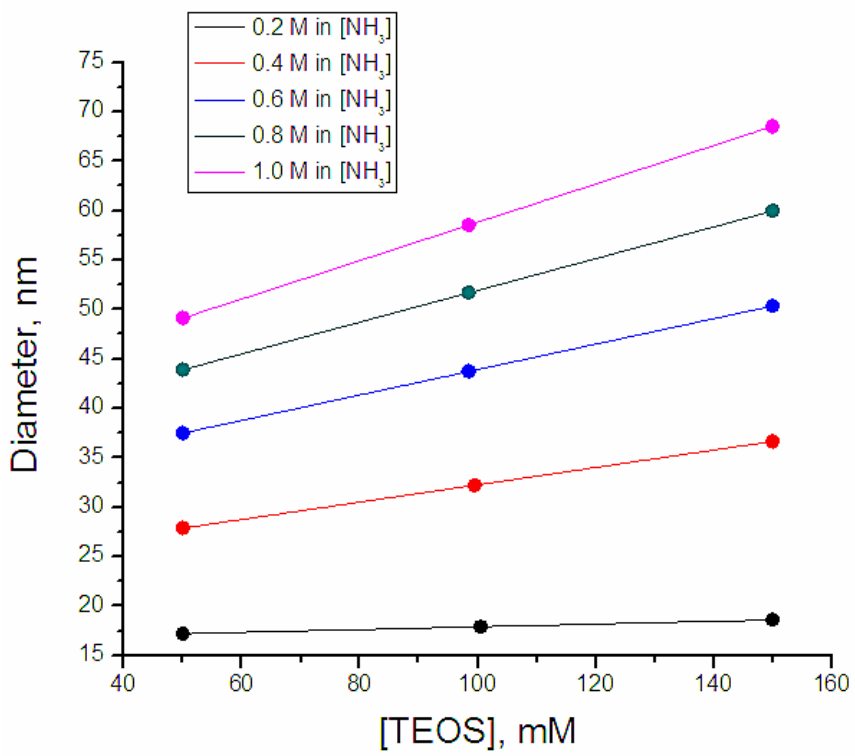

Figure 2.10: Graph derived from rearranged data in Table 2.3 (weighed linear best fit regression lines and experimental points as coloured circles)

In a stable colloidal system, the ratio between the total mass of the amorphous silica nano-particles per mL (m_t) and the mass of a single silica nano-particle in the same system (m_s) is the fixed number, n, the number of nano-particles per mL of system. After simple rearrangements (Note: Mass= Volume X density, so mass= [(4/3) πr^3 X d], being d= 2.65 g/mL, the density of the amorphous silica), it is possible to define an expression for n:

$$\frac{\text{mass}_t}{\text{mass}_s} = n = 5.0611 \bullet 10^{18} \frac{m_t}{(\phi)^3} \quad \text{(Eq.2.1)}$$

Equation 2.1: the number of nano-particles, n, must be constant in stable SM derived or SGM derived batch while the analysis of eventual deviations from n will reveal the possible remediation strategies in future batches. In eq. 2.4 m_t is in mg and Ø is in nm, the constant is expressed in nm^3/mg.

Table 2.6: Weighed linear best fit of the data in Figure 2.11. (Experimental errors are taken in account) (Note (*): This R^2 is low: at lower nano-particles diameters the experimental

interval of confidence would require a higher number of points to confirm the model; nevertheless the validity of the general discussion is not affected.

	Intercept, [nm]		Slope, [nm L/mmol]		
[NH_3], M	**Value**	**err**	**Value**	**err**	**Adj. R^2**
0.200	16.497	1.247	0.014	0.012	0.190(*)
0.400	23.497	1.565	0.088	0.014	0.947
0.600	31.063	1.210	0.129	0.011	0.985
0.800	35.873	1.996	0.161	0.018	0.974
1.000	39.423	0.200	0.194	0.002	1.000

The number n must be constant with the time both in stable SM derived bathes and during a regular nano-particles diameter growth in SGM derived batches while, if this value changes during time, this is a symptom of possible extra-nucleations or aggregations as it will be shortly clarified.

Before to start any SM/SGM batch to be monitored, from the just furnished statistical models (see Tables 2.4-5) and the known value of [NH_3], the number n can be calculated as $n_{expected}$:

$$n_{expected} = \frac{m_t}{m_s} = 5.0611 \bullet 10^{18} \frac{D + E \bullet [NH_3] + F \bullet [NH_3]^2}{\left(A + B \bullet [NH_3] + C \bullet [NH_3]^2\right)^3} \qquad \text{(Eq.2.2)}$$

Equation 2.2: $n_{expected}$ expression

The value $n_{expected}$ is a value derived by the defined statistical models in the Tables 2.4-5, a physical constant (the density d=2.65 g/mL of the amorphous silica) and the known value of [NH_3]. This value is perfectly definable before the nano-particles synthesis and no other data is needed.

Alternatively, once the colloidal system is stable at the end of the synthesis, the value n can be derived by experimental measures. In particular, n can be derived from

experimental values of m_t (mass content per mL) and m_s (mass of a single nano-particle calculated by the measure of the diameters by DLS and the value of d, the density of amorphous silica, 2.65 g/cm^3) from the equation 2.4.

In this case, n is defined as $n_{measured}$:

$$n_{measured} = \frac{m_t}{m_s} = 5.0611\ 10^{18} \frac{m_t}{(\phi \pm \Delta)^3} \qquad \text{(Eq.2.4)}$$

Equation 2.4: $n_{measured}$ expression. DLS allows determining only the whole value (ϕ+Δ); the discrimination between the pure expected diameter ϕ and its parasitic deviation Δ is the pivotal parameter for the quantitative measure of the batch quality. The value m_t is expressed in mg while (ϕ+Δ) is expressed in nm, the constant is expressed in nm^3/mg.

The comparison between $n_{expected}$ and $n_{measured}$ is the basis for the determination of the batch quality. It is now easy to monitor if more nuclei are forming during the growth ($n_{expected} > n_{measured}$, as the additional nuclei formed will reduce the average measured diameter by a factor -Δ in the equation 2.4) or if particles are aggregating during the growth ($n_{expected} < n_{measured}$, as undesired aggregations will increase the average measured diameter by a factor +Δ in equation 2.4). Figure 2.11 depicts these two deviation scenarios (red lines): the two zones of the graph are defined by the $n_{expected}$ (blue line, Δ=0): zone A (Δ>0) and zone B (Δ<0), as indicated. It is here important do explicitly note the entity of the error bars pertinent to the values $n_{expected}$ and $n_{measured}$. The $n_{expected}$ error bars are typically in the order of ± 5% of the average value as the error propagation theory suggest being the $n_{measured}$ typically in the same range if enough data is collect on the diameters. Figure 2.11 summarize this point of the discussion in the case of a SGT but the same is applicable to a SM derived batch.

The corrective strategies for the two scenarios to avoid out-of-specifications batches are so defined. In the case of SGM-derived batches, if a systematic trend for extra-nucleation is present ($n_{expected} > n_{measured}$), the TEOS dropping rate have been too fast or, if there are un-desired post aggregations ($n_{expected} < n_{measured}$), the centrifugation

times/forces or the batch concentration in [TEOS] have been too high with respect to the critical silica concentration while, in the case of SM-derived batches, if a systematic trend for extra-nucleation is present ($n_{expected} > n_{measured}$), some residual TEOS continued to produce new sub-diameter nuclei (this is typically due to a not accurate work up of a not proper pH storage conditions (see the experimental part on that matter), or, if there are un-desired post aggregations ($n_{expected} < n_{measured}$) the wrong pH, mass content of nano-particles per mL or too much prolonged centrifugations or ultra-sonication have been applied.

To show a practical working example of this strategy, a SM derived batch was prepared in ethanol with [TEOS]= 0.280 M, [NH_3]= 0.8 M and [NH_3]/[H_2O] = 0.41 (see Table 2.7).

Finally, to conclude this discussion, a second real example, on SGM derived batch, monitored using this approach is showed in the Table 2.8.

Specifically, a SGM derived batch was done at [TEOS]= 0.150 M, [NH_3]= 0.6 M, [NH_3]/[H_2O] = 0.41 then, everything left constant, the ammonia concentration was increased to [NH_3]= 0.8 M in order to increase the nano-particles diameter from 50 to 60 nm.

To be noted, in the case of the SGM derived batches, it is possible to compare the amount of nano-particles obtained by diameter growth during the SGM (conditions: [TEOS]= 0.150 M, [NH_3]= 0.6 M (starting conditions) to [NH_3]= 0.8 M (end of diameter growth conditions), [NH_3]/[H_2O] = 0.41) with the amount of directly formed nano-particles of the same diameter (conditions: [TEOS]= 0.150 M, [NH_3]= 0.8 M (, [NH_3]/[H_2O] = 0.41).

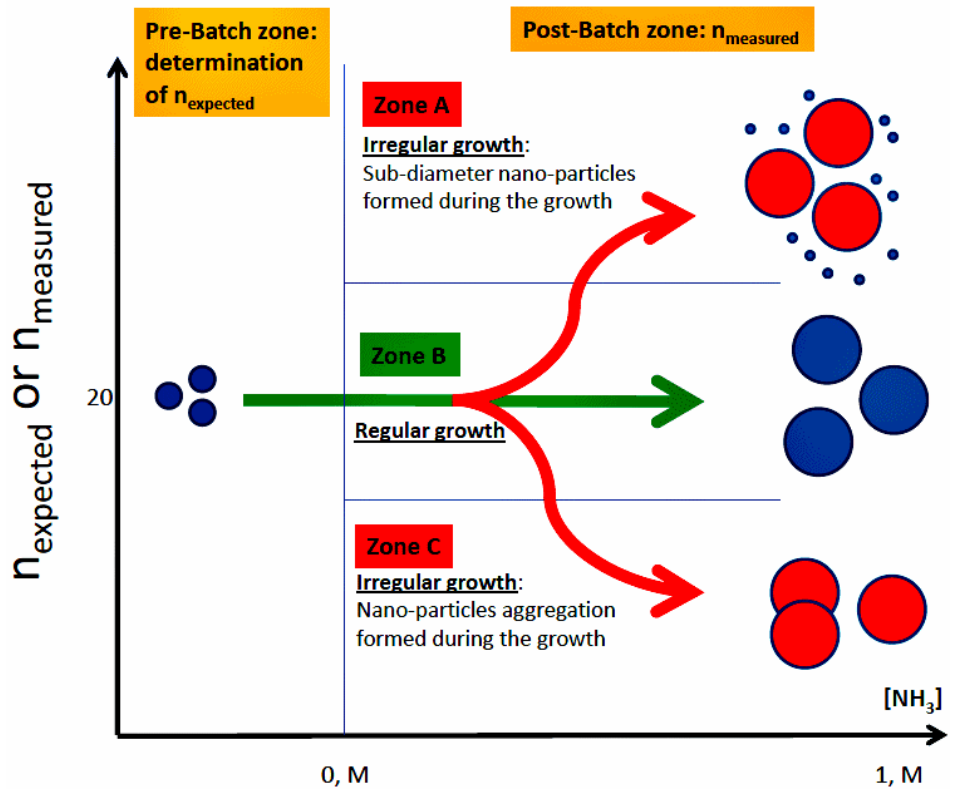

Figure 2.11: How to diagnose extra-nuclei formation (see Zone A) or aggregation (see Zone C) along a set of SGM experiments (n=20 as an example). On the left side of this scheme, the situation before the synthesis is considered (see the pre-batch zone, yellow frame on top left side): [NH_3] is known, the number $n_{expected}$ is so calculable (in this graph n=20 as an example). On the right side (see the post-batch zone, yellow frame on top right side)of the scheme, at the end of the SGM derived batch, m_t and (Δ+Ø) are measured so, based on this data, $n_{measured}$ is calculated. If the nuclei growth regularly (see the three blue nano-particles in the middle at the right side) $n_{expected} = n_{measured}$ and Δ=0. If the nuclei tends to aggregate (see the three red nano-particles at low right side) $n_{expected} > n_{measured}$ and Δ>0 as the experimentally read value (Δ+Ø) is bigger than the expected Ø due the fact that the experimentally read values of the diameters are bigger for the aggregation. If the extra-nuclei tends to form (see the three red nano-particles at high right side) $n_{expected} < n_{measured}$ and Δ<0 as the experimentally read value (Δ+Ø) is lower than the expected Ø due the fact that the experimentally read values of the diameters are lower for the extra-nucleations. In case of SM derived batches the approach is the same but the nano-particles at the left and at the right would have the same diameter as, in this case, the eventual aggregations or extra-nucleations would happen during the batch shelf life.

The "growth" nano-particles system has a mass content of 15.3 mg/mL while the directly formed nano-particles batch would have a mass content of 9.5 mg/mL (see Table 2.3, Test 14). It is evident how the SGM allows higher TEOS consumption and, more importantly, less free TEOS (and TEOS derived oligomers) in solution if growth and directly made batches of nano-particles of the same diameter are compared: this fact has a direct impact on the work-up process. Indeed, to clean a SGM-derived growth nano-particles batches require less demanding steps if compared to directly

formed SGM-method nano-particles of the same diameter. These facts have to be carefully considered if particularly clean stock solutions of low diameter silica nano-particles are needed.

Table 2.7: A real case example of the diagnostic in a SM-derived batch is shown. In red, there is the diagnostic input data while in blue there is the output data. On the left side, there are the pre-batch conditions and the right side there are the post-batch conditions. The diagnostic allows monitoring the excellent batch stability in the limits of the used error bars (± 5% in this case). The batch shelf life is of almost one year. Conditions: [TEOS] = 0.280 M, $[NH_3]$= 0.8 M and $[NH_3]/[H_2O]$ = 0.41.

Pre Batch conditions	
$[NH_3]$	0,8
$n_{expected}$	1,45E+15

Post Batch conditions	1 day	3 months	6 months	12 months
M_t, mg	23,0	23,1	23,0	23,1
diameter, nm	42,9	43	43,1	42,9
$n_{measured}$	1,47E+15	1,47E+15	1,45E+15	1,48E+15

Table 2.8: A real case example of the diagnostic in a SGM-derived batch is shown. In red, there is the diagnostic input data while in blue there is the output data. On the left side, there are the pre-batch conditions and the right side there are the post-batch conditions. The diagnostic allows monitoring the excellent batch stability in the limits of the used error bars (± 5% in this case). The batch shelf life is of almost one year. Conditions: [TEOS]= 0.150 M, $[NH_3]$= 0.6-0.8 M and $[NH_3]/[H_2O]$ = 0.41.

Pre Batch conditions	
$[NH_3]$	0,6
$n_{expected}$	3.46E+14

Post Batch conditions	1 day	3 months	6 months	12 months
m_t, mg	15.3	15.3	15.4	15.2
diameter, nm	60.7	61.0	61.2	61.2
$n_{measured}$	3.46e14	3.46e14	3.46e14	3.46e14

2.2 Conclusions

A general model for diameter growth and mass content during the SM and SGM is presented. The rate of nuclei growth and minimum diameter achievable for given experimental condition were derived and the impact of the suspension components discussed in case of accidental man-derived deviations from the ideal process. This offers a new way to generate diagnostic and corrective strategies and robust

synthetic protocols for the synthesis of silica nano-particles. The elucidated model for the synthesis of this silica based colloidal systems has the potential to be automated with computer controlled reaction processing using automated chemical injectors/auto-samplers and on-line DLS and titration tools.

2.3 Experimental part

Materials

Absolute ethanol (ACS reagent, ≥99.5 %, 200 proof), tetraethyl ortho-silicate ≥99.0 % (GC) was distilled under vacuum and used immediately, ammonium hydroxide solution (28% NH_3 in H_2O, ≥99.99% trace metals basis), ammonia solution 7M in MeOH, distilled water, fluorescein iso-thiocyanate isomer I ~98% (HPLC) (FITC) , THF, dry Toluene on molecular sieves A4, analytical grade and acetic acid analytical grade. All chemicals were obtained from Sigma Aldrich and used as received unless otherwise noted.

Methods

Centrifugation was done using a Hettich Zentrifugen Universal 320 centrifuge (Relative Centrifugal Force range 100-9000 g (Note: g is the gravitational constant = 6.67384×10^{-11} m^3 kg^{-1} s^{-2}) , Beckman Coulter Delsa-Nano 2.21, glass stoppers, Euthech Instruments PH510 pH meter, WLL 230 LAUDA thermostatic bath, Hitachi S3400n SEM microscope , Fe-SEM with proprietary software to measure nano-particles diameters, TEM, elemental analyzer, Spectrum 100 Beckman Coulter ATR-IR, regenerated cellulose dialysis membranes from SpectraPore 3.5 kDa MWCO.

Measure of mass content, diameter and zeta potential of silica nano-particles colloids

To measure the amorphous silica nano-particles content present in each stable alcosol, two different operative procedures are used. For nano-particles with diameters lower than 40 nm, a defined volume of the final batch (typically 20 mL) is diluted 1 to 5 with distilled water and immediately dialyzed using a regenerated cellulose bag from Spectrum Labs (MWCO: 20kD) being the washing liquid 5% acetic

acid in distilled water V/V, total volume 5L overnight. For silica nano-particles close to 40 nm this purification was repeated three times, for silica nano-particles close to 20 nm, this purification was repeated 5 times. Finally, a known volume of the neutralized suspension is lyophilized and the nano-particles mass content per mL is calculated. For nano-particles with diameters bigger than 40 nm, a defined volume of the final batch (typically 20 mL) is centrifuged at the minimum possible RCF (G) and time (these two parameters have been defined by trials and mistakes by analysing the eventual residual mass content in the residual supernatant at the rotavapor equipped with a proper trap for bases (to eliminate the residual ammonia). Typical values are: 8-10 min. at 9000 rpm in the aforementioned centrifuge for the 45-50 nm silica nano-particles down to 3-5 min at 9000 rpm for the 75-80 nm silica nano-particles. This centrifugation is repeated 5 times in 5% acetic acid in distilled water after proper re-suspension of the decanted mass by shortly ultra-sonication using Cole-Parmer EW-08891-11. Finally, a known volume of the neutralized suspension is lyophilized and the nano-particles mass content per mL is calculated. All the mass determinations values are the average of ten repeated tests on ten separates batches. Statistical considerations indicate the percent error bar on these measures in the order of 2 % (so, 0.05 mg/mL) due the use of the volumetric flasks with comparable error bars and the dilutions involved.

The nano-particles diameter is measured by dynamic light scattering (DLS on the aforementioned Beckman Coulter Delsa-Nano 2.21) on a sample of suspension properly diluted 1/5 V/V in ethanol. The machine available Contin algorithm used to define the diameters distribution profile in the DLS measurements, furnishes as well the error bars affecting each specific experimental value. The samples are prepared using ethanol filtered with 200 nm syringe filters in order to minimize dust contamination. To be noted: with batches of nano-particles 30-20nm in diameter lower dilutions are used (typically 1 to 1 in ethanol.)

For the measure of the zeta potential, after cleaning cycles as per the mass determination, the nano-particles are suspended in a buffer a pH=9 (0.1 M in 2,2-Bis(hydroxymethyl)-2,2',2"-nitrilotriethanol from Sigma Aldrich). A special PP cell for

zeta potential determination was used in the Beckman Coulter Delsa-Nano 2.21 device).

Synthesis of Si nano-particles by SM

Step 1: Nano particles preparation

This protocol was tested on batches of total volumes ranging from 10 mL to 2 L. A two-neck glass round bottom flask is cleaned with 2% hydrogen fluoride[17] at room temperature for 30 minutes, rinsed with distilled water (3 times, at RT for 10 minutes each time) and absolute ethanol (3 times, at room temperature for 10 minutes each time). The flask is dried in a vacuum oven at 80° C overnight. A dried polytetrafluoroethylene (PTFE) coated magnetic stir bar (length no more than 1/3 of the max reactor diameter) is transferred into the flask and is allowed to reach room temperature attached to a line vacuum just before use (ca. 2 hours). Then, it is immediately sealed with a rubber stopper (side neck) and the main neck connected to the vacuum line. The volume of the flask should be no bigger than the 30% of the total volume of the final alcosol to prevent that the ammonia solution can saturate the reactor free volume and, in doing so, the effective ammonia concentration in the incipient suspension would be minor than planned. The alcohols used in the synthesis are distilled under CaH_2 (The drying granules should be crushed immediately before use and residues should be destroyed by careful addition of water) and used immediately. The proper amount of alcohol and distilled water (conductivity: 18 MΩ/cm) are measured by volume and pre-mixed/transferred into the reaction flask by a still cannula and vacuum. Then, ammonium hydroxide solution is weighted in a separate rubber sealed glass vial and gently transferred into the flask by a still cannula and minimum vacuum (this operation has to be as fast as possible). The system is then transferred to a thermostatic bath and gently magnetically stirred at 25° C for 30 minutes. Actual ammonium contents are measured by withdrawing small samples (1 -2 % of the total reaction volume) and titrating with 1.000 M HCl. TEOS is distilled under vacuum and the proper amount cannulated into the reaction flask. The now complete reaction system is left under gentle stirring at 25° C for 2 hours (for the bigger nano-particles diameters) to 3 days (for the lower nano-particles diameters). When the cloudy suspension is stable (visually inspection), the reaction can be

considered finished. To determine the nano-particle mass content for mL of suspension, 1.0 mL (by volumetric flask, error bar 0.025 mL) of the alcosol is treated under freeze-drying tool.

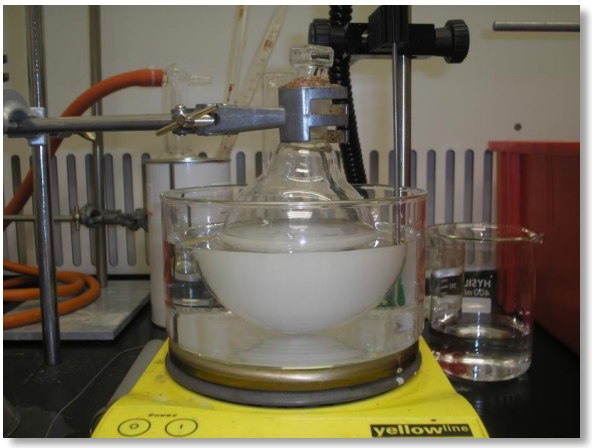

Figure 2.12: A typical batch of silica nano-particles just before the purification steps

As examples of two frequently prepared batches of bare silica nano-particles, the masses of the involved reactants are here explicitly indicated.

To prepare a 1 L alcosol batch with silica nano-particles 100 nm in diameter, 204 g of a 7M solution of ammonia in MeOH are weighed and mixed with water (81.5 g) and TEOS (58.35 g); finally, 591 mL of EtOH are added.

Similarly, to prepare a 1 L alcosol batch with silica nano-particles 200 nm in diameter, 406.5 g of a 7M solution of ammonia in MeOH are weighed and mixed with water (162.4 g) and TEOS (58.35 g); finally, 247.3 mL of EtOH are added.

Notably, the system contains as main solvent EtOH and a minor aliquot of MeOH (deriving from the 7M solution of ammonia): this had been demonstrated to be acceptable and not sensibly affecting the final nano-particles diameter. Indeed, in principle, as specified in the Stöber paper (see reference **Erreur ! Signet non défini.**), a full lower weigh alcohol batch should promote the formation of lower diameters if compared to higher alcohols but this is not the case in the systems under discussion.

To be here explicitly noted how the diameters here considered are out of the considered range (20-80 nm) but they are, more precisely, an extrapolation of the still valid models (see Table 2.3-4, values relative to the SM). The validity of the

extrapolation is based on the fact that the part of curve here used (in the range 100-200 nm) is clearly a monotonic function (see left hand down side of Figure 2.5). Indeed, for bigger diameters the just discussed lows would lose their validity and a new set of dedicated experiments should be done for the diameter bigger than 200 nm.

Step 2: Preparation of a stock solution for storage and further surface modification

The alcosol is centrifuged at 7690 RCF for 8 to 30 minutes (time varies with particles diameter, longer for smaller size). The semi-cloudy supernatant solution is discarded and the white solid is re-suspended in ethanol at ca. half of the starting original volumes using ultra-sonication in a glass vial for no more than 10 minutes. This procedure is repeated 3 times. To be noted, in each re-suspension step by ultra-sonication, a stable (not sedimenting) cloudy white suspension must be obtained in seconds. If by naked-eye inspection discrete clusters can be seen in the suspension even after ultra-sonication, the system must be discarded. In general, an easy and fast re-suspension by ultra-sonication is a sign of a still mono-disperse system.

The sediments at this stage appear as white iridescent solids. Then the sedimented solid is re-suspended in the half of volume used before with ethanol and then diluted in water at the same final solid concentration (this is the solvent exchange procedure to gently change the solvent and avoid aggregation problems during the re-suspension steps. Indeed, especially for littler nano-particles diameters, a sudden solvent change can easily promote aggregations).

After centrifugation, the solid is washed five times with water using a volume of ca. half of the original volume with respect to the starting alcosol. The re-suspension steps by ultra-sonication must be no more than 5 minutes each time. The centrifugations times are slightly longer due the higher density of water compared to the previous solvent.

Then the decanted is re-suspended in the half of the volume used before with water and then diluted with THF at the same final solid concentration (this is the second solvent exchange step). After centrifugation, the solid is washed three times with THF at the half of the final solid content.

The final iridescent white solid is left overnight at room temperature under a very gentle steam of nitrogen. The white and fragile solid is then gently grinded with a spatula to a fine white powder (few seconds are sufficient).

The fine powder is then transferred in a round bottom flask and dry toluene is added to reach half of the original volume with respect to the original stable alcosol.

Then, 2 hours at 40° C under magnetic stirring is the final conclusive step. A 0.027 % V/V in acetic acid[34] is added under magnetic stirring at room temperature a stable stock solution is formed. In the case of silica nano-particles with diameters under 60 nm, the centrifugation technique is not possible (the needs of high RCFs imply the development of aggregation). In these cases a regenerated cellulose dialysis membrane must be used. First, the ammonia content in the alcosol is eliminated at the rotary evaporator (high vacuum and water bath no more than 40° C for no more than 5 minutes). In general, it is sufficient to eliminate 3-5 % of the original volume and, immediately, to add the same volume of toluene under vigorous stirring. This system must be dialyzed immediately against toluene (0.027 % V/V Acetic Acid/Toluene[18]). The acidic toluene solution must be changed 3 times every 4 hours and then 1 time after 24 hours. To be noted, in each purification step a 100-fold volume excess of Toluene with respect to the dialyzed system must be used. In research laboratories a reasonable batch would not exceed a volume of ca. 20 mL but this is adequate for bathes with a nano-particles content of ca. 50 – 100 mg.

Synthesis of amorphous silica nano-particles by the SGT with eventual dye-enriched core

In the SGM there are two distinct steps: (A) The eventual formation of dye-rich (or shell rich) silica nuclei and (B) the controlled growth. In this specific work the conditions reported by A. van Blaaderen and A. Vrij[19] are used. In this step of the protocol, 5 nm dye rich silica nuclei are formed. A classical Stöber system as

presented in the previous section (see “Step 1: Nano particles preparation” above) but with no TEOS added is mixed with the FITC-APTES conjugate at a concentration of 18 µL of conjugate per mL of system. Then TEOS at 11.16 µL per mL of system is added. This reaction flask is left at room temperature, in the dark (an aluminium foil to wrap the flask is used), under mild stirring conditions for 24 hours.

Step (B): The controlled growth. To the core rich nuclei 4 µL of TEOS per mL of suspension is added per hour[20] using a syringe pump. The TEOS concentration is allowed to range up to 0.280 M (the concentration used in the SM) with no loss of mono-dispersity and colloidal stability. To be noted, in step (A) it is possible to form nuclei of different diameter and in B it is possible to form shells of different thickness.

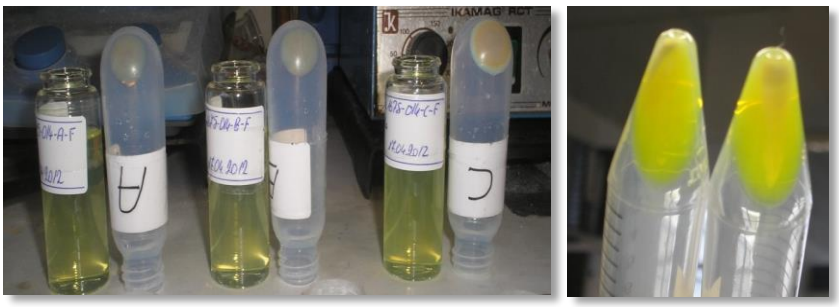

Figure 2.13: Left; three batches after the final centrifugation step of dye-core fluorescent bare silica nano-particles. A (ϕ= 30 nm by DLS) , B (ϕ=70 nm by DLS), C (ϕ=120 nm by DLS). The Glass Vials contain the supernatants; the PP plastic centrifuge tubes the wet sedimented particles. Right: wet core-fluorescent silica nano-particles at the end of the washing steps (ϕ=70 nm by DLS).

2.4 References

[1] Kolke, G. *Das komplexehemische Verhalten der Kieselsure*, PhD thesis dissertation, Friedrich-Schiller-Universität, Jena, **1956**

[2] Stöber, W.; Fink , A.; Bohn, E. *J. Colloid Interface Sci.* **1968**, *26*, 62

[3] Herz, E.; Burns, A.; Lee, S.; Sengupta, P.; Bonner, D.; Ow, H.; Liddell, C.; Baird, B.; Wiesner, U. *Proc. SPIE* **2006**, 6096

[4] Han, M.; Gao, X.; Su, J. Z.; Nie, S. *Nat. Biotechnol.* **2001**, *19*, 631

[5] Burns, A.; Ow, H.; Wiesner, U. *Chem. Soc. Rev.* **2006**, *35*, 1028

[6] Xu, H.; Aylott, J. W.; Kopelman, R.; Miller, T. J.; Philbert, M. A. *Anal. Chem.* **2001**, *73*, 4124

[7] Tam, F.; Goodrich, G. P.; Johnson, B. R.; Halas, N. J. *Nano Lett.* **2007**, *7*, 496

[8] Stellacci, F.; Bauer, C. A.; Meyer-Friedrichsen, T.; Wenselleers, W.; Marder, S. R.; Perry J. W. *J. Am. Chem. Soc*. **2002**, *125*, 328

[9] Van Blaaderen, A.; Vrij, A. *Langmuir* **1992**, *8*, 2921

[10] Xu, J.; Sun, L.; Li, J.; Liang, J.; Zhang, H.; Yang, W. *Nanoscale Res. Lett.* **2011**, *6*, 561

[11] Xu, J.; Sun, L.; Li, J.; Liang, J.; Zhang, H.; Yang, W. *Nanoscale Res. Lett.* **2011**, *6*, 561

[12] Nyffenegger, R.; Quellet, C.; Rickla, J. *Colloids Interface Sci. Ser.* **1993**, 159, 150

[13] Matsoukas, T.; Gulari, E. J. *Colloids Interface Sci. Ser.* **1991**, 145, 557

[14] Bogush, G. H.; Zukoski, C. F. *Colloids Interface Sci. Ser.* **1991,** *142*(1), 19

[15] Bailey, J. K.; Mecartney, M. L. *Colloids Surf. A* **1992**,63, 151

[16] Bogush, G. H.; Zukoski, C. F. *Colloids Interface Sci. Ser.* **1991**,*142*(1), 19

[17] Van Helden, A. K. ; Jansen, J. W. ; Vrij, A. *Colloids Interface Sci. Ser.* **1981**, *81*(2), 354

[18] Palmai, M.; Nagy, L. M.; Mihaly, J. *Colloids Interface Sci. Ser.* **2013**, 390, 34

[19] van Bladeeren, A.; Vrij, A. *Langmuir* **1992**, 2921

[20] Herz, E.; Ow, H.; Bonner, D.; Burns, A.; Wiesner, U. J. *Mater. Chem.* **2009**, 19, 6341

Chapter 3: Stable poly (methacrylic acid) brush decorated silica nano-particles by ARGET ATRP for bio-conjugation

3 Introduction: silica nano-particles as a platform for bio-conjugation

The advent of nano-technology and more recently nano-medicine has increased the demand for well-defined nano-particles (NPs) for example in areas such as diagnostics, drug delivery, bio-separation among others. [1-6] Silica nano-particles (Si-NPs) is among the most widely applied class of nano-particles owing to their well-documented synthetic accessibility by the base or acid catalyzed condensation of low molecular weight silicates. This process known as the Stöber synthesis (and variations thereof) allows the synthesis of Si-NPs ranging from 15 to 800 nm [7,8] with good size control and, if desired the incorporation of dyes or active molecules[9]. An increasingly important aspect in the design of nano-particles is their surface functionalization to facilitate interaction with the environment, the conjugation of active (bio)-molecules or simply to enhance their colloidal stability. Very useful in that respect are polymer brushes, i.e. functional polymers attached to the nano-particle surface, due to their high functional group density.[10,11] We are interested in the decoration of Si-NPs with poly(methacrylic acid) (PMAA) or poly(acrylic acid) (PAA) as they can easily be conjugated with bio-molecules by conventional coupling chemistry. [12] Moreover, the hydrophilic nature of these brushes stabilizes the nano-particle suspension in aqueous media thereby preventing particle aggregation and ensuring extended shelf life. [13]

The grafting of polymer chains from the surface of the NP is the most widely used methodology to achieve polymer brush decorated silica nano-particles. Controlled radical polymerization techniques such as atom transfer radical polymerization (ATRP) are particularly useful in that respect as they permit the engineering of polymer brushes of defined length, density, and composition so as to modulate the surface functionality and properties of the NP. [14-20] Although ATRP has been extensively used for the polymer decoration of various surfaces including few examples of PAA and PMAA, it has the drawback of high copper catalyst concentrations. While the catalyst can be removed when micro or macroscopic substrates are used (e.g. silicon wafers), removal of the catalyst from NP is challenging. This drawback can be overcome by activator regeneration by electron transfer (ARGET) ATRP. [21, 22]In ARGET ATRP the amount of copper catalyst is

significantly reduced by a strategy that employs a reducing agent to *in-situ* regenerate the active Cu(I) species. This technique has successfully been employed from surfaces [12, 23-27] but to the best of our knowledge there are only very few reports of ARGET ATRP from Si-NP. In one instance, Wanless published poly(2-(diethylamino)ethyl methacrylate) brushes from 120 nm diameter silica particles by this technique. [28]

Here we report for the first time the synthesis of PMAA decorated Si-NP by surface initiated ARGET ATRP of tert-butyl methacrylate (t-BMA). Comparison of polymers obtained from free sacrificial initiator and surface de-grafted material show good agreement up to 50 % monomer conversion. Subsequent mild deprotection of the poly(t-BMA) yielded hydrophilic PAA decorated Si-NP with high colloidal stability. The feasibility of these nano-particles as a platform for bio-conjugation was shown by the immobilization of Horseradish Peroxidase (HRP).

3.1 Results and Discussion

The synthesis of the brush decorated Si-NP include the surface decoration of the bare nano-particles with an ATRP initiator, the polymerization of t-BMA and a final deprotection step of the poly(t-BMA) to form the PMAA brush. The Si-NPs used in this work have an average diameter of 200 nm (PDI= 0.014) and were obtained by a classical Stöber synthesis from tetraethyl ortho-silicate (TEOS).7 The introduction of the initiator groups to the NP surface was achieved using a novel silane coupling agent employing 'click' chemistry (Scheme 3.1). [29, 30] Using the click approach, an azido-modified silane moiety **VI** was readily 'clicked' on an alkyne-functional bromoester **V** (Scheme 1). The initiator **VII** was obtained as a dark orange oil. The NMR spectra (Figure 3.1) of **VII** confirm the successful synthesis, in particular the singlet **d** at 8.20 ppm in the aromatic region of the ^{1}H-NMR spectrum due to the formation of the 1,2,3-triazolic ring.[31]

This multi-step reaction is easy to perform, produces high yields and is robust so that sufficient amounts of initiator can be synthesized. While only applied for the synthesis of an ATRP initiator functional silane coupling agent, this strategy would allow preparing initiators for a number of similar techniques just by changing the final active initiator group for the desired polymerization.

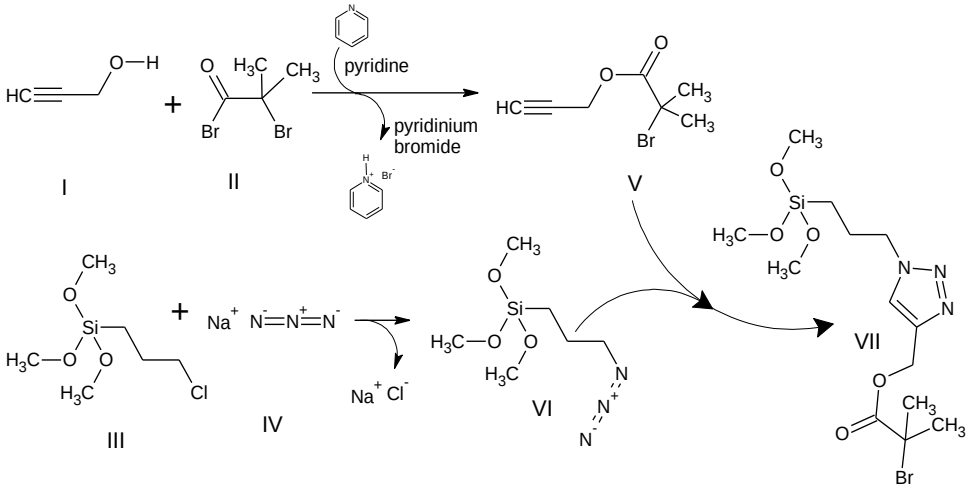

Scheme 3.1: Synthetic route to ATRP initiator silane coupling agent by 'click' chemistry

The decoration of SI-NPs (diameter 200 nm) was carried out in THF in the presence of a defined amount of the initiator-functional coupling agent.

Prior to the reaction the Si-NPs were activated under acidic conditions to maximize the amount of active silanol groups of the surface followed by rigorous drying. Evidence for a successful process was obtained from TGA (Figure 3.2).

From the comparison of the residual masses at 800 °C of the bare Si-NP (87.3 %) and the initiator decorated Si-NP (83.8 %) a total mass increase of 3.5 % upon the reaction was calculated. Considering the surface area of 1 g of 200 nm NPs of 11.34 m^2 (density 2.648 g/cm^3), this corresponds to an initiator concentration of 3.06 mg/m^2.

It is well known that a silica surface has a maximum of 4.5 silanol groups per nm^2, which equals to 7.47 10^{-6} mol of silanols on 1 m^2. [32] This value, multiplied by the initiator molar mass, is a rough estimation of the expected mass of initiator molecules per m^2, in this case 3.07 mg/m^2. This is in perfect agreement with the measured value

and verifies a monolayer decoration of initiator molecules on the NP surface. It has to be noted that careful drying of the NP prior to the decoration is crucial to achieve a monolayer.

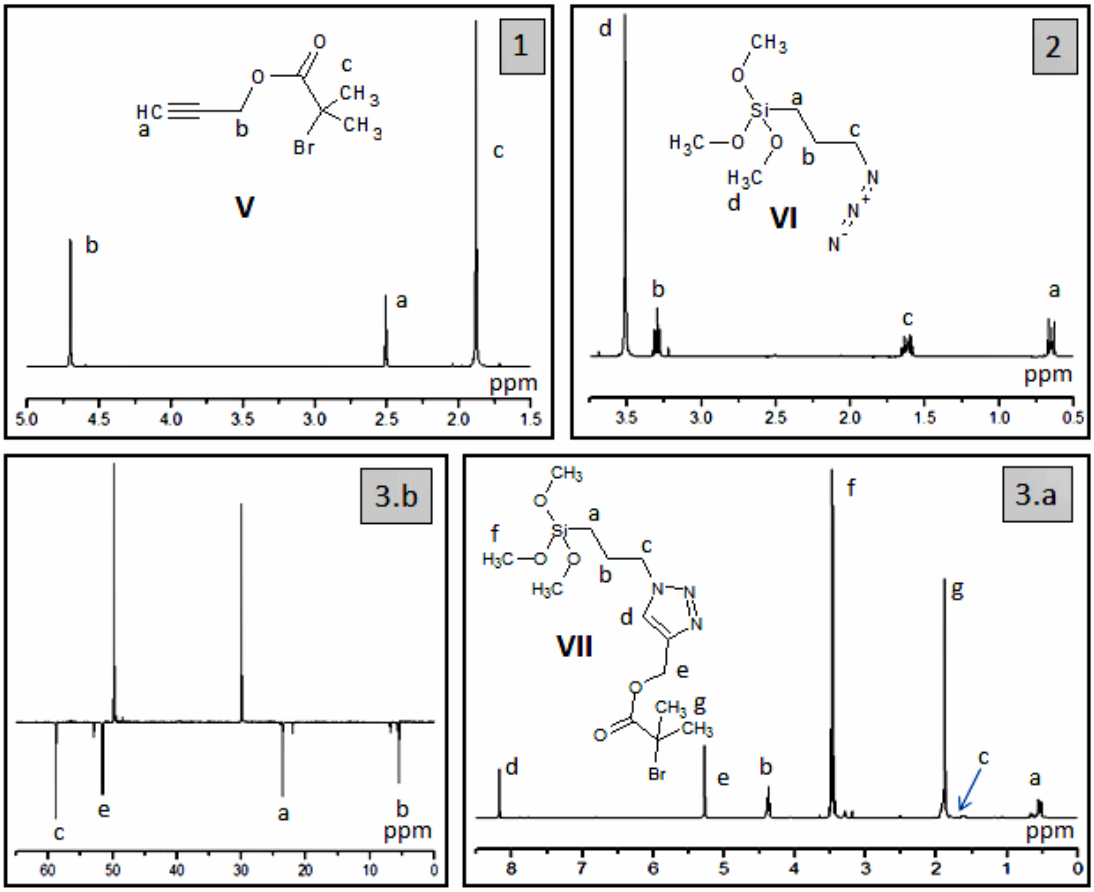

Figure 3.1: $^{1}H/^{13}C$-NMR spectra of the reaction intermediates and the final product in initiator synthesis in Scheme 1. Spectra recorded at 400 MHz in DMSO-d_6. Inset 3.b: distortionless enhancement of polarization transfer (DEPT) ^{13}C-NMR of VII.

ARGET ATRP of tBMA was then performed from the surface initiator decorated Si-NP using $CuCl_2$ and tris-[(2-pyridyl)-methyl]-amine (TPMA) as the catalytic system, and tin(II)-2-ethylhexanoate as the reducing agent. [33] The polymerizations were carried out in the presence of a defined amount of free sacrificial initiator (methyl-2-bromopropionate) to mediate the reaction kinetics as well as the molecular weight of the polymer brushes. **Erreur ! Signet non défini.**

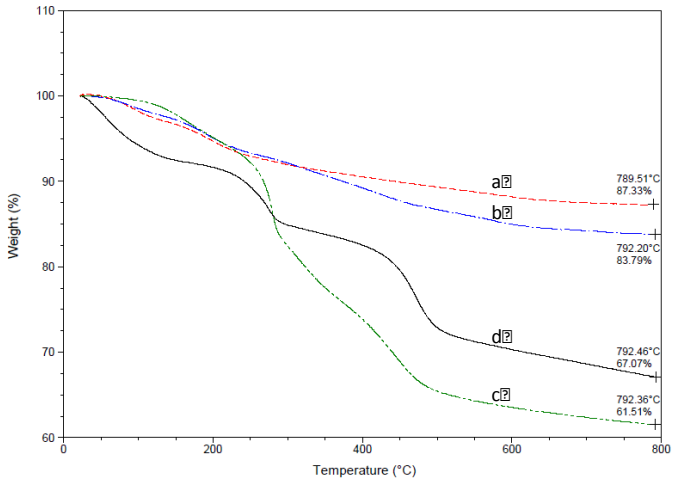

Figure 3.2: Thermo-gravimetric analysis (TGA) results of Si-NP (diameter 200 nm) at various stages of decoration: (a) bare Si-NP, (b) initiator decorated Si-NP, (c) brush poly(t-BMA) decorated Si-NP (polymerization time 180 min.), (d) brush PMAA decorated Si-NP. Note that all samples have been processed under the same conditions (freeze/drying for 5 days at 0.1 mPa at r.t.)

A known amount of dimethylformamide (DMF) was added to the reaction system as an internal NMR standard. The ratio of the ^{1}H-NMR signal intensity from the DMF methyl groups and the ^{1}H-NMR signal intensity of the tert-butyl groups of the *t*-BMA monomer provide a measure of the consumed monomer during the polymerization. Fixed aliquots of the reaction mixtures were withdrawn at time intervals of 30 minutes using N_2 purged syringes.

The collected samples were immediately exposed to air and cooled to stop the polymerization. After centrifugation the supernatant was analyzed by ^{1}H-NMR to determine monomer conversion and by GPC to measure the molecular weight of the free polymer.

The decanted Si NPs were subsequently treated with HF to de-graft the polymer brushes and analyzed by GPC after precipitation in water/methanol to determine molecular weight and polydispersity.

It was found that the polymerisation follows expected first order kinetics (Figure 3.3).

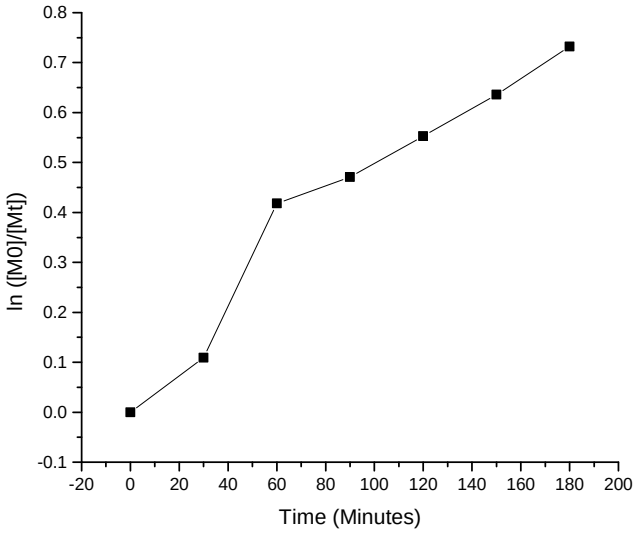

Figure 3.3: The initiator decorated silica nano-particles and the poly (tert-butyl) formation kinetics. Seven samples were collected from the polymerization system at time t=0 s then 6 samples each 30 min.

More interesting is the comparison between the de-grafted and the free PtBMA. In Figure 3.4, the normalized gel permeation chromatograms (GPC) of the de-grafted polymers for the collected samples are presented. A clear shift of the chromatograms from low to high molecular weights can be seen. It is noticeable, however, that with increasing reaction time (monomer conversion) the low molecular weight tail of the traces hardly shifts, which is also manifested in an increasing polydispersity of the samples (Figure 3.5). This was not observed for the free polymer samples. Figure 3.5 shows a comparison of the molecular weights of the de-grafted and free polymer. The very good agreement between both polymer molecular weights up to a monomer conversion of about 55 % suggests that the growth conditions are nearly identical for the free and the surface grafted polymer. Moreover, the increase of M_n with monomer conversion is nearly linear in the 35-55 % monomer conversion range as would be expected for a controlled polymerization. At conversions higher than 55 %, the measured M_n of the surface grafted polymer (156,000 g/mol) is significantly higher than that of the free polymers (5,500 g/mol). The deviation from the linearity for the surface polymerization suggests that the requirements for a controlled

polymerization are not met anymore and uncontrolled growths occurs. As this is not the case for the free polymer, this must be caused by the specific confined surface conditions. It can be speculated that polymer end-groups are not assessable anymore for the catalytic system thus disturbing the delicate balance between dormant and active species resulting in uncontrolled radical polymerization. This is supported by a significant increase in the polydispersity of the de-grafted polymers from 1.3 to 3.5 at 75 % monomer conversion (Figure 3.5). The assumption that free and grafted polymer populations are growing under the same conditions and produce polymers of comparable molecular weight and polydispersity is indeed not generally valid and in practice the comparability is strictly dependent on the specific condition used as the shape of the surface (flat or curved), the presence of confined pores or channels, the density of the grafted chains and the brush thickness can reverse this trend. [34-39]

TGA analysis (Figure 3.2) revealed a total polymeric brush mass of 17.9 % for the PBMA decorated Si-NPs at 75 % monomer conversion. Following the successful grafting of the PBMA brush, the final step was the deprotection of the *t*-butyl groups to yield PMAA decorated Si-NP. Numerous methods have been reported for the deprotection of *t*-butyl esters, although most involve the use of strong acids such as CF_3COOH, HCl, H_2SO_4, TsOH and MsOH or Lewis acids such as $BF_3{\cdot}OEt_2$, TMSI, TMSOTf, $TiCl_4$, $SnCl_4$, $AlCl_3$, $Sn(OTf)_2$, and $ZnBr_2$. [40, 41] However, strong acidic conditions and prolonged reaction times can promote hydrolytic reactions able to de-graft the polymer chains from the Si-NP surface. Alternatively, the deprotection can also be achieved under mild acidic conditions by Montmorillonite K10 clay catalyst or silica gel (low pressure) but this approach would require separating NPs from another solid phase. [42] Alternatively we investigated aqueous phosphoric acid (85 wt. %) based on reports that it is an effective, environmentally benign reagent for the de-protection of *t*-butyl carbamates, *t*-butyl esters, and *t*-butyl ethers. [43, 44]

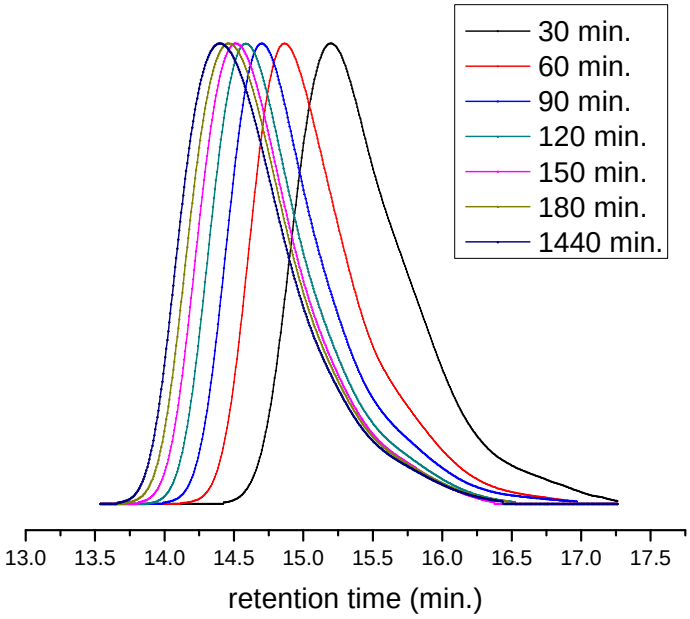

Figure 3.4: GPC chromatograms of the de-grafted polymers (normalized curves) at 30 minutes intervals and final sample after 24 h

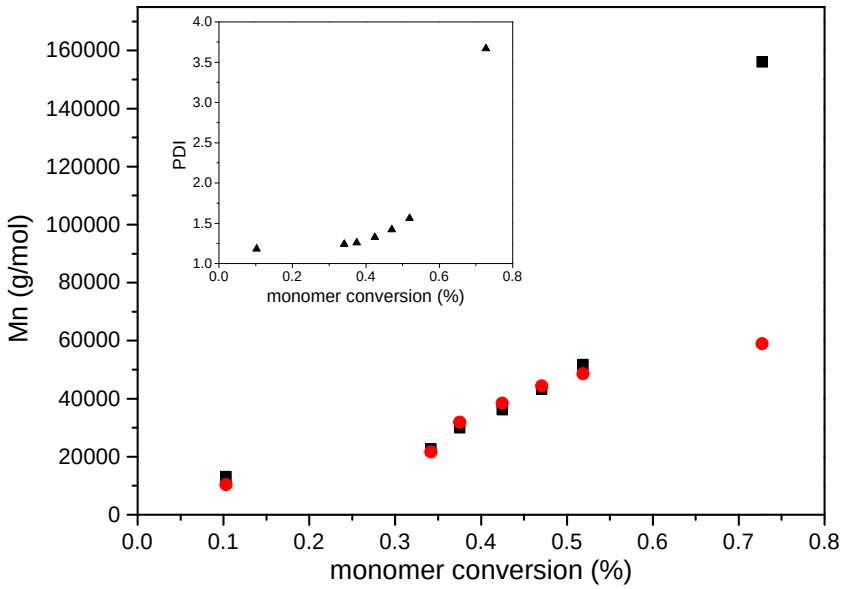

Figure 3.5: Molecular weights (M_n) and polydispersity (PDI, inset, ▲) of de-grafted polymer (■) and free polymer (●) as a function of monomer conversion.

The reaction conditions are mild, high yielding and offer good selectivity in the presence of other acid-sensitive groups such as cyclic carbamates, lactones, ketals, acetate esters. Figure 3.6 shows the attenuated total reflectance IR (ATR-IR) spectra

of PBMA decorated Si-NP before and after treatment with aqueous phosphoric acid. Notably, the peaks characteristic of PBMA (Figure 3.6, A) and PMAA (Figure 3.6, B) can be identified and are in agreement with literature data. [45, 46]

For example, the C=O stretching (**3**) at 1720 cm^{-1} and peaks such as the broad peak at 1470 cm^{-1} (**4**), and the doublet at 1390 cm^{-1} (**5** and **6**) assigned to the *t*-butyl group. After the deprotection step, peak **3** remains unchanged while the methacrylic acid bands appear (**7a**, **7b**, **8** and **9**) and peak **2** disappears.

Further evidence for the hydrophilic character of the de-protected Si-NP is their full dispersability in water as depicted in Figure 3.7. While the hydrophobic PBMA NP cannot be suspended in water, hydrophilic PMAA NP form a stable, homogeneous suspension within 5 seconds of ultra-sonication highlighting the change of hydrophilicity due to the deprotection process.

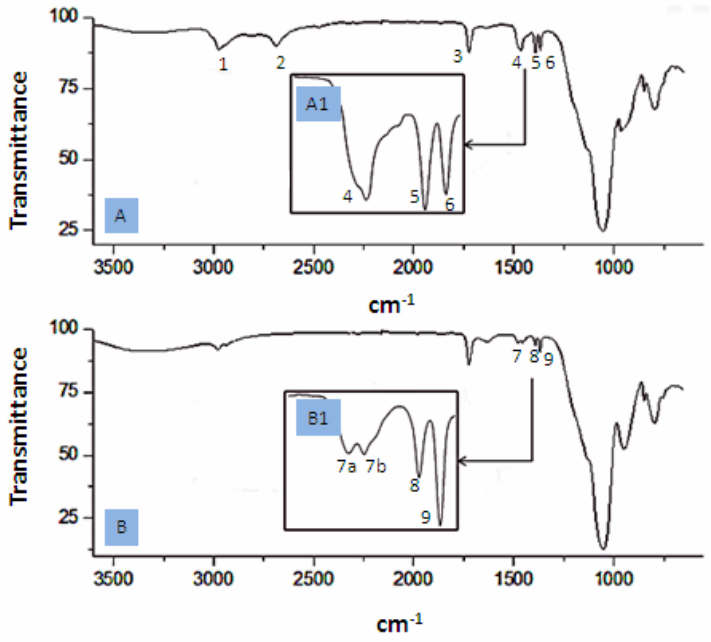

Figure 3.6: ATR-IR spectra of PBMA decorated Si-NP before (A) and after de-protection (B) with aqueous phosphoric acid.

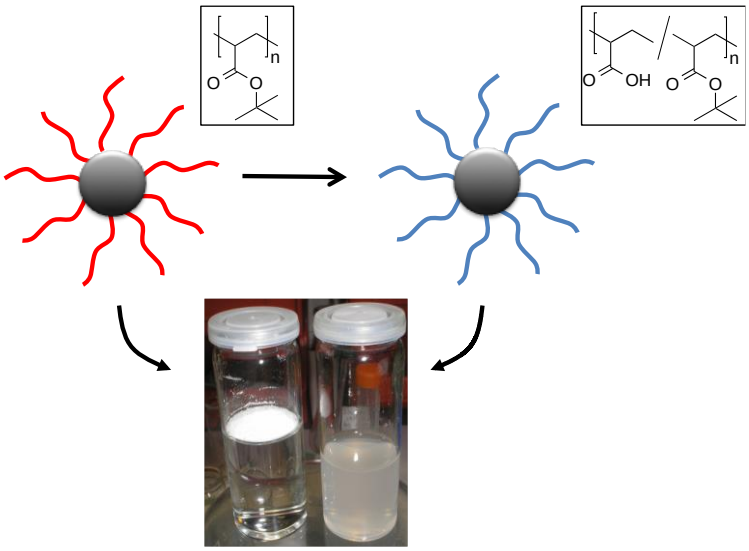

Figure 3.7: Hydrophobic PBMA decorated Si NPs floating on water (left) and hydrophilic PMAA Si NP suspended in water.

The deprotection yield for the PMAA Si-NP obtained at 75% monomer conversion was calculated from TGA analysis (Figure 3.2). A mass loss of 4.4 % compared to the PBMA NP was measured after the deprotection step. Considering a theoretical weight loss of 8.6 % at quantitative deprotection for this specific sample this corresponds to about 50 % deprotection yield after 12 hr of deprotection reaction. It was found that this is indeed the maximal possible de-protection degree as prolonged reaction times result in undesired brush and NP hydrolysis (Figure 3.8).

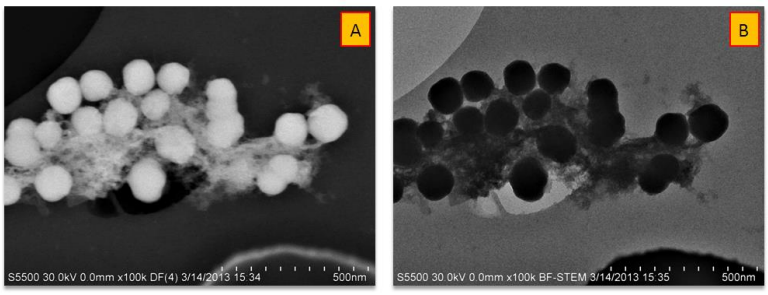

Figure 3.8: brush PBMA Si-NP (200 nm) after a 24 h deprotection. A: Dark Field secondary electron mode. B: Bright Field standard emission. The presence of the degrafted brush enveloping the Si-NP can be seen. Moreover, diameter reduction from 200 nm to 150 nm is evident as well as a less regular shape of the nano-particles compared to the bare Si-NPs due to the hydrolysis of the brush and of a partial silica re-dissolution.

The incomplete deprotection is most likely due to a low accessibility of *t*-BMA groups close to the silica surface. It is here worthwhile to note, that this is not a negative feature as a hydrophobic region close to the nano-particles surface provides a protective barrier against hydrolysis of the polymeric chains. This is highlighted by the fact that treating the Si-NP suspensions at pH range 2-10 had no detectable detrimental effect on the suspension stability or particle quality (Figure 3.9).

Moreover, this diffusion barrier is contributing to the stability of these mono-disperse suspensions in 0.1 M phosphate buffer solution at pH 7.4 (monitored over one year), a pH of interest as the majority of proteins are stable under these conditions, which makes these nano-particles directly suitable for bio-conjugation.

Figure 3.10 depicts Field Emission Scanning Electron Microscopy (FE-SEM) image of Si-NP at different stages of decoration. In particular the brush decorated NP show a distinct core-shell structure (Figure 3.10 D-F). The denser silica core appears as a dark gray (or blue in bright filed mode) and the surrounding corona made of less dense PMAA brush appears as lighter gray or blue. The silica core is perfectly spherical as evident from the sharp border in the micrograph and the brush thickness of the surrounding polymeric corona is highly regular. For the 200 nm NP a brush thickness of 40 nm can be estimated. Generally PBMA brush decorated Si-NP show a higher tendency to melting under a 30 kV electron beam and the corona shadow surrounding the nano-particles in this case has a less sharply defined contour if compared to the de-protected system.

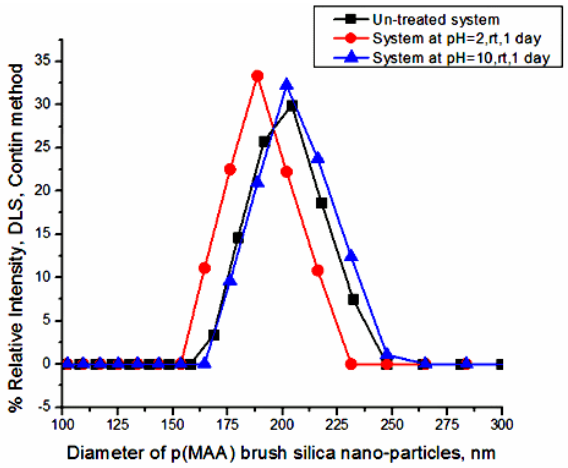

	Average diameter, nm	± Error bar, nm	PDI
Un-treated system	200.8	15.9	0.014
System at pH=2, 1 day, rt	189	14.8	0.009
System at pH=10,1 day, rt	204.1	16.5	0.017

Figure 3.9: Three water suspensions of brush PMAA) Si-NPs (polymerization time 180 min. pertinent to line d in Figure 3.2 (TGA) and to chromatogram at 180 min. in Figure 3.4 (GPC data)) at 5 mg/mL are tested. The un-treated sample was left un-touched. One sample was treated at pH=2 (by HCl) at room temperature during 1 day, then centrifuged and re-suspended in water up to neutrality of the supernatant. The third system had a pH=10.0 (by NaOH) treatment everything left the same. The three systems (at the same 5 mg/mL brush p(MAA) Si-NPS, in the same solvent (Water)) are then analyzed by DLS using the Contin method. The Polydispersity Index (PDI) is the ratio (standard deviation)^2/(weighed diameters average)^2 calculated using the % Relative intensities signals.

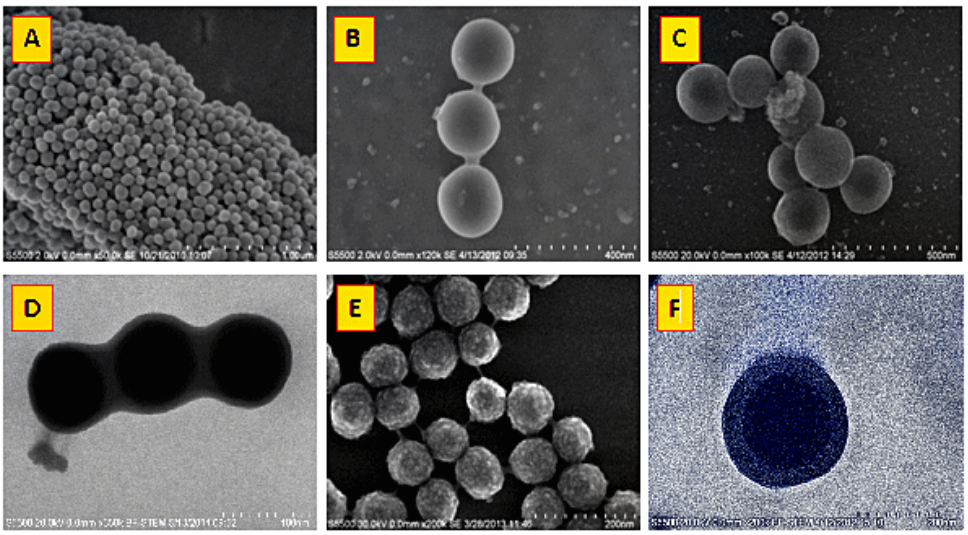

Figure 3.10: FE-SEM images of Si-NP of different size and state of decoration. A and B: bare Si-NP; C: ATRP initiator decorated NP; D: Pt-BMA brush decorated Si-NP; E and F: PMAA brush decorated Si-NP.

Immobilization of bio-molecules, such as proteins, enzymes, or antibodies on solid substrates has great importance in biosensors and biotechnology applications owing to their specific affinity for their targets. [47,48] Due to their robustness and versatility, functional polymer brushes have been utilized extensively for the immobilization of bio-molecules. [12, 47-52] Herein, horseradish Peroxidase (HRP) has been chosen to conceptually investigate the covalent immobilization through carboxylic acid groups of PMAA decorated Si-NP. HRP is a a-helical globular protein with an average diameter of ~ 4.5 nm. [46, 53] It is used extensively in biochemistry applications primarily for its ability to amplify a weak signal and increase detectability of a target molecule.[54] HRP immobilization was performed using common EDC/sulfo-NHS coupling chemistry between amino groups of lysine residue of HRP and carboxyl groups of grafted PMAA at pH 7.4. A series of experiments was carried out systematically varying the weight ratio of HRP to PMAA decorated SI-NPs (diameter 160 nm) from 30, 40, 50, 60 and 70 g HRP solutions (1mg/mL) to 1 mg of NP suspension. The NP were subsequently washed and recovered by centrifugation. The enzymatic activity of the immobilized HRP was monitored using o-phenylene diamine dihydrochloride (OPD) as a chromogenic substrate. Upon reaction with HRP in the presence of hydrogen peroxide the soluble product 2,3-diaminophenazine is formed, which can be quantified UV spectroscopically at ~ 441 nm. Figure 3.11 shows a linear dependence of the UV absorbance peak from the HPR immobilised on the NP. When compared to the UV signal obtained from the free HRP at a concentration that corresponds to the highest concentration used in the immobilisation protocol, a relative activity of 93 % was realised. Slight activity loss could be due to inactive HRP on the surface, non-quantitative immobilisation or slight mosses in the work-up procedure.

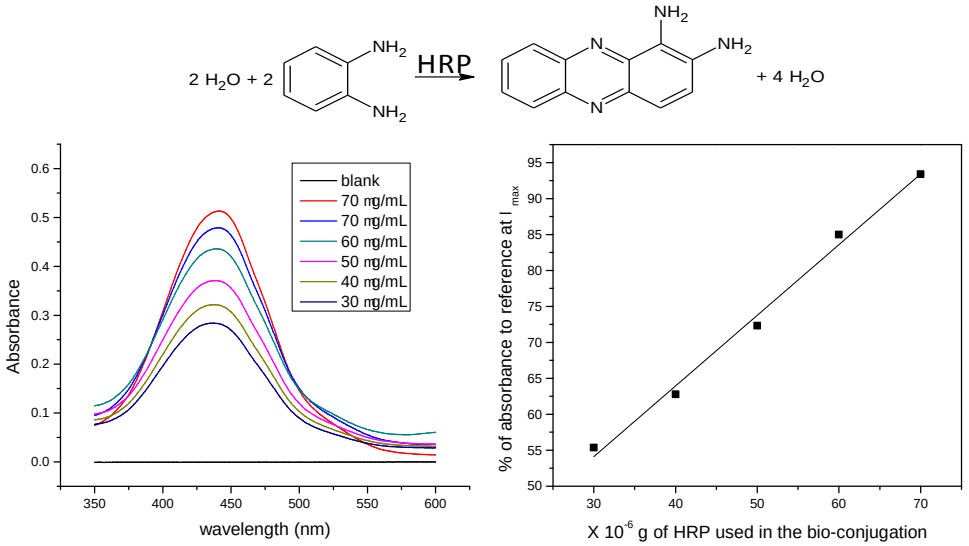

Figure 3.11: Horseradich peroxidase (HRP) catalysed conversion of o-phenylene diamine dihydrochloride (OPD) into 2,3-diaminophenazine and significant UV-Vis absorbance peaks of 2,3-diaminophenazine for reactions catalysed by SI-NP conjugated with HRP at a concentration of 1 mg/mL NP in PBS at pH 7.4. Experiments 1-5 represent NP with decreasing amout of conjugated HRP. The reference sample was recorded with free HRP (70 µg/mL), while the blank contains no HRP.

3.2 Experimental Section

Chemicals: All chemicals were obtained from Sigma Aldrich and used as received unless otherwise noted. Triphenylphosphine and $CuBr_2$ were obtained from Acros. 1-Ethyl-3-[3-dimethylaminopropyl] carbodiimid and *N*-hydroxysulfosuccinimide were obtained from Thermo Fisher. $Cu(PPh_3)_3Br$ was synthesized according to a literature procedure. [55] Peroxidase from horseradish Type VI, essentially salt-free, lyophilized powder, 250-330 units/mg solid (using pyrogallol), *o*-Phenylenediamine tablet (20 mg substrate per tablet), hydrogen peroxide solution (30 wt.% in H_2O), 1M H_2SO_4 were obtained from Sigma Aldrich.

Methods: ^1H and ^{13}C nuclear magnetic resonance (NMR) spectra were recorded at room temperature on a Bruker Avance 400 (400MHz) and a Bruker Avance Ultrashield 600 (600 MHz). $CDCl_3$ was used as a solvent and the signals were referred to the signal of residual protonated solvent signals. Thermo-gravimetric analyses (TGA) were performed on a TGA Q50 from TA Instruments using a temperature ramp from 20° to 800°C at 20°C/min. under nitrogen atmosphere. All samples were carefully dried before measurement (3 days at 0.1 mbar at RT). A Perkin-Elmer Spectrum 100 was used for collecting attenuated total reflectance Fourier transform infrared (ATR-FTIR) spectra in the spectral region of 650–4000 cm^{-1}. The spectra were obtained from 4 scans with a resolution of 2 cm^{-1}. A background measurement was taken before the sample was loaded onto the ATR unit for measurements. To measure melting points a Gallenkamp melting point apparatus has been used. Molecular weights of polymer were characterized by gel permeation chromatography performed on an Agilent 1200 series equipped with two PL Gel 5 micrometer Mixed-C 300 * 7.5 mm^2 columns at 40°C and a differential refractive index (DRI) detector. Tetrahydrofuran (THF) was used as an eluent at a flow rate of 1 mL min^{-1}. Molecular weights were calculated based on poly(methyl methacrylate) standards. TEM images were obtained using a TITAN microscope at Trinity College Dublin CRANN (at an accelerating voltage of 200 kV) for samples deposited on carbon-coated (400 mesh) copper grids. The preparation of samples for transmission

electron microscopy (TEM) analysis involved depositing a drop (15 mL) of the nano-particle suspension in toluene of water onto the grids and allowing the solvent to evaporate prior to imaging. The dynamic light scattering (DLS) experiments of peptide grafted nano-particles in different pH solutions were performed at 25° C on a ZetasizerNano ZS particle analyzer (Malvern Instruments) using a detection angle of 173 degree and a 4 mW He–Ne laser operating at a wavelength of 633 nm. Perkin-Elmer Lambda 900 spectrometer (Foss, Ireland) was used for HRP colorimetric tests.

Prop-2-ynyl 2-bromoisobutyrate (V)[56]**:** A clean round bottom flask (previously dried 1 night in the oven at 140° C) containing 100 mL of anhydrous ether was cooled to 0 °C using an ice/water bath. The solvent was purged 10 minutes with N_2 before the addition of 2-bromoisobutryl bromide (20.0 g, 87 mmol) and pyridine (8.3 g, 105 mmol). After 2-3 min. the suspension turned yellow. The mixture was stirred for 5 min. before the drop wise addition of propargyl alcohol (5.87 g, 105 mmol) dissolved in 50 mL of anhydrous ether over a period of 30 min after which the suspension turned white. The flask was then removed from the ice bath and the reaction was allowed to proceed at room temperature for 24 h. The reaction mixture was then washed with 100 mL of 1 M HCl, 100 mL of 1 M NaOH, and 100 mL of brine, and then dried over anhydrous $MgSO_4$. The solvent was removed by rotary evaporation at 35°C and 0.1 mbar for 1 hour and the alkyne group containing ATRP initiators was obtained as a white solid (yield: 89%). ^{1}H NMR ($CDCl_3$): δ 4.78 (d, 2H, CH_2O), 2.55 (t, 1H, C-CH) and 1.96 (s, 6H, $(CH_3)_2C$).

3-Azidopropyltrimethoxysilane (VI)[57]**:** To a 250 mL round bottom flask, 3-chloropropyltrimethoxysilane **III**, (6 mL, 6.80 g, 32 mmol), sodium azide **IV** (4.2 g, 64 mmol), and N,N-dimethylformamide (DMF) (40 mL) were added. The reaction mixture was stirred at 100° C for 24 h. After cooling to room temperature, the mixture was filtered and the filtrate concentrated under reduced pressure by rotary evaporation at 35°C, 0.1 mbar for 2 hours to yield a yellow liquid as product (yield: 3.1 g, 95%). ^{1}H NMR ($CDCl_3$): δ 3.57 (s, 9H, O-CH_3), 3.27 (dt, J = 2,7 Hz, 2H, N_3-CH_2), 1.71 (m, 2H, CH_2), 0.71 (m, 2H, Si-CH_2).

1-((3-Trimethoxysilyl)propyl))-4-(ylmethyl 2-brono-2-methylpropanate)-1,2,3-triazole (VII): In a round bottom flask 1.2 mol eq. prop-2-ynyl 2-bromoisobutyrate, 1 mol. eq. 3-azidopropyl trimethoxysilane and 0.5 mol % catalyst $Cu(PPh_3)_3Br$ in DMF are stirred for 24 h at room temperature. After centrifugation and removal of the solvent in a rotary evaporator the product was obtained without further purification as a dark orange oil (density measured at RT is 1.45 g/mL) and stored under N_2 at 4°C (yield: 78%). ^{1}H NMR ($CDCl_3$): δ 0.52 (m, 2H, -CH_2-), 1.91 (s, 8H (6+2), $(CH_3)_2C$) and –CH_2-), 3.57 (s, 9H, O-CH_3), 4.32 (m, 2H, -CH_2-), 5.25 (m, 2H, -CH_2-O), 8.20 (s, 1H, triazolic C(5) proton). ^{13}C-NMR (DEPT) δ 5.80 (-CH_2-), 23.70 (-CH_2-), 30.02 (-CH_3), 49.90 (-CH_3), 51.70 (-CH_2-), 59.10 (-CH_2-), 124.35 (C-H) (*13C-NMR DEPT assignments confirmed by Heteronuclear Multiple Bond Correlation (HMQC) NMR 1H-13C correlation spectrum.*).

Synthesis of Si-NP (diameter 200 nm): To prepare a 1 L alcosol batch with Si-NP 200 nm in diameter, 406.5 g of a 7M solution of ammonia in MeOH are weighed and mixed with water (162.4 g) and TEOS (58.35 g). Finally, 247.3 mL of EtOH were added. The system was left overnight at room temperature. Subsequently the particles were recovered by successive centrifugations/decanted re-resuspension cycles in ethanol, acetone and THF.

Decoration of silica nano-particles with ATRP initiator VII: The concentration of NP in the decoration suspension can be up to 1 g per 40 mL of solvents (for nano-particles up to 200 nm or less for smaller diameters). The system must be perfectly homogenous and mono-disperse and for this reason a 2 mL properly diluted aliquot of the system at room temperature should be analyzed by DLS at this stage. The acidic (acetic acid 0.027% V/V) suspension in THF of the bare SI-NP is gently stirred for 2 hours at 35-40°C. Then, 2 % V/V of initiator (diluted in 5 mL of THF) is added drop-wise during 5 minutes under stirring and the system is refluxed under static N_2 flow overnight. As a final step the washed decorated NP are re-suspend in a minimum amount of THF and left overnight under a very gentle flow of N_2 to complete the formation of silanol bonds. The final powder is stored as stock solution in anisole.

Grafting of tert-butyl methacrylate from ATRP initiator decorated silica nano-particles: To a 22.5 mL glass vial (cleaned with acetone and dried by flushing N_2 for 5 minutes) 100 mg initiator decorated Si-NP were added as an anisole stock suspension (5 mL of 1g/mL suspension). Then a stirring bar and 15 mL of tert-butyl methacrylate (92.3 mmol) are charged. Under magnetic stirring, the sacrificial initiator is added (methyl 2-bromopropionate, 32.80 µL, 0.294 mmol). $CuCl_2$ (0.710mg, 0.0053 mmol) and TPMA ligand (6.50 mg, 0.0224 mmol) are then added. The vial is then sealed with a rubber septum and the reducing agent is added under stirring (tin (II) 2-ethylexanoate, 109 µL, 0.337 mmol). The system is left at 60°C for 4.5 hours. The work up is based on six centrifugation steps at 9000 rpm (7890 RCF) for 20 minutes using toluene to wash the decanted particles (in each re-suspension of the decanted particles 5 minutes of ultra-sonication is applied). The last steps are three washings in THF and the re-suspended system in THF is left under a mild steam of N_2 overnight at room temperature after which a brownish powder (118 mg) was recovered.

Reaction kinetics and de-grafting of polymer from Si-NP: In order to define the kinetic of the polymer growth, a know amount of DMF was added as an internal (and not reactive) NMR standard. Aliquots of the reaction mixture were withdrawn at time intervals with of a N_2 purged syringe. The samples were immediately exposed to air and cooled to stop the polymerization. After centrifugation, the supernatant was analyzed by ^{1}H-NMR, while the solid silica nano-particles (properly dried and washed) were treated with HF to de-graft the polymer from the surface. The supernatant is then treated with methanol/water 1/1 V/V to precipitate the polymers and freeze/dried after centrifugation. The resulting powder was analyzed by GPC.

Deprotection of poly(t-butyl methacrylate) grafted Si-NP: In a typical experiment, aqueous phosphoric acid (85 wt%) was added to a suspension of the brush Si-NP in THF typically with 1 mL of solvent per gram of brush and 15 equivalents of aqueous phosphoric acid (85 wt%). The mixture was stirred at room temperature for 12 hours (this time refers to the system obtained at 75 % monomer conversion). For the workup water was added to dilute the reaction mixture, and concentrated sodium hydroxide solution was added to adjust the pH to 7–8. Final centrifugation steps are repeated up to pH neutrality of the supernatant.

Bioconjugation with HRP: A 10 mg/mL brush PMAA silica nano-particle suspension in 0.1 M MES (2-[morpholino] ethanesulfonic acid), 0.5 M NaCl, pH 6.0 buffer was reacted with 1-ethyl-3-[3-dimethylaminopropyl]carbodiimide (2 mM) and *N*-hydroxysulfosuccinimide (5 mM) at room temperature during 15 min. Then, after fast (2 min.) centrifugation the nano-particles were washed with 0.1 M sodium phosphate, 0.15 M NaCl, pH 7.2-7.5 two times. After decanting the liquid, the solid was diluted in 10 mL of 0.1 M sodium phosphate, 0.15 M NaCl, pH 7.2-7.5 and 5 times 1 mL aliquots are centrifuged. These 5 samples of activated silica nano-particles are re-dissolved in 930, 940, 950, 960, 970 µL of sodium phosphate buffer. The entire process should be carried as quickly as possible (here 8 min.) and at room temperature. Then, aliquots of a freshly prepared solution of Peroxidase from horseradish (HRP) in 0.1 M sodium phosphate, 0.15 M NaCl, pH 7.2-7.5 at 1 mg/mL in HRP are transferred in the activated NP suspension. In particular, 5 aliquots of 70, 60, 50, 40 and 30 µL of the HRP solution at 1 mg/mL were added to the 1 mg/mL activated nano-particles suspension to obtain 5 time 1 mL samples with the same concentrations of nano-particles (1 mg) and different amounts of HRP. The bio-conjugation reaction was complete within 2 h at room temperature. The work up was made by centrifugation and two washing/re-suspension steps in PBS buffer (centrifugation cycles at 6860 Relative Centrifugal Force at 8500 rpm for 3 min). The final samples were stored in 0.1 M PBS buffer at pH= 6.0 at 4°C for no more than two weeks, based on the stability of the HRP at concentrations of 1 mg of bio-conjugated nano-particles per mL of buffer. The specific tests here were carried out with 1 day to 2 weeks old bio-conjugated NP with no difference in the final colorimetric test.

Colorimetric test: A buffer solution was prepared with 10.19 g of anhydrous citric acid, 30.90 g of Na_2HPO_4 12 H_2O (or, as an alternative, 14.60 g of Na_2HPO_4) at pH=5 in 1L of ultra pure water (18 MW/cm). A 20 mg tablet of o-phenylene diamine is dissolved in 50 mL of this buffer and left in the dark. Immediately before the colorimetric test, 20 µL of H_2O_2 (30% vol) were added. To each aliquot of bio-conjugate at 1 mg/mL, 0.1 mL of this buffer is added. The system is left in the dark at room temperature during 2 h then 25 µL 1M H_2SO_4 are added to stop the reaction. The system is then measured in a UV spectrophotometer at l_{MAX} ~ 441 nm.

3.3 Conclusions

The synthesis of polymer brush decorated silica nano-particles is demonstrated by ARGET ATRP grafting of poly(t-butyl methacrylate). ATRP initiator decorated silica nano-particles were obtained using a novel trimethylsiloxane derivatised ATRP initiator obtained by click chemistry. Comparison of de-grafted polymers with polymer obtained from a sacrificial initiator demonstrated good agreement up to 55 % monomer conversion. Subsequent mild deprotection of the t-butyl ester groups using phosphoric acid yielded highly colloidal and pH stable hydrophilic nano-particles comprising approximately 50 % methacrylic acid groups. The successful bio-conjugation was achieved by immobilization of Horseradish Peroxidase to the polymer brush decorated nano-particles and und the enzyme activity demonstrated in a conversion of o-phenylene diamine dihydrochloride assay.

In conclusion, we have presented a robust protocol for the synthesis of PBMA polymer brushes on well-defined Si-NP using ARGET ATRP. The mild deprotection with phosphoric acid provided access to PMAA/PBMA copolymer brushes with high colloidal and pH stability. The feasibility for conjugation of active bio-molecules to these particles was demonstrated by immobilization of HRP under retention of high level of catalytic activity.

3.4 References

[1] Jiang, T.; Mo, R.; Bellotti, A.; Zhou, J.; Gu, Z. *Adv. Funct. Mater.* **2014**, *24*, 2295

[2] Hood, J. L.; Jallouck, A. P.; Campbell, N.; Ratner, L.; Wickline, S. A. *Antivir. Ther.* **2013**, 18, 95

[3] Thaxton, C. S.; Elghanian, E.; Thomas, A. D.; Stoeva, S. I.; Lee, J.-S.; Smith, N. D.; Schaeffer, A. J.; Klocker, H.; Horninger, W.; Bartsch, G.; Mirkin, C. A. *Proc. Natl. Acad. Sci. U. S. A.* **2009**, *106*, 18437

[4] Getts, D.R.; Martin, A.J.; McCarthy, D.P.; Terry, R.L.; Hunter, Z.N.; Yap, W.T.; Getts, M.T.; Pleiss, M.; Luo, X.; King, N. J. C.; Shea, L.D.; Miller, S.D.*Nat. Biotechnol.* **2012**, *30*, 1217

[5] Li, Y.; Chen, Y.; Xiang, R.; Ciuparu, D. *Anal. Chem.* **2005**, 77, 1398

[6] Chambers, S. D.; Svec, F.; Frechet, J. M. J. *Anal. Chem.* **2011**, 83, 9478

[7] Stöber, W.; Fink , A.; Bohn, E. *J. Colloid Interface Sci.* **1968**, 26(*1*), 62

[8] Nyffenegger, R.; Quellet, C.; Rickla, J. *Colloids Interface Sci. Ser.* **1993**, 159, 150.

[9]Bin, Z.; Brittain, W. J. *Prog. Polym. Sci.* **2000**, *25*, 677*Nanoscale Res. Lett.* **2011**, *6*, 561

[10] Steve, E.; Osborne, V. L.; Huck, W. T. S. *Chem. Soc. Rev.* **2004***, 33*, 14

[11] Audouin, F.; Larragy, R.; Fox, M.; O'Connor, B.; Heise A. *Biomacromolecules* **2012**, *13*, 3787

[12] Li, Z. F.; Ruckenstein, E. *Nano Lett.* **2004**, *4*, 1463

[13] Chunzhao, L.; Benicewicz, B. C. *Macromolecules* **2005**, 38, 5929

[14] Rajesh, R.; Brittain, W. J. *Macromol. Rapid Commun.* **2008**, *29*, 1104

[15] Bindushree, R.; Ranjan, R.; Brittain, W. J. *Soft Matter* **2006**, *2*, 386

[17] Von Werne, T.; Patten, T. E. *J. Am. Chem. Soc.* **1999**, *121*, 7409

[17] Li, D.; Xia, S.; Bin, Z. *J. Am. Chem. Soc.* **2005**, *127*, 6248

[18] Perruchot, C.; Khan, M. A.; Kamitsi, A.; Armes, S. V.; Von Werne, T.; Patten, T. E. *Langmuir* **2001**, *17*, 4479

[19] Chevigny, C.; Gigmes, D.; Bertin, D.; Jestin, J.; Boué, F. *Soft Matter* **2009**, *5*, 3741

[20] Ke, M.; Gao, H. Matyjaszewski, K. *Macromolecules* **2007**, *40*, 1789

[21]Jakubowski, W.; Matyjaszewski, K. *Angew. Chem. Int. Ed.* **2006**, *45*, 4594.

[22] Matyjaszewski, K.; Dong, H.; Jakubowski, W.; Pietrasik, J.; Kusumo, A. *Langmuir* **2007**, *23*, 4528

[23] Hansson, S.; Ostmark, E.; Carlmark, A.; Malmström, E. *ACS Appl. Mater. Inter.* **2009**, *1*, 2651

[24] Jonsson, M.; Nyström, D.; Nordin, O.; Malmström, E. *Eur. Polym. J.* **2009**, *45*, 2374

[25] Wang, M.; Yuan, J.; Huang, X.; Cai, X.; Li, L.; Shen, J. *Colloids Surf. B* **2013**, *103*, 52

[26] Ma, W.; Otsuka, H.; Takahara, A. *Chem. Commun.* **2011**, *47*, 5813

[27] Cheesman, B. T.; Willott, J. D.; Webber, G. B.; Edmondson, S.; Wanless, E. J. *ACS Macro Lett.*, **2012**, *1*, 1161

[28] Kolb, H. C.; Finn, M. G.; Sharpless, K. B. *Angew. Chem. Int. Ed*. **2001**, 40, 2004

[29] Vijay Kumar Patel, V. K.; Vishwakarma, N. K. ; Mishra, A. K.; Biswas, C. S.; Maiti, P.; Ray, B. *J. Appl. Polym. Sci.* **2013**, 127, 4305

[30] Paoprasert, P.; Spalenka, J. W.; Peterson, D. L.; Ruther, R. E.; Hamers, R. J.; Evans, P. G.; Gopalan, P *J. Mater. Chem.* **2010**, *20*, 2651

[31] Pretsch, C.; Seibl, S. Tables of Spectral Data for Structure determination of Organic Compounds, 2nd Ed., Sringer-Verlag: Berlin Heidelberg New York, **1989**

[32] Zhuravlev, L.T. The surface chemistry of amorphous silica. Zhuravlev model. *Colloids Surf. A* **2000**, *173*, 1

[33] Matyjaszewsky, K.; Dong, H.; Jakubowski, W.; Pietrasic, J,; Kusumo, A. Grafting from Surfaces for "Everyone": ARGET ATRP in the Presence of Air. *Langmuir* **2007,** 23, 4528

[34] Turgman-Cohen, S.; Genzer, J. *J. Am. Chem. Soc.* **2011**, 133, 17567

[35] Gorman, C. B.; Petrie, R. J.; Genzer, J. *Macromolecules* **2008**, *41*, 4856

[36] Koylu, D.; Carter, K. R. *Macromolecules* **2009**, 42, 8655

[37] Devaux, C; Chapela, J. P.; Beyou, E.; Chaumont, Ph. *Eur. Phys. J.* **2002**, *7*, 345

[38]Husseman, M.; Malmstro, E. E.; McNamara, M.; Mate, M.; Mecerreyes, D.; Benoit, D. G.; Hedrick, J. L.; Mansky, P.; Huang, E.; Russell, T. P.; Hawker, C. J. *Macromolecules* **1999**, *32,* 1424

[39]Pasetto, P.; Blas, H.; Audouin, F.; Boissiere, C.; Sanchez, C.; Save, M.; Charleux, B. *Macromolecules* **2009**, *42*, 5983

[40] Bose, D. S.; Kumar, K. K.; Reddy, A. V. N. A New Protocol for Selective Deprotection of *N*-*tert*-Butoxycarbonyl Protective Group (*t*-Boc) with $Sn(OTf)_2$. *Synth. Commun.* **2003**, *33*, 445

[41] Greene, T. W.; Wuts, P. G. M. Protective Groups in Organic Synthesis, 3rd ed., John Wiley & Sons: New York, **1999**

[42] Apelqvist, T.; Wensbo, D. Selective removal of the *N*-BOC protective group using silica gel at low pressure. *Tetrahedron Lett.* **1996**, *37*, 1471

[43] Li, B.; Berliner, M.; Buzon, R.; Chiu, C. K. F.; Colgan, S. T.; Kaneko, T.; Keene, N.; Kissel, W.; Le, T.; Leeman, K. R.; Marquez, B.; Morris, R.; Newell, L.; Wunderwald, S.; Witt, M.; Weaver, J.; Zhang, Z. *J. Org. Chem.* **2006**, *71*, 9045

[44] Li, B.; Bemish, R.; Buzon, R. A.; Chiu, C. K. F.; Colgan, S. T.; Kissel, W.; Le, T.; Leeman, K. R.; Newel, K.; Roth, J. *Tetrahedron Lett.* **2003**, *44*, 8113

[45] Shin, H. S.; Jung, Y. M.; Chang, T.; Ozaki, Y.; Kim, S. B. *Vib. Spectrosc.* **2002**, *29*, 73

[46] Metaxa, A. F.; Efthmiadou, E. K.; Boukos, N.; Kordas, G. *J. Colloids Inter. Sci.* **2012**, *384*, 198

[47] Jiang, H.; Xu, F. J. *Chem. Soc. Rev.* **2013**, *42*, 3394

[48] Goddard, J. M.; Hotchkiss, J. H. *Prog. Polym. Sci.* **2007**, *32*, 698

[49] Ates, Z.; Audouin, F.; Harrington, A.; O'Connor, B.; Heise, A. *Macromol. Biosci.* **2014**, *14*, 1600

[50] Audouin, F.; Fox, M.; Larragy, R.; Clarke, P.; Huang, J.; O'Connor, B.; Heise, A. *Macromolecules* **2012**, *45*, 6127

[51] Barbey, R.; Lavanant, L.; Paripovic, D.; Schuwer, N.; Sugnaux, C.; Tugulu, S.; Klok, H. A. *Chem. Rev.* **2009**, *109*, 5437

[52] Xu, F. J.; Neoh, K. G.; Kang, E. T. *Prog. Polym. Sci.* **2009**, *34*, 719

[53] Erickson, H. P. *Biol. Proced. Online* **2009**, *11*, 32

[54] Barbey, R.; Lavanant, L.; Paripovic, D.; Schuwer, N.; Sugnaux, C.; Tugulu, S.; Klok, H. A. *Chem. Rev.* **2009**, *109*, 5437

[55] Gujadhur, R.; Venkataraman, D.; Kintigh, J. T. *Tetrahedron Lett.* **2001**, 42, 4791

[56] Vijay Kumar Patel, V. K.; Vishwakarma, N. K. ; Mishra, A. K.; Biswas, C. S.; Maiti, P.; Ray, B. *J. Appl. Polym. Sci.* **2013**, 127, 4305

[57] Paoprasert, P.; Spalenka, J. W.; Peterson, D. L.; Ruther, R. E.; Hamers, R. J.; Evans, P. G.; Gopalan, P. *J. Mater. Chem.* **2010**, *20*, 2651

Chapter 4: Manufacture of a porous monolith in an inexpensive polypropylene housing

4 Features of porous polymeric glycidyl methacrylate-*co*-ethylene dimethacrylate p (GMA-co-EDMA) monolith

Polymeric porous monoliths (PPM) were prepared for the first time in the early 1990's and used as stationary phases in liquid chromatography.[1] These polymeric solid phases were prepared using a number of monomers such as methacrylates, acrylates, styrene, acrylamides or cyclic monomers. These systems were typically formed casting a blend of monomers, cross-linking monomer, porogens and a free radical initiator inside glass capillaries. [1]

The poly(glycidyl methacrylate-*co*-ethylene dimethacrylate) (poly(EDMA-*co*-GMA)) monolith specifically discussed in this work features the presence of the GMA monomer bearing an epoxy ring, which can be reacted with a range of nucleophiles.[2,3] Applying this chemistry, diol functional groups could be formed on the surface of the monolith as a result of the epoxy group ring opening catalyzed by sulfuric acid. Similarly, amine based functionalities can be obtained by simple post-modification steps following the ring opening reaction with a base such as ethylenediamine or diethylamine.[4] Svec was the first to incorporate GMA into a porous polymeric monolith.[5] The pioneering work in the preparation of polymeric monolithic columns was performed by Hjerten[6] and later by Frechet and Svec, who published studies on *in-situ* co-polymerization of GMA and ethylene dimethacrylate.[7]

The type and the concentration of the cross-linking agent, the porogens, the thermal radical initiator along with the temperature and the times involved in the casting step are important parameters impacting the final composition of the polymer monolith. More cross-linking affects the final morphology with the resulting macro-porous structure consisting of smaller globules with smaller voids and relatively large surface areas.[8] The porogens, as the term suggest, have the function to promote and control the pore formation. Seidl[9], Guyot[10], Kunin[11] pioneered the studies on the mechanisms ruling the pore formation. In this short introduction it is important to note that the more monomer-incompatible the porogenic solvent is, the larger the

pore size of the polymer will be.[12] Thus, the porogens impact the final morphology of the monolith.

There is a fine balance between obtaining a large number of small pores (micro/meso-pores) and larger pores (macro-pores). The small pores significantly increase the overall surface area of the monoliths, and even though the macro-pores do not contribute significantly to the overall surface area, they are essential in providing flow through space, which allow the mobile phase to flow at a reasonable pressure. Both are therefore important to obtain a monolithic column that provides good separation efficiency and a low resistance to mobile phase flow.[13] There is a range of porogens that can be used as part of the EDMA/GMA co-polymerization mixture: 1-propanol, 1,4-butandiol, cyclohexanol, 1-decanol, dodecanol, and dimethylsulfoxide are commonly used. These can be used individually or as a binary or ternary mixture. Viklund reported the preparation and characterization of monolithic stationary phases and reported the effect of varying the relative percentage of porogens/monomers in a co-polymerization mixture.[14] The average pore size can be controlled by at least an order of magnitude by controlling the porogens/monomers ratio. Similarly, raising polymerization temperature results in a decrease of the pore size diameter due a faster rate of initiator decomposition with consequently larger number of precipitating globules in the mixture. [15,16] The free radical initiator half-life is linked to the final porosity of the monolith as well. The impact on the porosity is the same as described for temperature changes, i.e. the substitution of azobisisobutyronitrile (AIBN) by benzoyl peroxide causes the formation of a monolith with higher pore diameters due to a slower decomposition rate in the case of benzoyl peroxide.

Once the monolith blend recipe is defined, another important aspect of a SPE device must be considered, i.e. an anchoring system that assures the phases continuity between the housing and the monolith. Typically, the anchoring system is made by grafting an EDMA based network of oligomers on the inner housing walls. Once the housing is modified, the monolith blend is transferred inside the tubing under oxygen free conditions and the casting process is performed.

The current poly(EDMA-co-GMA) monolith related literature is typically focused on expensive computer assisted techniques such as digital micro-fluidics devices[17], digital micro-fluidic platform[18], solid-phase micro-extraction[19], micro-scale analysis[20], micro-extraction packed syringe for mass spectrometry[21] directly describing the analytical performances of the separation process. Whilst there is a large body of literature on SPE devices, most of those focus on separation performance while materials and detailed manufacturing aspects are receiving less attention. This approach impacts the extent of production details as well as the effective monitoring of each single manufacturing step involved. On that matter, sometimes, the geometry of the housing itself is a problem. Indeed, in the case of micro-capillary housing having a fraction of millimeter diameter, the use of electron microscopy and IR techniques is – if possible - time consuming as during the preparation of the sample the housing, the monolith and the fragile anchoring system tend to break and detach easily. In other cases, the effectiveness of the EDMA-co-GMA chemical modification can only be monitored indirectly using the scanning capacitively coupled contactless conductivity techniques.[22] In the majority of cases, the extraction performances are used to judge the chemical-physical processes involved in the cartridge manufacture. This approach works well only if the whole process is effective but does not offer any explanation in the case of failures. In particular, it would not be possible to derive whether the properly manufactured device is not working *per se* or if the data is not as expected due un-monitored problems in the cartridge manufacture. Typically, problems originate from a non-uniform anchoring system across the monolith length or from non-effective and inhomogeneous chemical modifications of the porous polymeric support. For these reasons, in this chapter, the manufacturing steps of a new readily produced SPEs cartridges made of a polypropylene (PP) housing and a poly (EDMA) anchored EDMA-co-GMA monolith are detailed. Inexpensive materials are used and each manufacture step is monitored in detail. This approach has a number of intriguing features. First of all, the device is inexpensive, so it is possible to perform a high number of tests and then, once a robust protocol is defined on the basis of analytical evidences the manufacture parameters can be directly transferred to automated devices using the same materials. Secondarily, it is well known that the poly (EDMA-co-GMA) porous monolith surface can be chemically modified at the

GMA epoxy ring to target a specific property (e.g. to aim at a hydrophobic/hydrophilic material or to impose permanent electrostatic charges on the monolith surface).[23] Inherently, the SPE device in this study allows monitoring reaction yields and the surface chemical uniformity during these surface-modifying reactions: Indeed, this possibility is explored in the chapter 5.

4.1 Results and Discussion

The SPE device built in this work is the product of a three-step process featuring the use of inexpensive polypropylene (PP) tubing as housing material (the Cristal Bic® pen, mass-produced and sold by Société Bic of Clichy, Hauts-de-Seine, France).[24] In particular, the BIC pen ink-cartridge tubing (made in PP, as per manufacturer brochure[25]) is used as a handy housing for this extraction tool (see Figure 4.1, ink-tubing B). The device manufacture scheme is presented at a glance in Figure 4.2: after the pre-treatments on the tubing (see products I and II), a three-step process is performed. The just cutted PP tubing (see product I in Figure 4.2) is left standing overnight to let the ink flow out by gravity. The tubing is then washed with acetone and ethanol and dryed in the oven at 40°C for 1 hour (see product II in Figure 4.2). The SPE tool housing is now assembled: The PP tubing ends are equipped with plastic luer locks made from blade cut disposable steel needles (see Figure 4.12 in the experimental part). The luer lock polypropylene tubing connection is strong enough to assure watertight conditions if the plastic connetors are properly cut (see Inset A, in Figure 4.12 in the experimental part). Moreover, the luer lock-polypropylene tubing geometry assures the minimum dead volume during the SPE process.

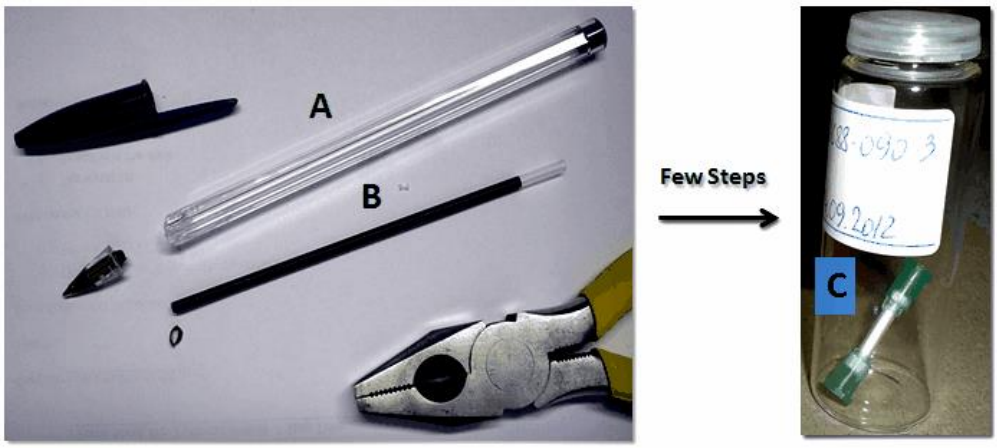

Figure 4.1: Polypropylene ink cartridge (see B) used for the manufacture of an SPE device and final product (see Inset C). The PP ink cartridge (B) is removed from the polystyrene hexagonal barrel (A) of a Bic® pen and processed to form the final monolith-filled cartridge. The final cartridge can be as long as 90 mm and it has an inner diameter of 2 mm.

To prevent the effect of possible heat deformations, the hub-tubing junctions can be protected with teflon seal tape (see Inset C, Figure 4.12, experimental part).

The presence of these two luer lock hubs, directly pluggable onto syringes tips, allows oxygen free UV irradiation curing and thermal treatment to mold the monolith (see steps 1, 2 and 3 in Figure 4.2) as well as the combined use of these home-made cartridges on syringe pumps during nano-particles decorations/SP chemical modifications or extractions (see chapter 5).

This cartridge has an inner volume of 3.14 mm^3/mm and, in the 3-6 cm length range, it can feature a solid phase bed length/diameter ratio in the range of 15-30 and more. In principle longer cartridges can be manufactured up to 90 mm.

In the step 1 of the process under discussion (see Figure 4.2), the cartridge is filled with a de-oxygenated solution of benzophenone in methanol. The sealed system is then irradiated in a UV curing station where a speed regulated horizontal belt expose the cartridge to the emissions of a UV mercury lamp for a time determined by the selected belt speed (see Figure 4.13 in the experimental section for details). A similar procedure follows with the EDMA monomer solution in methanol (see Figure 4.2, step 2). Normally the time between the step 1 and the step 2 is kept to no longer than

24 hours (the BP-PP surface is chemically stable for almost 3 weeks in dark conditions).[35]

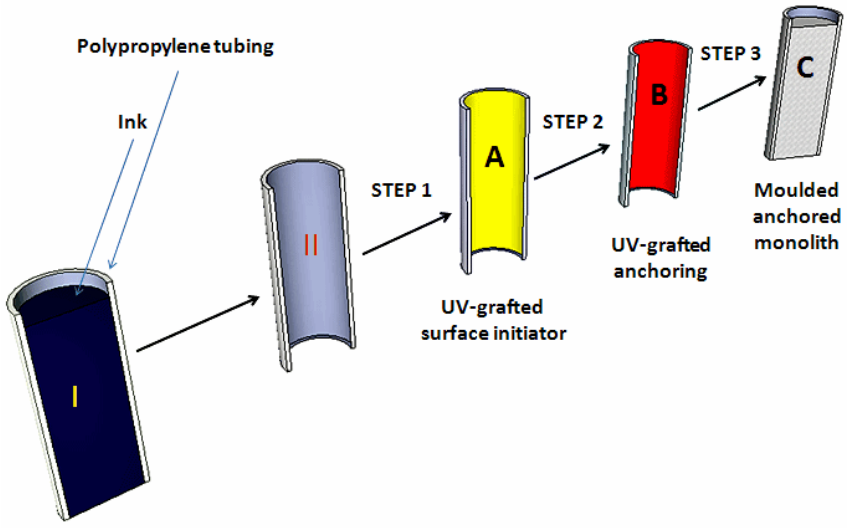

Figure 4.2: Processing of an ink cartridge into an SPE device. The ink cartridge (I) is cleaned (II). Subsequently, a three-step process is performed to build an inner tubing surface anchoring system (steps A, B) and a final molding step completes the manufacture process. Step A in yellow, is the benzophenone UV grafting step. Step B in red, is the EDMA UV photo-grafting process to build the anchoring system. The Step C in gray is the polymeric porous EDMA-co-GMA monolith synthesis by thermally initiated free radical polymerization. The system C is an EDMA-anchored EDMA-co-GMA porous polymeric monolith.

Typically, these steps are performed on a set of several 90 mm PP cartridges (see Figure 4.13 in the experimental part) and then, the surface treated tubing can be cut to the desired length and the step 3 can be performed. Steps 1 and 2 are crucial to assure the homogeneous anchoring system and avoid a poor separation due the presence of preferential macroscopic channels in the extraction tool: Indeed, this three-step process is aimed at the formation of a continuum made of the external PP housing and the to-be-formed inner monolith.

The grafting of acrylic oligomers onto the inner PP surface of the SPE cartridge is challenging because, as all polyolefins, PP surfaces are hydrophobic and chemically inert under ordinary conditions. For these reasons, the PP surface requires chemical or physical treatment to tailor its properties.[26-29] Chemical modification of the interfacial polymer chains with polar groups such as hydroxyl, carbonyl, and

carbonylic acid[30], by flame treatment[31], plasma treatment[32,33], low-pressure glow discharges[34] has been reported. However, all these methods are expensive and not routinely performed in research laboratories. The use of UV radiation and photo-initiators offers an excellent low cost alternative because of its simplicity and cleanness and for this reason, this is the approach used in this work. The rationale for the step 1 (see Figure 4.2) relies in the photochemistry of the benzophenone (BP). Photo-chemically produced triplet states of BP carbonyl group can abstract hydrogen atoms from almost all polymers, thus generating the fast recombining semi-pinacolic radicals and surface radicals (see Figure 4.3). [35,36] The presence of radical species implies the use of oxygen free solutions and treatments. The inhibition effect of oxygen in the grafting reaction of BP has been observed.[37] The minimum concentration required to obtain complete surface coverage of the PP tube is approximately 0.002 wt/wt % of BP in methanol, i.e. the concentration conditions used in this work (5% wt/wt in methanol) assure a total surface coverage. [35] This concentration has been experimentally determined in previous papers as a compromise of lower values (implying longer UV treatments times) and higher values (implying a fast decrease in the UV radiation intensities during the UV radiation passage through the solution.[35]

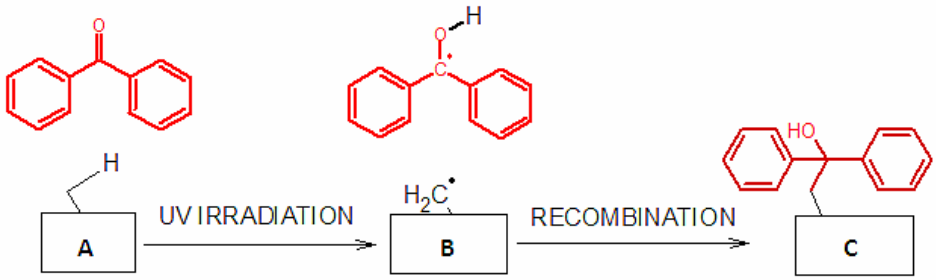

Figure 4.3: The benzophenone photo-grafting sequence. B: semi-pinacolic radical and surface radicals. C: recombination molecule termed "surface initiator" because it can re-generate radicals by exposure to UV light. Note: A, B and C are all part of a one-pot radical-mediated reaction.

Step 2 (see Figure 4.2 and Figure 4.4) is performed using EDMA solutions in methanol. The step 1 formed semi-pinacolic surface grafted molecule and then, the step 2 can re-generate surface radicals and radicals in solution under oxygen free UV light irradiation. The surface radicals promote a free radical polymerization of the EDMA

diacrylate in solution and on the inner PP tubing surface. This process results in an oligomeric cross-linked network chemically linked to the inner PP tubing cartridge surface (see Figure 4.4).

Steps 1-2 need to be performed sequentially as a UV irradiation process with BP and EDMA present at the same time would promote the formation of BP-EDMA cross-products. Indeed, this problem is reduced by the two-step process adopted in this work as the semi-pinacolic radicals (see B in Figure 4.2) have a very short lifetime and preferentially recombine or terminate growing chains if the two processes are sequential. [37] This just formed cross-linked surface polymer will act an intermediate layer during the generation of the final monolith (see step 3 in Figure 4.2) and will ensure a uniform chemical adhesion of the EDMA-co-GMA monolith to the PP surface. In this way, the adhesion between the cast monolith and its housing is assured. This is the main pre-requisite to eliminate housing-monolith detachment and the consequent formation of undesired preferential analyte solution flow in the PP housing-monolith regions, which would negatively impact the performance of the SPE device.

Attenuated total reflectance infrared spectroscopy (ATR-IR) is based on the interaction of an evanescent field penetrating the sample surface typically between 0.5 and 2 µm.[38] For this reason, this technique is particularly suitable to analyze the success of the surface treatments of step 1 and step 2 (see Figure 4.2). In particular, it is possible to monitor the impact of UV treatments for different UV irradiation times for steps 1 and 2 (see Figure 4.2).

For each experiment, after the surface treatment and surface washing/drying at room temperature with N_2, the PP tubing is longitudinally blade cut and flattened (5000 kg/cm^2 during 5 min). In this way, a flat sample is formed with two different faces: one is the tubing inner surface (directly exposed to the BP/EDMA solutions) and the outer surface.

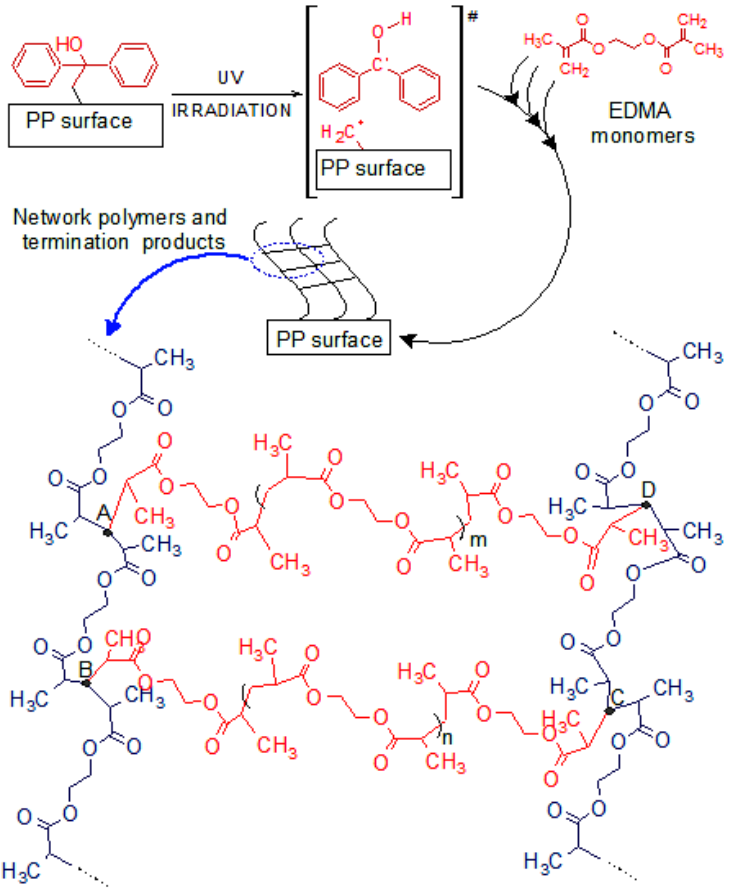

Figure 4.4: UV surface grafted BP, under UV irradiation, re-generates surface radicals and EDMA monomers in solution react in a free radical polymerization process to form a randomly three dimensional polymer network chemically bond to the PP surface. In this figure, 4 knots ABCD in a generic point of the polymeric network are exemplified. Length of the lateral (in red, see m and n numbers) and longitudinal (in blue) lines are statistically distributed due the nature of the radical process.

In the Inset A of Figure 4.5, four ATR-IR spectra are presented. Each spectrum is the averaged accumulation of 1024 scans on the same sample.

Repetition of the analysis on different tubing sections from different batches gave the same results. The black, blue, orange and red lines are relative to four identical inner PP surfaces exposed to the UV radiation for 5, 10, 15 and 20 minutes respectively, while the green line is the ATR-IR spectrum of an untreated PP surface exhibiting the same IR spectrum as the external PP surface irrespective of the UV exposure. The peak a 703 cm^{-1} is due to the presence of the chemically anchored semi-pinacolic photo-initiator [62], i.e. the lower the transmittance value, the higher the density of BP per nm^2. In the Inset B of the Figure 4.7, the transmittance minima

of the ATR-IR spectra peak at 703 cm^{-1} are plotted against time after subtraction of the signal for the untreated sample.

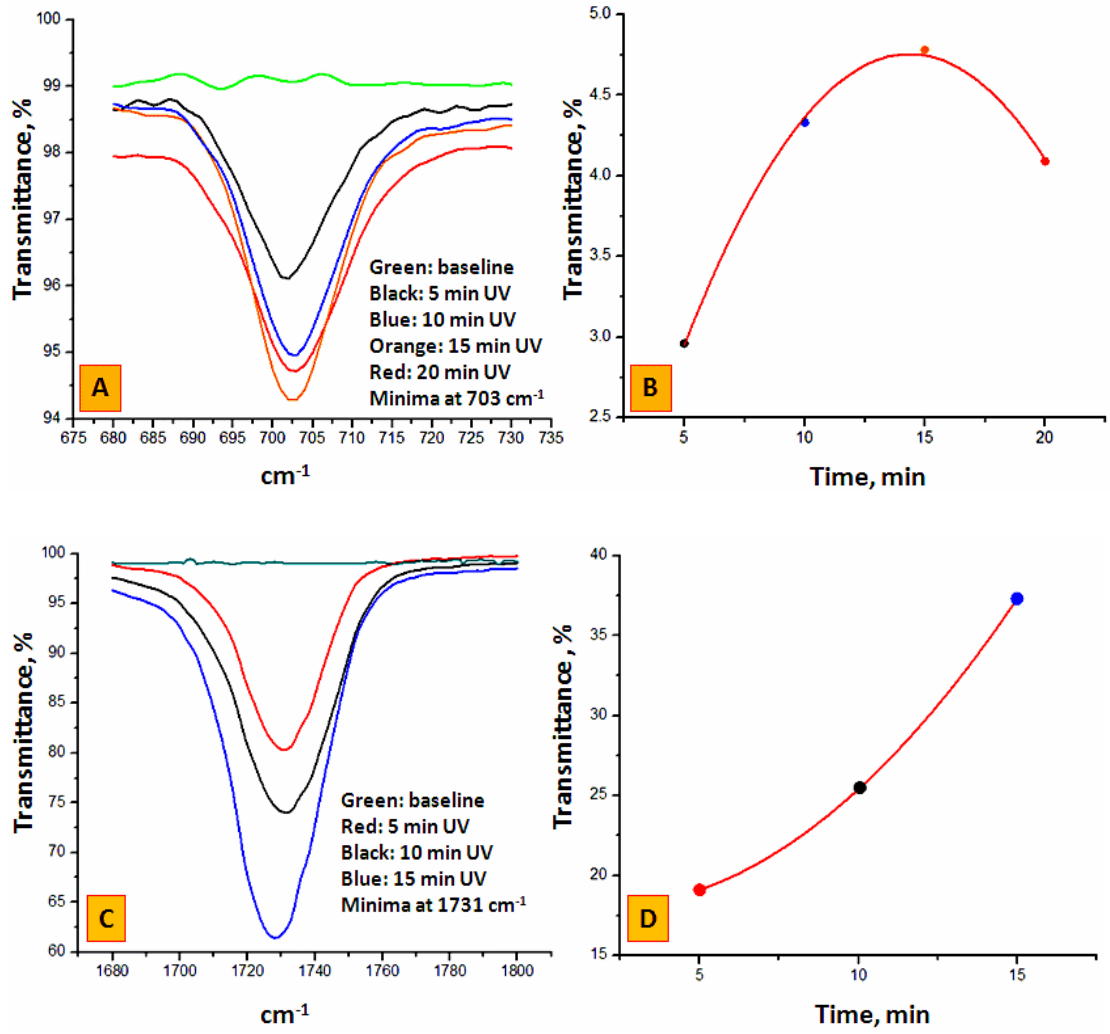

Figure 4.5: Inset A: ATR-IR spectra of the inner PP housing surface sections form the Crystal BIC pen after UV light surface exposure at various times (see Step 1, Figure 4.2, BP 5% wt/wt in methanol); green line: inner PP-surface before UV irradiation. Inset B: Transmittance minima from Inset A (colored dots) at 702 cm^{-1} as a function of UV irradiation time after baseline subtraction (Inset A, green line). The red line in the Inset B is a polynomial best fit curve. Inset C: ATR-IR spectra of the inner PP surface after UV light surface exposure (see Step 2, Figure 4.2, EDMA 5% wt/wt in methanol); green line: Inner PP-surface after 15 min UV treatment (BP 5% wt/wt in methanol). Inset D: Transmittance minima from Inset C (colored dots) at 1731 cm^{-1} as a function of UV irradiation time after baseline subtraction (Inset C, green line). The red line is a polynomial best fit curve. The polynomial best fit $y=A+B*time+ C*time^2$ is defined by the following coefficients: for the step 1, A=0.505, B= 0.5918 min^{-1}, C=-0.0206 min^{-2}; adj. R^2= 0.996; for the step 2, A=18.41, B=- 0.423 min^{-1}, C=0.1122 min^{-2}. The polynomial best fit curve derives from the Polyfit routine in Origin 8.5®. The signal at 702 cm^{-1} is due to the chemically grafted BP while the signal at 1731 cm^{-1} is due to carboxylic groups in the EDMA anchored oligomeric network.

The fact that the number of accessible surface hydrogens is progressively diminishing with time would suggest that a saturation plateau would be reached with increasing UV exposure time. The first three experimental points (5, 10 and 15 min. UV exposition time) in the Inset B, could be part of this model (the increase of surface decoration decrease with time) but the experimental point at 20 min. shows an inversion trend probably due to an increasing oxygen concentration. Indeed, possible mechanical deformations, under this simple experimental set-up, of the tube or thermal swelling during the UV treatment and the formation of leaks could cause oxygen to enter the tube. Nevertheless, during the 15 min. of UV irradiation the device is properly irradiated and sealed under the specific conditions used but irradiation for longer periods of time are not beneficial.

Insets C and D in Figure 4.5, are pertinent to the step 2 in Figure 4.2 and show results presented in the same way. In particular, in the Inset C there are three spectra relative to the inner EDMA treated surface at 5, 10 and 15 min UV exposure time. All experiments were performed on samples with the same step 1 BP treatment (15 min UV irradiation time). The band at 1731 cm^{-1} represents the carbonyl due to the grafted EDMA derived network. Analysis of the IR data shows an increase of EDMA decoration with irradiation time (within the limits of a 15 min exposure) due to the formation of a three-dimensional polymer network.

Additional proof of the anchoring system uniformity was obtained from electron microscopy. In Figures 4.6-7, the morphology of this anchoring layer is presented. Figure 4.6 shows the systems at the macroscopic scale at the end of step 1 (see Figure 4.6, Inset 1) and step 2 (see Figure 4.6, Inset 2) and a SEM micrograph at 2 mm scale (see Figure 4.6, Inset 3).

Step 1 does not change the physical appearance of the PP tubing inner wall. Step 2 impacts the physical appearance at the inner surface level. Indeed, after the 5 % EDMA wt/wt in methanol solution was drained, a dense white skin is left bonded to the inner surface. The residual white solution is opaque with macroscopic granules in suspension resulting from unbound polymer formed by the free radical polymerization.

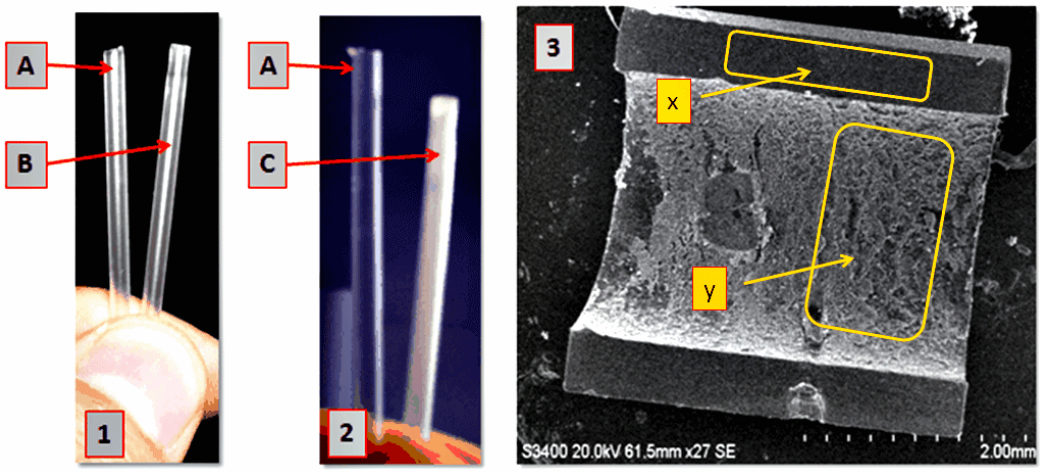

Figure 4.6: Inset 1: the just cleaned PP tubing (A) (see II, Figure 4.4) and the BP treated PP tubing (B) (see A, Figure 4.4) after the washing/drying step. Inset 2: the just cleaned BP treated PP tubing (B) and the EDMA treated PP tubing (C) after the washing/drying step. The inner surface of C shows a visible white layer. Inset 3: SEM micrograph of a longitudinal section of the C tubing in the Inset 2 (scale 2 mm). The anchoring system covers the inner wall of the PP tubing. In the SEM micrograph it is interesting to note the contrast between the smooth untreated PP surface (the dark blade cut areas, see zone marked as "x") and the corrugated network polymer layer chemisorbed on the PP inner wall (clearer central zone, see zone marked as "y").

In Figure 4.7, the same system as shown in Figure 4.6 is examined at higher magnification. The presence of a highly corrugated surface is evident at 400 nm scale (see Figure 4.7, Inset A).

The Insets B, C and D in Figure 4.7 confirm the presence of a ~ 30 nm globular shaped EDMA network polymer intimately bonded to the UV BP treated inner PP surface.

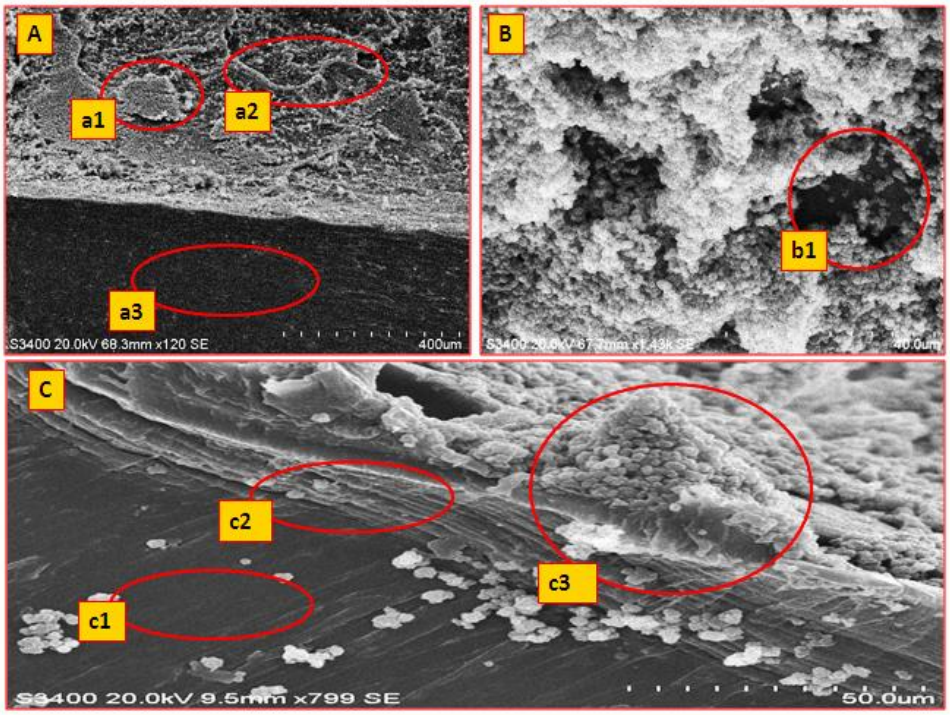

Figure 4.7: Inset A: the same sample in Figure 4.8 (see Inset 3) at a 400 nm scale. The a3 dark zone is the PP inner wall while the a1, a2 zones show the presence of plaques (a1) and corrugated micro-structures. Inset B: the Inset A at 40 nm scale. The nano-globular structure of the EDMA anchoring system is evident. The b1 zone shows the presence of the naked nano-zones (the dark PP wall behind the anchoring system). Inset C: Image of the same Inset B specimen at the PP tubing cutting zone at 50 nm scale. The c1 zone shows the not treated PP fibers and theirs longitudinal arrangement: This is congenital (deriving from the extrusion process used to manufacture the PP tubing). The c2 zone is a ~ 15 nm thick area made of vertical lamellae. The c3 zone shows a perfectly inner surface anchored cluster of network EDMA polymer.

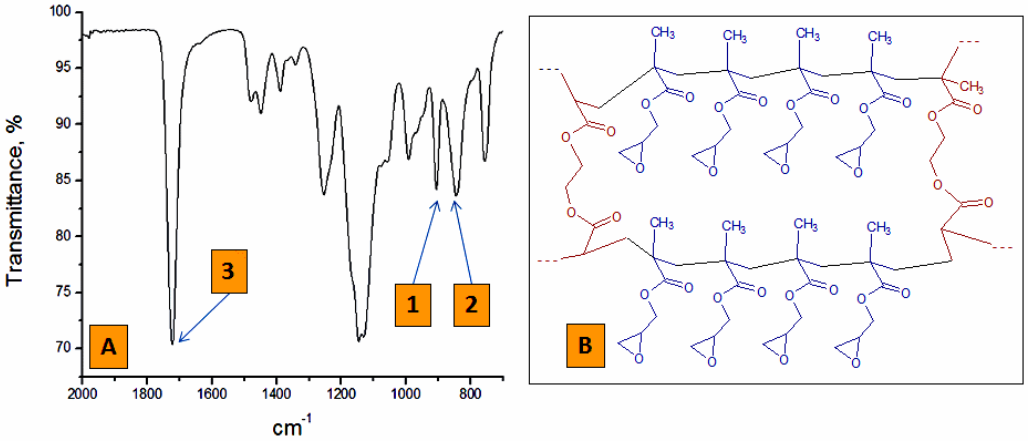

Figure 4.8: Inset A: IR spectrum of the poly (EMDA-co-GMA) monolith (see C, Figure 4.4). The presence of the two bands (see peaks 1 and 2 at 900 and 850 cm^{-1}) confirms for the epoxy ring while the peak 3 at 1735 cm^{-1} derives from the carbonyl stretching. Inset B: The chemical structure of the EDMA-co-GMA polymeric monolith. In red the polymerized cross-linking monomer EDMA and in blue the functional polymerized monomer GMA.

The formation by thermally induced free radical polymerization of the monolith directly in the PP tube is the aim of step 3 in Figure 4.2: The PP tube is filled with a solution containing a free radical initiator, the monomers (EDMA and GMA) and the porogens solvents under N_2 atmosphere.

The sealed system is left at 70°C for 22 hour and then washed with methanol and acetone. In total accordance with the Seidl[39], Guyot[40] and Kunin[41] models the porogens mixture has not only the role to dissolve the EDMA and the GMA monomers but it rules the delicate and progressive precipitation of the clusters.

With the process progressing, these clusters will dissolve the residual monomers better than the porogens and, due a concentration effect, the polymerization rate will be faster inside these clusters than in the bulk. This is the main phenomenon driving the pore formation as the initial clusters will gradually cross-link in a unique structure forming the monolith. For this reason it is extremely important to perform step 3 with the cartridge standing in a vertical position. Indeed, a horizontal position would form a not uniform monolith around its symmetry axis.

As a final step, the anchored monolith is washed with methanol, acetone and distilled water (see experimental section for details). The polymeric porous monolith cast under these conditions is a white soft material consisting of EDMA bridged GMA as the ATR-IR spectrum confirms (see Figure 4.8, Inset A and B).

The four micrographs in Figure 4.9 show the just formed polymer under discussion (see C, Figure 4.2) under progressively increased magnification.

The globules, clusters and pores exhibit a regular morphology in agreement with the Seidl, Guyot[42], Kunin[43] models. The high surface area of these monoliths (523.9 m^2/g) [36] is due the presence of these globules.[44]

To confirm the crucial role of the anchoring system, a monolith was cast in a PP housing omitting step 1 and step 2 in Figure 4.2. Figure 4.10 shows the monolith immediately slit out of the housing after a few drops of solvent were pushed through.

Similarly, at the microscopic scale, Figure 4.11 shows the monolith-housing contact surface in the case of absent anchoring system (see Inset A) and properly anchored monolith (see Inset B).

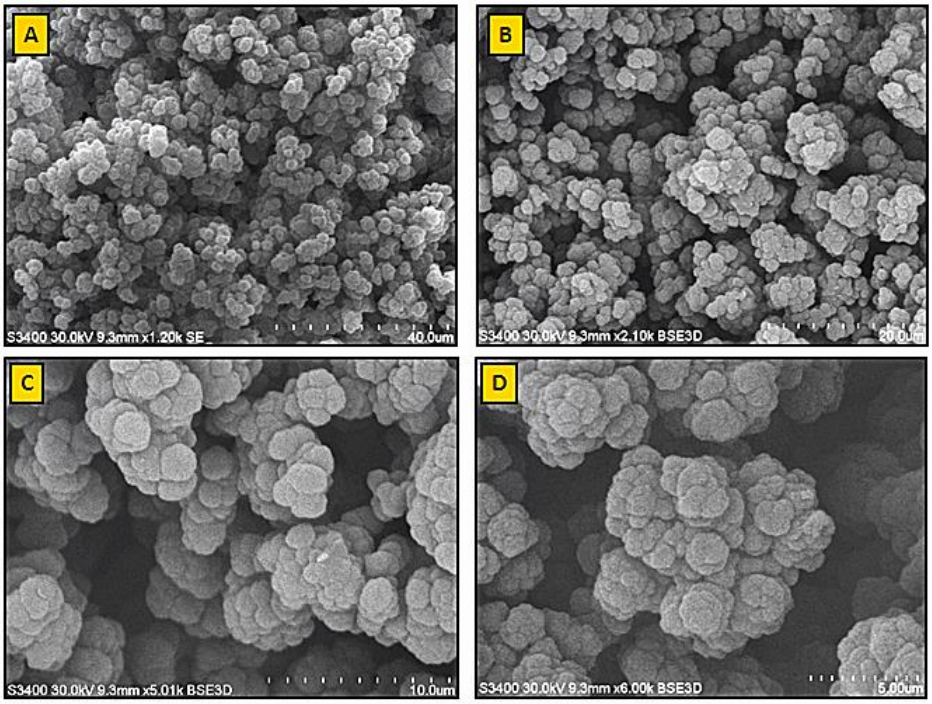

Figure 4.9: The porous poly (EDMA-co-GMA) monolith (see C, Figure 4.2). Inset A, B, C and D are SEM micrographs of the same material at different magnifications. Inset A: Clusters of polymeric globules are visible along with monolith structural pores (scale 40 nm). Inset B: A number of pores is clearly visible (scale 20 nm). Inset C: Details of two pores (scale 10 nm). Inset D: A single cluster of globules is surrounded by pores (scale 5 nm). Sample morphology: globules (1-4 nm), clusters (5-10 nm) and surrounding pores (10-20 nm).

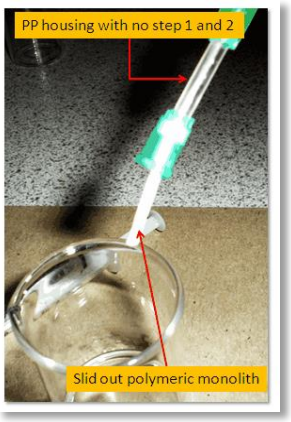

Figure 4.10: A non-anchored housing will not hold the cast polymeric monolith

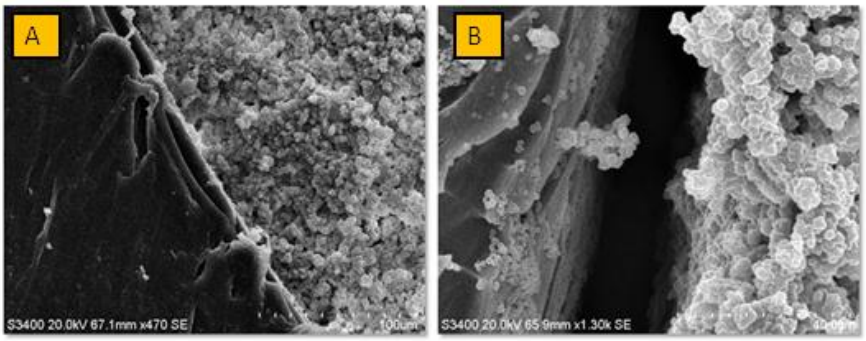

Figure 4.11: The impact of the anchoring system on the monolith (see 3, Figure 4.2) housing adhesion. Inset A: anchored PP monolith; Inset B: not anchored PP monolith. In the case of the non-anchored monolith, there is a large gap between inner PP wall and the monolith due to the poor compatibility between PP and the organic polymerization solution.

4.2 Conclusions

An in-depth investigation of the synthesis of porous polymeric EDMA-co-GMA monoliths in an inexpensive PP housing is presented. Special emphasis was given to the analysis and optimization of the anchoring layer on the PP surface that allows the formation of homogeneous monoliths fully attached to the PP wall. The SEM analysis of the final polymeric monolith demonstrated the presence of the expected globules, clusters and pores in the final monolith.

4.3 Experimental part

Materials

Benzophenone, azobisisobutyronitrile (AIBN), ethylene dimethacrylate, glycidyl methacrylate, 1-4 butanediol, 1-propanol, penta-methyl-diethylene-triamine (PMDETA), methanol, acetone, ethanol from Sigma Aldrich were used as received. Polypropylene tubing is from a Crystal BIC© pen. UV Fusion station is equipped with bulb H UV lamp. Atmos-bag is from Sigma Aldrich.

Methods

A Perkin-Elmer Spectrum 100 was used for collecting attenuated total reflectance Fourier transform infrared (ATR-FTIR) spectra in the spectral region of 650–4000 cm^{-1}. Hitachi S3400n SEM microscope was used as emission electron microscope. UV Fusion lamp station

Preparation of the PP tube (see Figure 4.2, steps I-II)

The PP tubing of a Bic Cristal Pen is removed from the hexagonal barrel. The head is cut off and the ink is left to drain out overnight. Then the tube is washed several times with acetone and ethanol and left to dry in an oven at 40°C during 1 hour. The tube is then capped with luer lock connectors cut from disposable needles. The connection is sealed with Teflon tape (see Figure 4.12). However, if teflon tape is used in the steps 1 and 2 (see Figure 4.2), it is important to cut off 2-3 mm of PP tubing not directly UV light exposed (due the tape light shielding action) as this would result in an inhomogeneity of the anchoring system.

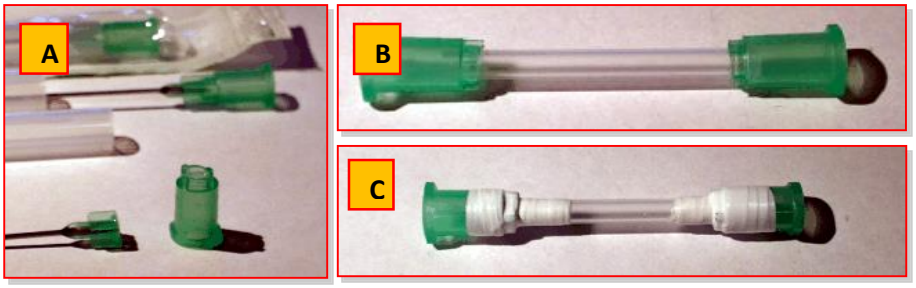

Figure 4.12: Inset A: blade cut luer lock. Inset B: the housing before treatments. Inset C: Teflon tape wound housing for oxygen free conditions.

UV treatment with Benzophenone (step 1, Figure 4.2)

A solution of Benzophenone/MeOH 5/95 wt/wt is transferred in a glass vial sealed with a rubber septum. N_2 is gently bubbled through the system (the vial is connected to a Dreschel bottle filled with mineral oil, h=15 cm) during 15 minutes. Then the luer lock capped tube, the vial, 2X1 mL syringes to be used as stoppers are transferred inside an AtmosBag© and 3 cycles N_2 / Vacuum are applied. Then, the tube is filled

with the solution using the attached syringes and sealed under inert atmosphere. The tube is then UV treated with a Fusion UV lamp for a total of 15 minutes of effective irradiation under oxygen free conditions. When the tubing is exposed to the UV radiation, a side will be belt-faced and the other side will be direct toward the UV bulb (See Figure 4.13, upper Inset). To assure uniformity of the radiation, the tubing is alternatively re-positioned face-up and face-down at each passage. The formation of bubbles during the irradiation due the handling and the increasing inner temperature must be avoided using few second delays between each single cycle. Indeed, the presence of bubbles would be a sign of leaks and possible oxygen presence inside the tubing. The residual BP solution is drained and the BP-PP treated tubing is cleaned with MeOH and dried under N_2. To be noted here, especially after a 15 min treatment, the 5 % wt/wt solution in Methanol tend to exhibit a pale yellow color still being clear. It can be speculated that the yellow color is due to the presence of the BP-BP bi-radicalic termination products.

UV treatment with Ethylene Glycol Dimethylacrylate (EDMA) (step 2, Figure 4.2)

The handling is the same as in step 1 but the solution is Ethylene Glycol Dimethylacrylate /MeOH 5/95 wt/wt. In general, it is a good practice to substitute the plastic luer locks between step 1 and step 2.

Casting the porous polymeric EDMA-co-GMA monolith inside the anchoring system bearing PP tubing (procedure for 10 SPE cartridges, L=2 cm); (step 3, Figure 4.2)

In a glass vial are transferred Azobisisobutyronitrile (AIBN) (3 mg, 1.83 10^{-5} mol), water (70 mg, 3.88 10^{-3} mol), ethylene dimethacrylate (75 mg, 3.78 10^{-4} mol), glycidyl methacrylate (225 mg, 1.58 10^{-3} mol), 1-4 butanediol (280 mg, 3.11 10^{-3} mol), 1-propanol (350 mg, 5.82 10^{-3} mol). The vial is sealed with a rubber septum and well mixed by a vortexing table and N_2 is gently bubbled through the system (the vial is connected to a Dreschel bottle filled with mineral oil, h=15 cm) during 15 minutes. Then the PP tubes with luer locks at the ends, the septum vial with the

monomers/porogens pool, 1 mL syringes to be used as stoppers are transferred inside an AtmosBag© and 3 cycles N_2 / Vacuum are applied. Then, the tubes are filled with the solution and sealed under inert atmosphere. The filled cartridges are left vertically standing in an oven at 70°C for 22 hours and then, at RT, washed with MeOH.

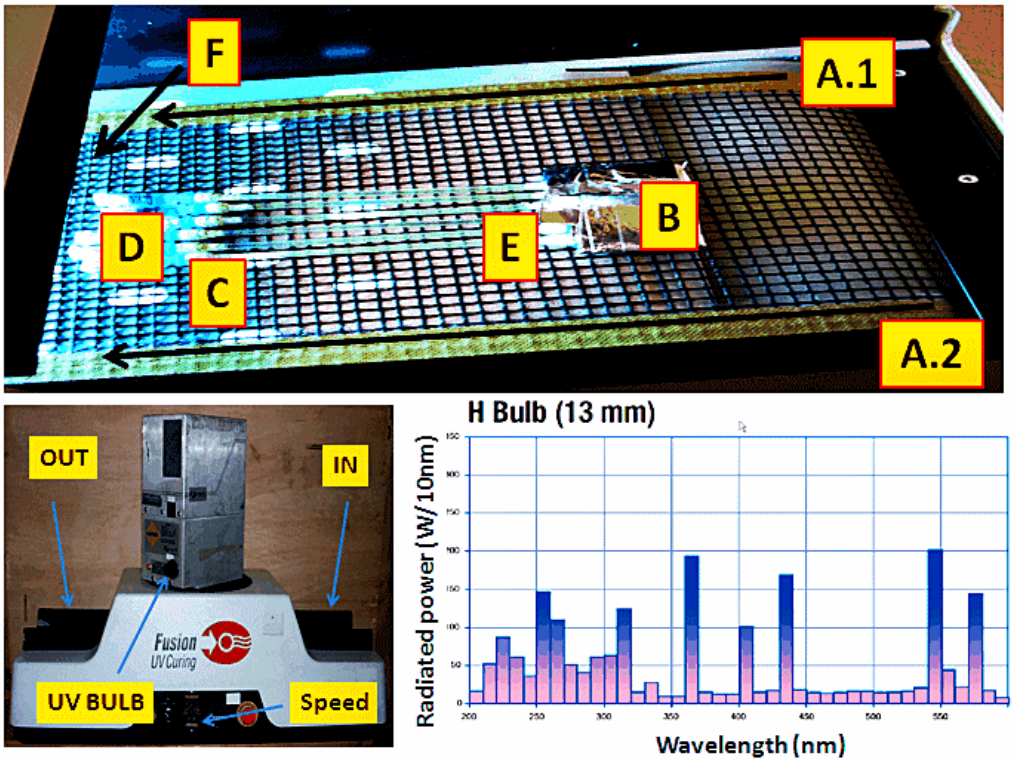

Figure 4.13: Upper inset. Experimental set up for the step A to B and step B to C (see Figure 4.2). A set of 6 X 90 mm sealed solution filled PP tubing. A.1 and A.2 black arrows indicate the horizontally sliding belt. B: aluminum foil to keep the tubing in position. D: the syringes used to seal the tubing with the solutions. C: the Teflon tape used to seal the tubing. E: The tubing filled with the oxygen free solutions (BP or EDMA in turn). Lower left-hand inset: Vision UV curing station. The filled and sealed cartridge is left on the horizontal belt in IN and – after a time depending on the regulated belt speed – collected in OUT. The cycles are then manually repeated a number of times. Lower right-hand inset: The emission spectrum of the contactless H bulb furnished with the Fusion UV Curing station used in this work. Specifically, it is of particular interest the peak at 360-370 nm in the emission bulb of this lamp. Indeed, this is the excitation frequency able to promote the photo-excited triplet state of Benzophenone that is the reactive species for the hydrogen abstraction. [45]

4.4 References

[1] Svec, F. *J. Chromatogr.* B. **2006**, 841, 52

[2] Plieva, F.; Bober, B.; Dainiak, M.; Galaev, I.; Mattiasson, B. *J. Mol. Recognit.* **2006**, 19, 305

[3] Bisjak, C.; Bakry, R.; Huck, C.; Bonn, G. *Chromatographia* **2005**, 62, S31

[4] Han, G.; Ye, M.; Zou, H. *Analyst* **2008**, 133, 1128

[5] Svec, F.; Frechet, J. M. J. *Anal. Chem.* **1992**, 64, 820

[6] Hjerten, S.; Liao, J. L.; Zhang, R. *J. Chromatogr.* **1989**, 473, 273

[7] Svec, F.; Frechet, J. M. J *Anal. Chem.* **1992**, 64, 820

[8] Viklund, C.; Svec, F.; Frechet, J. M. J.; Irgum, K. *Chem. Mater*. **1986**, 8, 744

[9] Seidl, J.; Malinsky, J.; Dusek, K.; Heitz, W. *Fortshr. Hochpolym. Forsh.* **1967**, 5, 113

[10] Guyot, A.; Bartholin, M. *Prog. Polym. Sci.* **1982**, 8, 277

[11] Kun, K. A.; Kunin, R. *J. Polym. Sci.* **1969**, 6, 2689

[12] Viklund, C.; Svec, F.; Frechet, J. M. J.; Irgum, K. *Chem. Mater.* **1996**,8, 774

[13] Eeltink, S.; Hilder, E.; Svec, F.; Kok, W.T. *J. Sep. Sci.* **2007**, 30, 409

[14] Viklund, C.; Svec, F.; Frechet, J. M. J.; Irgum, K. *Chem. Mater*. **1996**, 8, 744

[15] Svec, F.; Frechet J. M. J. *Chem. Mater.* **1995**, 7,707

[16] Svec, F.; Frechet, J. M. J. *Macromolecules* **1995**, 28, 7580

[17] Mudrik, J. M.; Dryden, M. D. M.; Lafreniere, N. M.; Wheeler, A. R. *Can. J. Chem.* **2014**, *92*(3), 179

[18] Mudrik, J. M.; Yang, H.; Wheeler, A. R. Digital microfluidic devices and methods incorporating a solid phase U.S. Patent US20130277218 A1, October 03, 2011

[19] Lin, L.; Chen, H.; Wei, H.; Wang, F.; Lin, J. *Analyst* **2012**, *136*(20), 4260

[20] Bruchet, A.; Dugas, V.; Laszak, I.; Mariet, C.; Goutelard, F.; Randon, J. *J. Biomed. Nanotechnol.* **2001**, *7*(3), 415

[21] Altun, Z.; Blomberg, L.; Jagerdeo, E.; Abdel-Rehim, M. J. *J. Liq. Chromatogr. Relat Technol.* **2006**, *29*(6), 829

[22] Curivan, S.; Connolly, D.; Paull, B. *Microchem. J.* **2013**, 111, 32

[23] Svec, F.; Tennikova T. B., Deyl. Z., Eds., *Monolithic Materials: Preparation, Properties, and Applications*. Elsevier, Amsterdam, **2003**

[24] http://www.youtube.com/watch?v=_1j9_Y8hwRI (accessed 11.09.2013)

[25]http://www.bicworld.com/img/pdf/presskit_60yearsCristal_EN_light.pdf (accessed 12.09.2013)

[26] Steward, N.; Walzak, M. J. *Add. Con. 95: Worldwide Addit. Polym. Modif. Conf., Book Pap.* **1995**, 23, 69

[27] Ryntz, R. A. *Prog. Org. Coat.* **1994**, 25, 73

[28] Garbassi, F.; Morra, M.; Occhiello, E. *Polymer Surfaces*; Wiley: New York, **1994**

[29]Chan, C. H. *Polymer Surface Modification and Characterization*; Hanser: New York, **1994**

[30] Lee, L. M. *J. Adhes. Sci. Technol.* **1991**, 5, 71

[31] Severini, F.; Di Landro, L.; Galfetti, L.; Meda, L.; Ricca, G.; Zenere, G. *Macromol. Symp.* **2002**, 181, 225

[32] Muhlan, C.; Nowack, H. *Surf. Coat. Technol.* **1998**, 98, 1107

[33] Kang, M. S.; Chun, B.; Kim, S. S. *J. Appl. Polym. Sci.* **2001**, 81, 1555

[34] Denes, F. Trends Polym. Sci. (Cambridge, U.K.) **1997**, 5, 23

[35] Castel, P.; Wouters, M.; de With, G.; Fisher, H.; Huijs, F. *J. Appl. Polym. Sci.* **2004**, 92, 2341

[36] Ma, H.; Davis, R. H.; Bowman, C. N. *Macromolecules* **2000**, 33, 331

[37] Yang, W.; Rånby, B. *J. Appl. Polym. Sci.* **1996**, 62, 1723

[38] Maribeli, F. M. Principles, Theory, and Practice of Internal Reflection Spectroscopy, Internal Reflection Spectroscopy-Theory and Applications, ed. FM. Mirabella, Jr., Marcel Dekker, Inc.: New York, 1993

[39] Seidl, J.; Malinsky, J.; Dusek, K.; Heitz, W. *Fortshr. Hochpolym. Forsh.* **1967**, 5, 113

[40] Guyot, A.; Bartholin, M. *Prog. Polym. Sci.* **1982**, 8, 277

[41] Kun, K.A.; Kunin, R. *J. Polym. Sci.* **1969**, 6, 2689

[42] Guyot, A.; Bartholin, M.; **1982**, *Prog. Polym. Sci.*, 8, 277

[43] Kun, K. A.; Kunin, R.; **1969**; *J. Polym. Sci.*, 6, 2689

[44] Svec, F.; Tennikova, T. B.; Deyl, Z.Monolithic Materials: Preparation, Properties and Applications, Elseiver:Amsterdam, **2003**

[45] Mita, I.; Takagi, T.; Horie, K.; Shindo, Y.*Macromolecules* **1984**, 17, 2256

Chapter 5: Solid phase extractions using surface nano-brushed polymeric monoliths: analytical performances and brush enhancement factor

5 Introduction

The last 30 years witnessed a growing permeation of nano-technologies into the field of the analytical chemistry and inspired numerous developments. This interdisciplinary research combination featured two parallel approaches. One is focused on nano-technology for specific analytical applications such as mass spectroscopy[1], sample preparation[2], electrochemical sensors[3-6] and diagnostics[7]. The second approach is bottom-up and focuses on a particular kind of nano-particles, for example the integration of magnetic nano-particles for analyte handling, chemical sensors, and imaging techniques[8], as well as gold nano-particles uses and applications in analytical techniques[9] and the use of carbon nano-tubes.[10,11]

On this basis it is not surprising that there are a number of informative reviews and publications covering analytical chemistry studies on porous polymeric monoliths and their nano-particles surface decoration for chromatographic applications.[12-14] The particular aim of the present work, i.e. the use of nano-particle surface enhanced porous polymeric monoliths for solid phase extractions of bio-molecules, was recently reviewed by Blomberg.[15] These open porous polymeric monoliths are easy to prepare and modify to tailor specific surface chemistry thus making them versatile substrates to explore nano-particles/surface interactions. Indeed, the resulting hybrid materials would still retain a convection dominated mass transfer typically promoted by these monoliths.[16] Porous polymeric monoliths decorated with different types of nano-particles are nowadays a well-established field in material science with applications in separation science as briefly summarized in the following.

- Monoliths modified with metallic nano-particles: This class includes iron oxide nano-particles with diameters ranging from 50 nm[17,18] to 20 nm[19] in 10-50 µm pore size cryogel porous polymeric monoliths for studies on increase of binding capacity of proteins, 50 nm silver nano-particles on poly(glycidyl methacrylate–co- trimethylpropane tri-acrylate) monoliths [16], 20 nm gold nano-particles, featuring ideal surfaces for protein immobilization, on poly(butyl methacrylate-co-ethylene dimethacrylate) monolithic phases[20,21] and gold nano-rods[22]. The use of metallic nano-particles also includes less

common 10 nm Ni-Co nano-particles on polymeric monoliths[23] and titanium oxide 20 nm particles on EDMA-based monoliths[24].

- Monoliths modified with inorganic nano-particles: 20-40 nm silica nano-particles have been used in the context of the synthesis of cryogels and the new material tested in lysozyme binding tests[25], nano-meter scale hydroxyl-apatite have been incorporated in a poly (2-hydroxyethyl methacrylate-co-ethylene dimethacrylate) monolith and tested in the separation of Protein A/IgG2 antibody complex[26].
- Monolith modified with carbonaceous nano-particles: The pioneering work on the study of the interactions between a poly(divinyl benzyl chloride-*co*-ethylene dimethacrylate) and single-walled carbon nano-tubes has been published in 2005 followed by more recent work of the multi-walled carbon nano-tubes version on an poly(glycidyl methacrylate-co-ethylene dimethacrylate) monolith.[27,28] These reports focus on the separation of a mixture of peptides. Another carbonaceous material, C_{60}-Fullerene, has been used in studies on ethylene dimethacrylate based porous monoliths in 2011.[29] The more recent application in this family of nano-objects is the use of graphene oxide nano-sheets on small organic molecules.[30]
- Monolith modified with polymer particles: The pioneering work of Hilder focused on the use of quaternary anime-functionalized 60 nm latex nano-particles on poly(butyl methacrylate-co-ethylene dimethaxcrylate-co-2-acrylamido-2-methyl-2-propanesulfonic acid) porous polymeric monoliths.[31]

The cited four classes of particle modified porous polymeric monoliths are far from being a comprehensive list on the topic but give an impression of this extremely vibrant field of research.

To complete this overview on nano-particle modified monoliths, it is crucial to provide the most representative approaches used to decorate these systems with the nano-particles. Due to the large variety of chemistries available, there are a number of different approaches to synthesize a monolith with a surface decorated by nano-particles and for reasons of brevity only a few possible approaches will be highlighted:

- Electrostatic post immobilization: In this approach a suitable bare porous polymeric monolith is treated to introduce chemical groups able to promote the presence of permanent electrostatic charges used to trap nano-particles bearing opposite charge. Once the proper monolith is formed, a suspension of nano-particles bearing the opposite electric charge on the surface is flushed through and the monolith surface is gradually saturated with a monolayer of nano-particles. Hilder, the pioneer in this research filed, demonstrated how a negatively charged co-polymerization agent (2-acrylamido-2-methyl-1-propanesulfonicacid) used in the synthesis of a methacrylate neutral monolith is able to enhance the surface coverage by positively charged amino modified latex nano-particles.[32]
- Encapsulation of the nano-particles within the monolith during casting step: In this technique the nano-particles are added during the formation of the monolith. It has to be considered, however, that the delicate equilibria between the monomers, formed oligomers and the mixture of porogenic solvents during the monolith casting step are further complicated by the interactions of the surface of the nano-objects. Consequently, the risk of nano-particle aggregation and segregation is high. For this reason, a number of optimized techniques involving the use of monomers bonded to nano-particles for the monolith casting step is used.[33]
- Formation of nano-particles inside a pre-formed monolith: In this technique, the nano-particles are actually formed inside the monolith. A classical work on this approach was published by Xu: an EDMA-co-GMA monolith modified with thiol groups had been treated with two separate solutions of gold chloride and sodium citrate to form *in situ* gold nano-particles. [34]

Currently, nano-particle decorated monoliths are mainly explored in research laboratories but they hold significant application promise once all technological gaps have been overcome. This also includes the development of better theoretical models. For example, the laws of adhesion of a nano-particle on a surface are far from to being understood as the macroscopic law of friction does not generally apply to nano-scale contacts.[35]

The work presented in this chapter is dedicated to the use of the brushed p(MAA) silica nano-particles (presented in the chapter 2 and 3) as nano-systems to decorate the surface of polymeric porous monolith based solid phase extraction device (detailed in the chapter 4). As a first step, the advantage to use a brushed nano-particle to decorate the surface of a solid phase extraction device is discussed as oppose to using nano-particles bearing just a monolayer of functional group (see paragraph 3). In the second part of this chapter, there is a section dedicated to the chemical modifications at the monolith surface to electrostatically trap the negatively charged brushed p (MAA) silica nano-particles. Under this aspect, the inexpensive device used in this study can be considered as a model system for solid phase extraction devices manufacture. Moreover, a new nano-particle encapsulation approach is detailed as an appealing process able to overcome some of the manufacture problems affecting the "pure" electrostatic approach. Finally, the solid phase extraction data forms the third and conclusive part of this study. It describes the parameters derived from solid phase extraction breakthrough curves confirming the positive impact on the extraction performances of the brush enhancement factor. The new material present unprecedented performances even if compared to the commercial extraction devices as it will be briefly detailed in the discussion.

5.1 Results and Discussion

5.1.1 Geometrical considerations and brush-enhancement factor

There are two main reasons to decorate the surface of a porous polymeric monolith with nano-particles. On one hand, the resulting monolith total surface is incremented with respect to the starting monolith. On the other hand, the nano-particle surface can introduce functional groups over the monolith surface. In the following short discussion, the geometric nature of this problem is introduced. Moreover, the advantage in using brush-decorated nano-particles compared to nano-particles just bearing chemical surface groups is investigated.

On the simplifying hypothesis of rigid spheres and a flat square surface portion of the monolith of X^2 nm^2 surface area, an assemblage of n^2 spheres of the radius X/(2n) can be packed in a square matrix-like arrangement of n*n spheres (see Figure 5.1). In this case, the total surface area of these n^2 spheres would be $\pi*X^2$ nm^2. Therefore, the sphere-deriving surface area increment with respect to the square surface considered would be a π time increase. On this basis, a roughly 3 time (π) increase in the total surface area would be achieved irrespective of the diameter of the considered nano-particles. This value is not even considering real scenarios of 3-dimensional surfaces or non-ideal spheres packing efficiency. An enhanced extraction process based only on the surface area enhancement derived from bare nano-particles would have, for this reason, only limited impact. However, a brush surrounding a nano-particle, with its controlled thickness and volume would make a more important contribution if the amount of the carried functional groups were considered. For the same nano-particles covered surface in a n*n square matrix configuration, the situation changes if brushed nano-particles are considered being K the brush thickness express as a fraction of the total nano-particles radius (ranging from K=1, in the case of a bare non brush bearing silica nano-particles, to K=0, in the case of a nano-particles made only of polymeric brush; see Figure 5.2). Simple mathematical manipulations confirm that the total volume of the polymeric brush would decrease as $-(1/n^2)$ if K is kept constant while, if the diameter n is kept constant, a variation in K would increase the total brush volume as K^3. As a direct consequence of these trends, a lower nano-particles diameter (if K is fixed) would negatively impact the amount of functional groups, e.g. methacrylic acid, introduced to the monolith surface by the nano-particles brush. Conversely, if n is kept constant and K increased, the amount of methacrylic acid introduced to the monolith surface would significantly increase (as a power of 3). These considerations are important to prevent any misunderstanding on the geometric nature of these nano-brushed systems and to define future comparative experiments in the proper way.

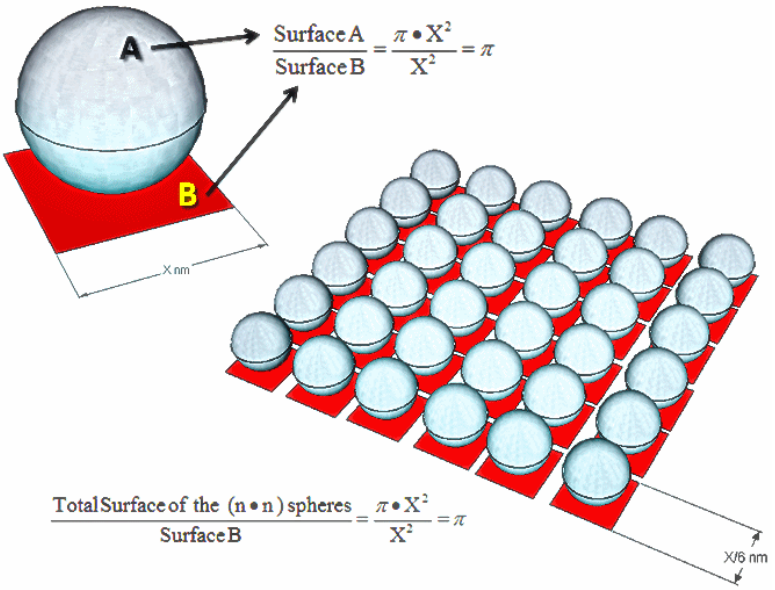

Figure 5.1: A sphere A of radius X/2 nm has a surface of πX^2 nm^2 resulting in a surface π times bigger than the square surface B of X^2 nm^2. This ratio B/A=π remains unmodified if the square surface B is covered with a (n x n) square collection of spheres of the same radius 1/2n. For the example of 6X6 spheres, the sum of these 36 spheres will have a surface π times bigger of the square surface B of X^2 nm^2).

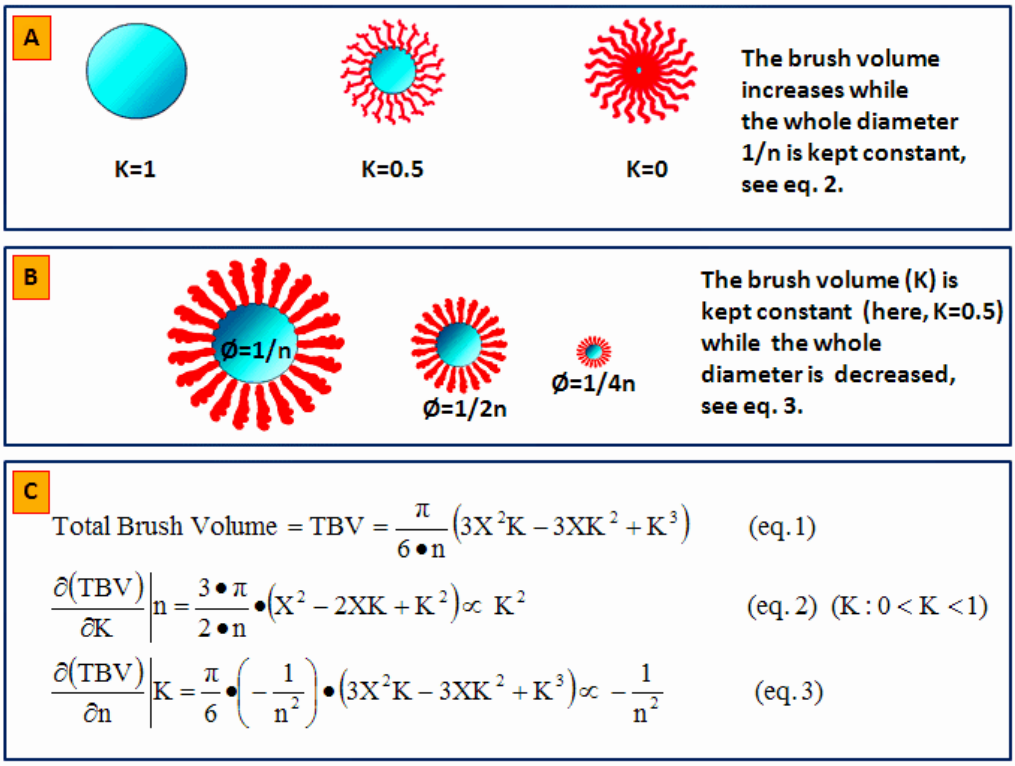

Figure 5.2: Inset A and eq.2 in the Inset C: three nano-particles of the same total diameter (X\n) are depicted, K being the brush thickness increased from the left (K=1, no brush) to the right (K=0, all brush). The total amount of brush carried functional groups increases with K decreasing. Inset B and eq. 3 in the Inset C: three nano-particles of the three different diameters are depicted. In each case, the brush thickness is half of the whole nano-particles diameters (K=0.5). The total amount of brush carried functional groups decreases with n increasing.

5.1.2 Monolith decoration with poly (methacrylic acid) fluorescent silica nano-particles by electrostatic trapping approach

In Figure 5.3 a negatively charged poly(methacrylic acid) brush nano-particle (see Inset A) and the positively charged ammonium modified monolith surface (see Inset B) used in this study are shown. While both electrostatic and frictional forces will contribute to the nano-particle trapping process, the individual contributions of both forces are not yet fully understood. For sure, the electrostatic interactions participate in this process and the fact that the surface and the to-be-trapped nano-particles are both of hydrophilic nature influence the delicate nano-particles "surface landing process" when the double layers on the nano-particles and the monolith surface have to interact. Moreover, frictional forces at the nano-scale might play a significant role.

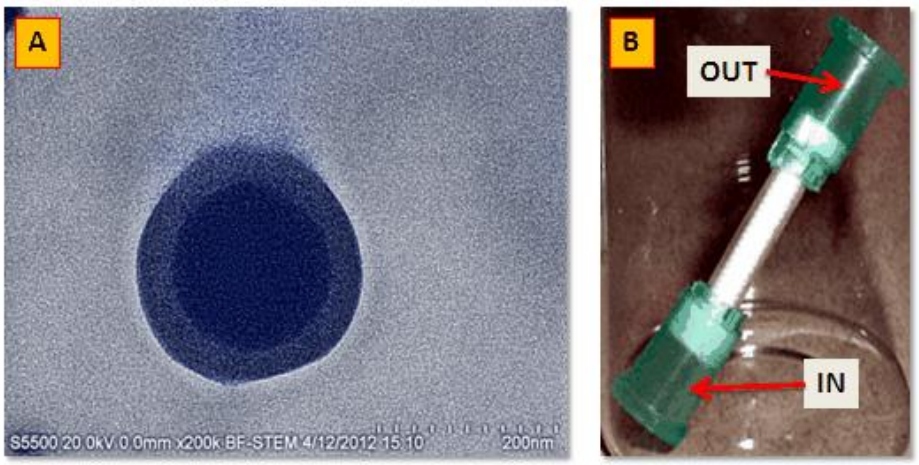

Figure 5.3: Inset A: Bright Field SEM micrograph at 20.0 kV of a poly (methacrylic acid) brush decorated core fluorescent silica nano-particle used in this study (diameter: ca. 190 nm; brush thickness: ca. 40 nm). This system is from the same batch of the Sample No. 4, Table 3.1 Chapter 3 (De-protected version). Inset B: Ammonium modified EDMA-co-GMA porous polymeric monolith. Monolith length: 15 mm; monolith inner diameter: 2 mm; mass of the polymeric bead 13.8 mg; monolith surface area from literature data[36] for the EDMA-co-GMA monolith: 7.2 m^2; epoxy content, based on the assumption that all the GMA monomer used to cast the monolith is present in the final monolith 7.21 10^{-5} mol.

Figure 5.4 summarizes the chemical modification steps from the EDMA-co-GMA bare monolith to the brush nano-particles decorated monolith. The GMA monomer

possesses an epoxy ring, which is a good reaction site for nucleophiles at the less sterically hindered epoxy carbon atom. Normally a 2 to 10 fold excess of nucleophiles is able to promote the reaction with the epoxy group in a reasonable time.[37] It is worthwhile to emphasize that these considerations are valid in the ideal case of a reaction system in solution. Indeed, in the specific context of the modification of the EDMA-co-GMA porous monolith, the epoxy rings are part of the less accessible polymer network and are part of the rigid monolith structure and surface. For this reason, more drastic reactions conditions are required and the uniformity of the reaction must be carefully monitored across the monolith length by ATR-IR.

For analysis purposes the monoliths were therefore divided in 5 sections (each one 3 mm long), which were analyzed individually for all the modification steps under study. Unless specifically noted in the discussion, analysis results were identical for the sections suggesting homogeneous transformations.

The surface modification of the initial monolith (see Figure 5.4, Conditions a, Inset B) entails an acid catalyzed nucleophilic bimolecular substitution reaction SN_2 of the tri-methylamine hydrochloride (TMA HCl) on the less substituted carbon atom of the epoxide ring. For this modification step, two experimental approaches were investigated. In the dynamic approach, the reactants solution is flushed trough the monolith at a specific flow rate, concentration, times and temperature conditions (see Figure 5.5).

In the static approach the monolith is filled with the reactant solution, sealed and placed in a temperature controlled oven for a definite time. In both cases, a total of 7.21×10^{-5} mol of GMA in the monolith was assumed according to initial concentration in the formulation used to cast the polymeric monolith. The reactant solution used is 1.05 M in TMA HCl, i.e. a large molar excess with respect to the GMA epoxy groups is used (~ 14500 molar equivalents). It was found that prolonged (24 h) reaction times at 100 °C are necessary to obtain a homogeneous surface treatment.

Figure 5.6 shows the ATR-IR spectra of the initial EDMA-co-GMA monolith (Inset A) and the ammonium-modified monolith (see system 2, Inset B, Figure 5.4) for one test

done under dynamic conditions. The epoxy ring signals in the Inset A of Figure 5.6 feature two peaks of the same intensity at 850 (peak 2) and 900 cm^{-1} (peak 1).

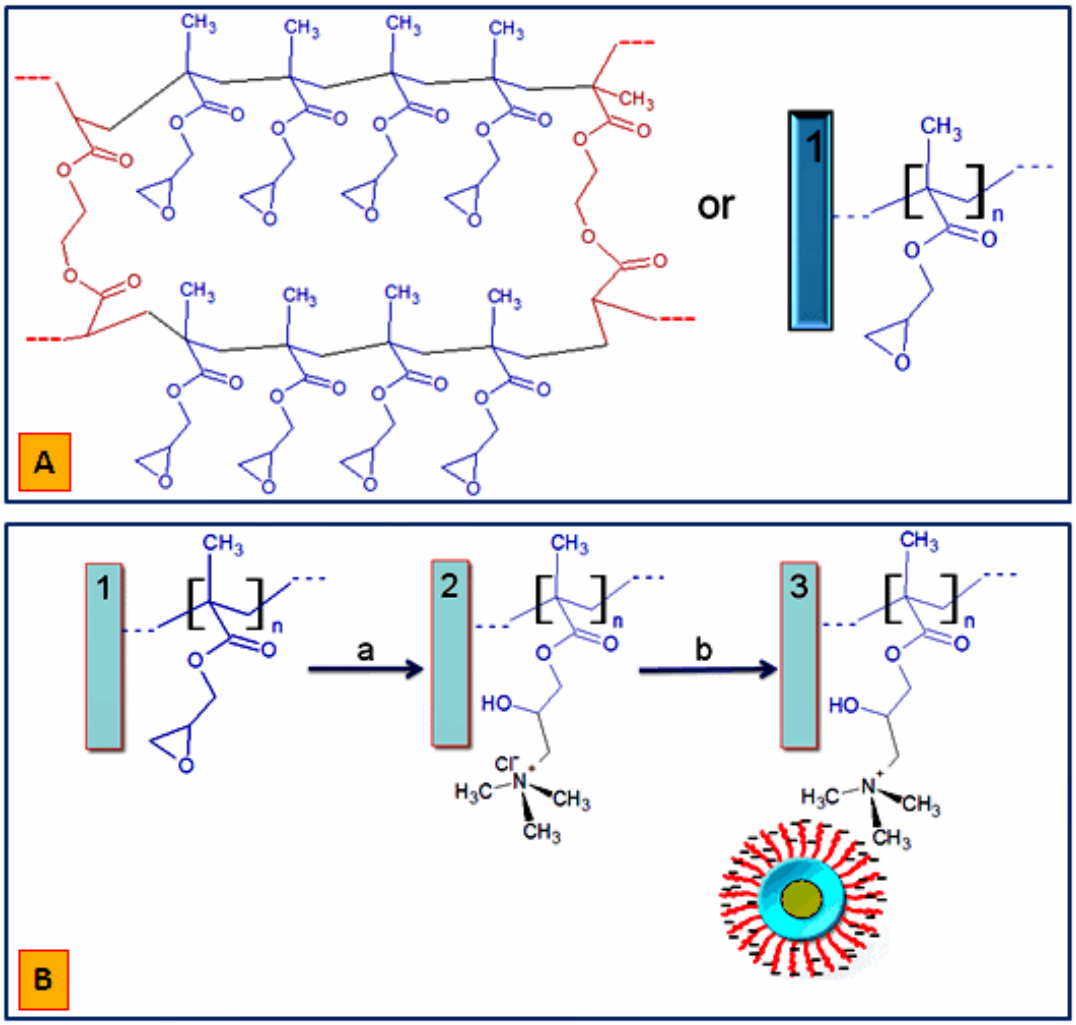

Figure 5.4: Inset A: Representation of the initial EDMA-co-GMA monolith network with the EDMA chains in red and the GMA chains in blue and its simplified representation. Inset B: Chemical modifications steps from the EDMA-co-GMA monolith (material 1) to the nano-particle decorated monolith (material 3). Reaction a: TMA HCl, 1.05 M, 100° , 24 hs). Surface decoration process b: 100 mL of a 0.5 mg/mL brush poly (methacrylic acid) suspension (see Inset A, Figure 5.3) flushed at flow rate of 2000 µL/h (see details in the experimental section). Material 3 can be formed by a new encapsulation approach as will be shortly detailed. The brush poly (MAA) core FITC silica nano-particles specifically used in this study are from the same batch of the Sample No. 4, Table 3.1 Chapter 3 (De-protected version).

After the reaction, these two peaks disappeared, suggesting quantitative reaction at the epoxy ring. If the monolith is treated with a lower concentration of reactant (e.g. 0.5 M in TMA HCl or ~ 5000 molar equivalent with respect to the epoxy ring), irrespective of whether the static or dynamic approach is used, the reaction time to reach quantitative and homogenous conversion was prolonged (2 weeks). Finally it is important to store the modified monolith sealed in a vacuum desiccator to avoid any device surface doping by volatile nucleophiles, grease, dust, etc.

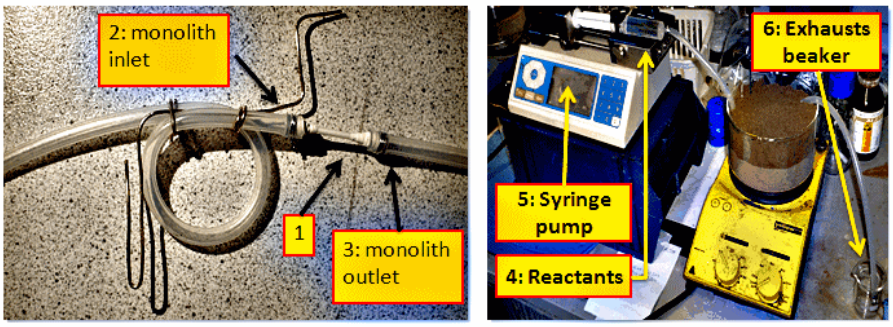

Figure 5.5: Experimental setup of the monolith surface modification by dynamic approach. The tubing connected cartridge (1) is sand covered in a sand bath on a heating plate and connected to a syringe pump (5). The upper sand layer is left wet in order to assure a better heat transfer to the device. The monolith (1) ends are fixed to two PP tubing. The tubing loop at the monolith inlet assures the reactants to be at the desired temperature before entering the monolith. At the end of each treatment, the surface modified monoliths are flushed with acetone, methanol and water and then stored at RT.

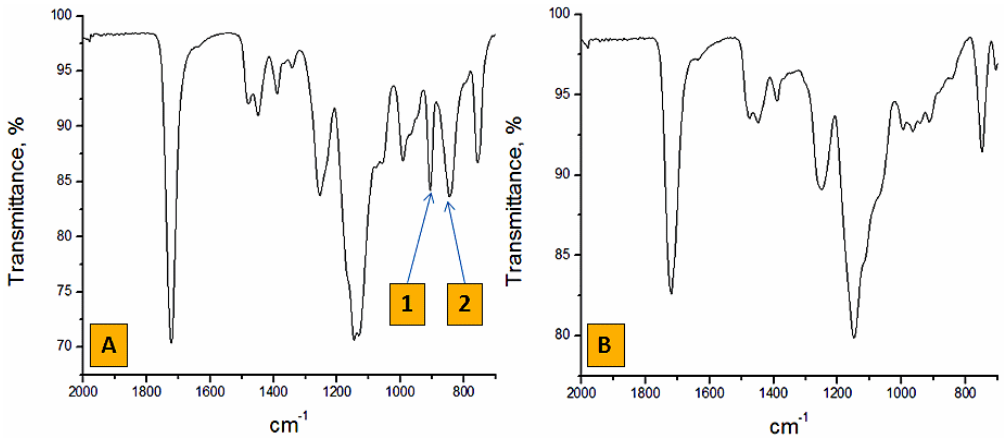

Figure 5.6: Inset A: ATR-IR spectrum of the EDMA-co-GMA monolith (starting material 1 in Figure 5.4, Inset B). Peak 1 and 2 are diagnostic for the epoxy ring. Inset B: the ammonium modified EDMA-co-GMA monolith, dynamic approach (see material 2, Figure 5.4, Inset B).

The reaction **b** (see Figure 5.4, Inset B) is the monolith surface nano-particles decoration. Two important aspects for a successful electrostatic nano-particle

surface decoration of a monolithic material are the suspension flux trough the modified monolith and the nano-particles mass content in the suspension. Indeed, if the suspension flux is excessively high, a nano-particles 'cake' preferentially forms at the monolith inlet as the monolith would behave as a filter as observed in initial experiments. This results in a back pressure increase that can expel the monolith device from the screw pump piston (to be noticed here that, in no case, the monoliths have been expelled from their housings and this fact is a further proof of the anchoring system's robustness detailed in the Chapter 4). Conversely, if the suspension flux is excessively slow, the time to decorate the surface would become impracticably long. Similar problems would arise in the case of suspensions when high or low concentrations of nano-particles are used. Through a number of tests the following optimized parameters for a 15 mm long, 2 mm in diameter ammonium modified EDMA-co-GMA monolith (system b in Figure 5.3) were determined. Suspension mass content 0.5 mg/mL of brush poly(methacrylic acid) core fluorescent silica nano-particles, diameter: 200 nm, brush thickness: 40 nm (The system here considered is from the same batch of the Sample No. 4, Table 3.1. in Chapter 3 (de-protected version)); solvent: water; flow rate: 2000 µL/h. 100 mL of this suspension are used to reach the nano-particles decoration saturation conditions. The flow direction is reversed each 5 mL, to maximize the decoration uniformity. For the last 30 mL of this milky yellowish suspension pumped through the monolith no change in its cloudiness is observed indicating that surface saturation has been reached. By comparison with an untreated ammonium modified monolith, the mass increment is 31-32 mg due to the presence of the brush nano-particles (both monoliths were dried under the same conditions for 5 days at 0.1 mbar at RT).

The uniformity of the nano-particle layer on the monolith surface was monitored by SEM (see Figure 5.7). On one hand, the brush poly(methacrylic acid) silica nano-particles (see Inset A, Figure 5.7; nano-particles diameter: 200 nm) and on the other hand, the 2-3 µm sized EDMA-co-GMA monolith globules (see Inset B, Figure 5.7) can be identified. A rough visual comparison of the relative dimensions of the nano-particles and the globules suggest space for 4-6 nano-particles per globule as confirmed by SEM (see, as an example, Figure 5.8, Inset A). The SEM image of the final nano-particle decorated surface (see Inset D, Figure 5.7) shows a fully

homogeneous nano-particle monolayer while the porous structure of the monolith is not affected, as evidenced by the presence of the 5 µm channels.

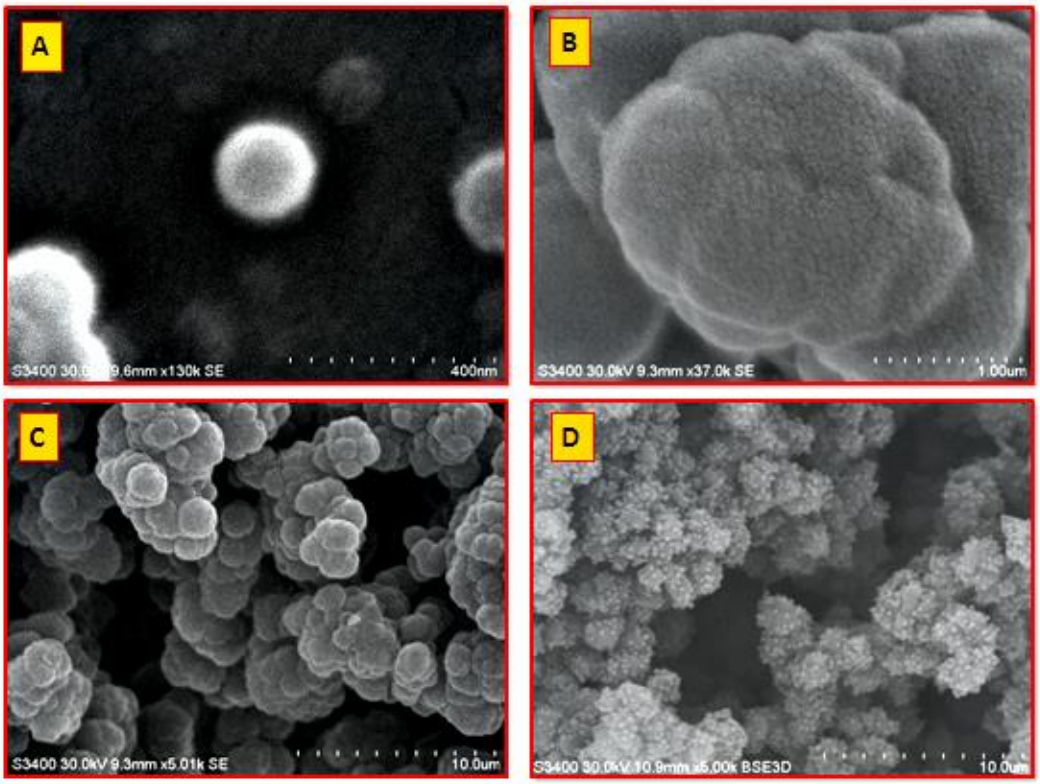

Figure 5.7: Inset A: Brush nano-particle at 135 kV at 400 nm scale (the electrons scattering is evident at these energies, see the intense white shadow surrounding the nano-particle). Inset B: Bare EDMA-co-GMA porous monolith surface (a globule) at a 1 µm scale at 37 kV (see material 1, Inset B, Figure 5.4). Inset C: Clusters of globules and two channels of a monolith at a 10 µm scale at 5 kV (see material 2, Inset B, Figure 5.4). Inset D: Brush nano-particle surface decorated monolith at a 10 µm scale at 30 kV (see material 3, Inset B, Figure 5.4 and Sample No. 4, Table 3.1 Chapter 3 (de-protected version)). The SEM samples are gold sputtered and the gold layer is expected to be ~ 20 nm thick.

A visual inspection of SEM images of the decorated monolith at different positions showed quite uniform nano-particles decoration, although a higher density of nano-particle in the centre of the monolith is noticeable (see Figure 5.8). This result is fully reproducible as evident from the analysis of three monoliths 15 mm long of the same nature. The monolith surface seems to trap the nano-particles somewhat better at the centre of the system. It is possible to argue that this subtle difference could be caused by some local effects on the brush nano-particles kinetic energy spread. The nano-particles flowing in the monolith, after few initial non-trapping collisions on the monolith surface/channels would have a more uniform distribution of the kinetic

energies and so causing a more efficient surface trapping frequency. It is the first time this trend is documented and it would merit the definition of a quantitative model in a future work.

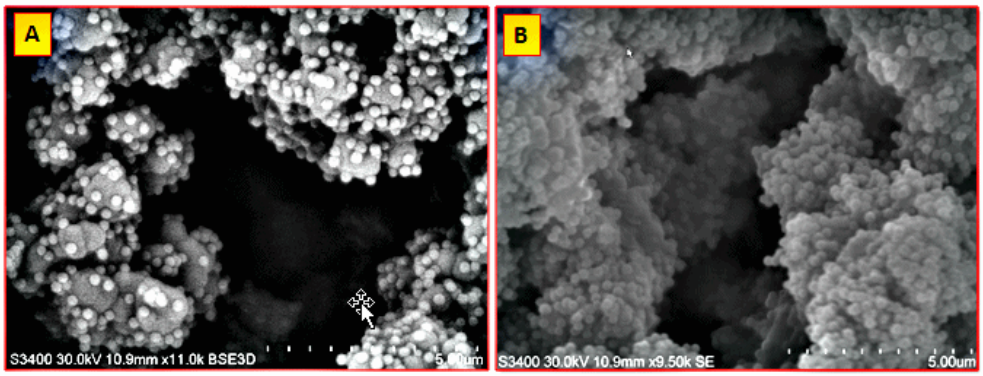

Figure 5.8: SEM images taken at different sections of a nano-particle decorated ammonium modified monolith (see material 3, Inset B, Figure 5.4). Inset A is the section 2 of 5 and Inset B is the section 3 of 5 at a 5 µm scale. (Each 15 mm monolith have been cut in 5 equal sections of 3 mm)

Table 5.1: Five brush nano-particles surface decorated ammonium modified monolith (see material 3, Inset B, Figure 5.4) are dried 5 days at 0.1 mBar, RT, weighed and then flushed with solutions of different pH. Flow rate 2000 µL/h. The original monolith weight is ca. 45-46 mg of which ca. 30-32 mg stems from brush nano-particles. Errors are in the order of no more than 0.3 %.

Solution flushed	Weight loss (%) 10 ml flushed	Weight loss (%) 100 ml flushed	pH
0.1 M PBS	1	3	7.4
HCl	1	2	4.5
HCl	1	3	6.0
NaOH	2	4	8
NaOH	3	4	9.5

The results in Table 5.1 and the SEM images in Figure 5.8 demonstrate the robustness of the electrostatic nano-particles/surface interactions under a large pH range and elution volumes. In no case, the mass loss was higher than 4 % of the initial mass.

This adhesion robustness can be rationalized by the cooperative nature of the interaction. For each single nano-particle, there is a large number of trapping electrostatic nano-particle/surface interactions able to prevent the “washing out” of the nano-particles in the presence of competing ions.

Moreover, it is possible to envisage a more subtle effect of local buffering action from the remaining free residual methacrylic acid groups. Indeed, if the system is flushed with HCl, the acid-base equilibrium of a part of the polymerized methacrylic acid is shifted in favor of the COO^- groups by the common ion effect.[38] The newly generated protons from the brush can trap the Cl^- ions from the flushed HCl solution being in the same time the electrostatic interaction reinforced by the increment of the COO^- groups. On the contrary, if a NaOH solution is flushed through, for the same reason, the acid-base equilibrium of a part of the polymerized methacrylic acid is shifted in favor of the COOH groups. The OH^- in excess would preferentially participate in nucleophilic reactions on the carbonyl group on the polymer chain. In this way, this buffering action would be able to explain the suppression of ion-exchange reactions able to remove the nano-particles from the surface during the extractions. On top of that, as mentioned in the introduction, frictional forces can complement the electrostatic interactions.

5.1.3 Monolith decoration with poly(methacrylic acid) fluorescent silica nano-particles by encapsulation approach

The monolith surface decoration by the electrostatic approach is a robust procedure but it suffers from some practical drawbacks. In particular, a 100 mL nano-particle suspension must be flushed through the 15 mm long monolith at 2000 µL/h, i.e. 50 hours of work are required to saturate the monolith surface. Moreover, the flow direction is reversed every 5 mL (to favorite the decoration uniformity) making this process labor intensive. The attention for the alternative encapsulation approach aims at eliminating these problems. In particular, this approach combines the

advantages of the electrostatic approach (as a uniform and strong nano-particles surface trapping action) with the advantages of the encapsulation approaches (as a faster one pot molding process).

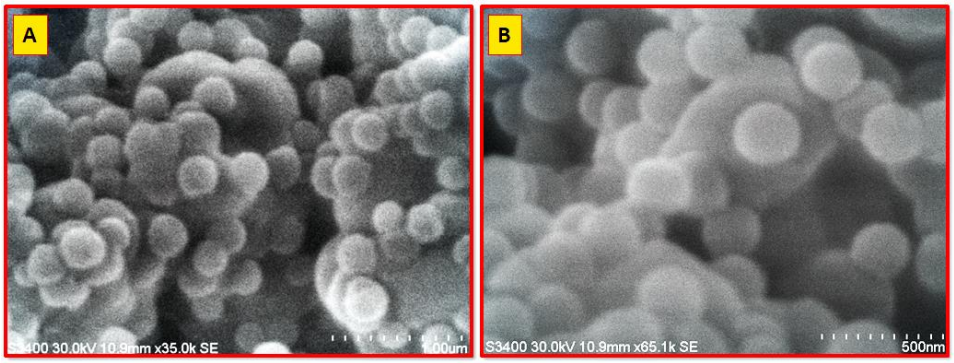

Figure 5.9: SEM images of nano-particle decorated monoliths (see material 3, Inset B, Figure 5.4) after being flushed with the solutions in Table 5.1. Inset A: sample directly comparable with the system in the Inset A of Figure 5.8 (the monolith is cut at the same height, the section 2 of 5), flushed with 100 mL of 0.1 M of PBS (scale 5 µm). Inset B: sample flushed with 100 mL of HCl at pH=4.5 (scale 500 nm) (similarly to Inset A, section 2 of 5). (Each 15 mm monolith has been cut in 5 equal sections of 3 mm).

The encapsulation strategy is very simple: to a standard EDMA–co-GMA monolith mixture are added brush nano-particles used in this study (see Inset A, Figure 5.3) and a previously prepared ammonium modified EDMA-co-GMA monolith reduced to a fine powder (see Inset B, material 2, Figure 5.4). This just formed blend is ultra-sonicated for 5 minutes and the suspension is transferred into a sealed vial and gently nitrogen purged for 15 minutes. This oxygen free suspension is then transferred in the polypropylene housing (as detailed in the Chapter 4) in nitrogen purged AtmosBag as for a classic bare monolith manufacture. This is a very delicate stage as great care must be taken in order to avoid the presence of bubbles in the transferred dense liquid mixture. After attaching syringes at both ends, the mixture is flushed back and forth through the housing a number of times to assure the absence of such bubbles. Then the carefully sealed monolith is thermally cured as done for a bare monolith.

The rationale for this approach is based on the well consolidated literature on the mechanisms of pore formations in the monoliths.[39-41] Indeed, the monolith phase is made of porogenic solvents, structural and function bearing monomers in presence

of thermal initiators. The mixture is then heated and initiating radicals are generated. The oligomers formed in the starting phase become insoluble and tend to precipitate in the continuously changing reaction medium due their lack of solubility in the porogens: Indeed, the insoluble gel-like polymeric nuclei swell preferentially with the monomers and the polymerization continues preferentially inside these primary nuclei. The initially formed globules, enlarged by the progressing polymerization, cannot interpenetrate due the presence of cross-linking monomers and, on the other hand, are held together by side polymer chains. In the final stages of the monolith formation, the interconnected matrix becomes progressively reinforced by the last residual polymerization products. This process is based on the suspension stability (almost two hours). Indeed, under poor stability conditions, the sedimentation of the added brush nano-particles would occur resulting in their non-homogeneous distribution along the standing monolith (more nano-particles at the monolith bottom).

The addition of grinded ammonium modified EDMA-co-GMA monolith (see material 2, Inset B, Figure 5.4) to the starting polymeric suspension used to cast the final monolith is aimed to elicit the electrostatic trapping action on the brushed nano-particles. This is the first time this kind of procedure is detailed in the literature: During the monolith formation, the finely grinded ammonium modified EDMA-co-GMA monolith is electrostatically trapped on the brush nano-particles surface and, at the same time, inter-penetrated in the cross-linked network forming nuclei of the incipient EDMA-co-GMA monolith. Arguably, the ammonium modified EDMA-co-GMA monolith is able to interact hydrophilically with the brush on the nano-particles and, in some extent, as well with the progressively forming EDMA-co-GMA monolith. At the end of the casting step the monolith is flushed with distilled water. After 0.5-1.0 mL of cloudy effluent (after lyophilization of this centrifuged eluate, a residual mass of 1-2 mg has been collected), a clear colorless solution (15 mL) appears with no evidence of nano-particles being washed out from the system. The time required to produce monoliths by this method is 22 hours. Moreover, during the casting-decorating step the system is left standing vertically undisturbed while, in the electrostatic approach an active operator is needed to reverse the flush direction over 50 hours. The drawback of this technique is the need to use larger amounts of

brush nano-particles to form the monolith. Indeed, in order perform the nitrogen bubbling step before the casting step, typically a minimum suspension volume of 10 mL is required: For smaller volumes, the even kind bubbling process (typically 1 bubble per s) could result in the volatilization of part of the solvents in the blend and consequent alteration of the porogens/monomers molar ratio. In a typical blend of 10 mL, 210 mg of brush nano-particles are used. It is here important to note how, no matter which of the two methods are used, the final concentration of brush nano-particles is 50 mg for a 15 mm long monolith.

The SEM micrographs in Figure 5.10 confirm that this method is equivalent to the electrostatic approach clearly showing brush nano-particles on the monolith surface with a comparable density of brushed nano-particles per nm^2 (in the limits of the visual inspection used in this first study). In this case, being 15 mm long monoliths cut in 3X5 mm long sections, the higher nano-particles surfaces density is at the initial or terminal sections (sections 1 or 5) while the central section (sections 2 or 3) appears slightly less populated.

This difference in density is possibly due to the fact that the free radical polymerization is faster than the nano-particles sedimentation, i.e. the nano-particles remain in a stable position during the formation of the porous polymeric structure and only in a final consolidation phase of the casting process, some brush nano-particles can slightly migrate from the monolith center to its periphery due secondary changes (excess of porogens in a monomers depleted part of the system) in the solubility of the components of the system at the end of the monolith formation. The hydrophilicity of the poly (methacrylic acid) brush arguably plays as well a role in the fact that the used nano-particles, at the end of this process, are quantitatively on the monolith surface and not embedded in its inner bulk structure.

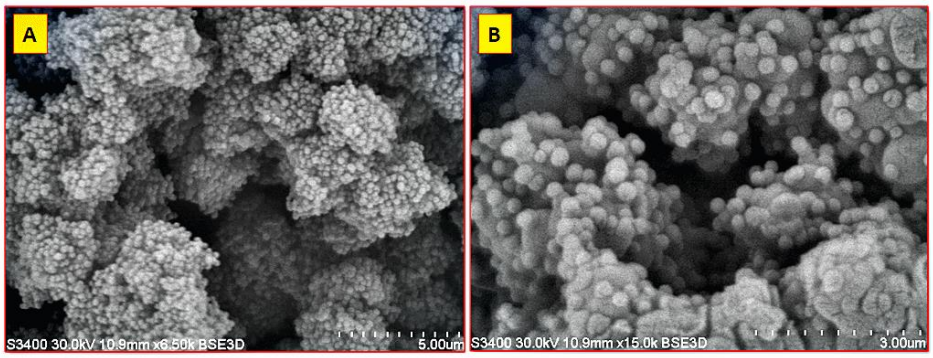

Figure 5.10: SEM images on the systems of monolith from the encapsulation approach. Inset A: section 1 or 5 (scale 5.00 µm). Inset B: section 2 or 3 (scale 3.00 µm). Each 15 mm monolith has been cut in 5X3 mm long sections.

The stability of the nano-particles/monolith surface interactions is similar to the previous electrostatic approach as shown in Table 5.2. Monoliths prepared without the addition of the grinded ammonium modified monolith (see 4th column, Table 5.2) display a much higher total weight loss (ca. 20 %) upon flushing with buffer solutions providing evidence for the importance of the added grinded ammonium modified EDMA-co-GMA monolith and its consequent electrostatic trapping effect.

Table 5.2: A nano-encapsulated monolith (dried 5 days at 0.1 mBar, RT and weighed) (see material 3, Inset B, Figure 5.4) is flushed with the solutions of different pH (dried, 5 days at 0.01 mBar, RT). The flow rate is of 2000 µL/h. PBS is a phosphate buffer saline solution used typically for most proteins, pH=7.4.

Solution flushed	Weight loss (%), 10 ml flushed	Weight loss (%), 100 ml flushed	Weight loss (%) without grinded monolith used, 10 mL	pH
0.1 M PBS	**1**	**3**	**20**	**7.4**
HCl	**1**	**2**	**22**	**4.5**
HCl	**1**	**3**	**18**	**6**
NaOH	**2**	**4**	**21**	**8**
NaOH	**3**	**4**	**23**	**9.5**

Figure 5.11-12 show SEM images of the post flushed nano-encapsulated monoliths obtained with and without addition of grinded ammonium modified monolith respectively. Figure 5.12 shows a very low number of brush nano-particles in particular on the more exposed and interstices-free surfaces. This is in agreement with the weight loss date presented in Table 5.2 and further highlights the importance of the addition of the ammonium modified monolith.

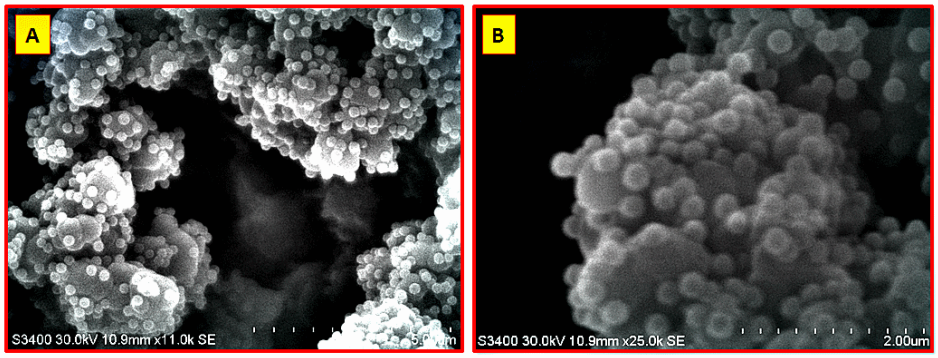

Figure 5.11: Nano-encapsulated monoliths. Inset A (scale 5.00 nm): monolith washed with 100 mL HCl pH=4.5 (see Table 5.2) (section 3 of 5); Inset B (scale 2.00 nm): monolith washed with 100 mL NaOH pH=9.5 (see Table 5.2) (section 3 of 5). Each 15 mm monolith has been cut in 5X3 mm long sections.

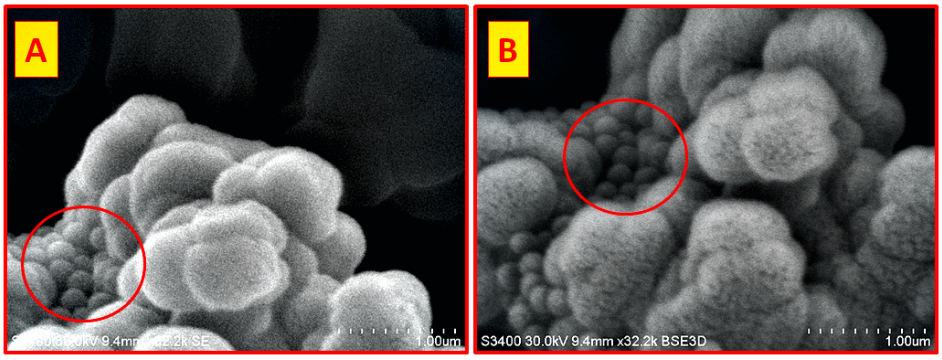

Figure 5.12: SEM micrographs of samples from monoliths done by an encapsulation approach without addition of grinded ammonium modified EDMA-co-GMA monolith. Inset A (scale 1 nm): monolith washed with 10 mL HCl pH=4.5 (see Table 5.2, 5th column) (section 3 of 5): Inset B (scale 1 nm): monolith washed with 10 mL NaOH pH=9.5 (see Table 5.2, 5th column) (section 4 of 5). Both the systems are substantially nano-particles depleted; the red circles indicate zones where the only trapping forces are arguably of frictional nature. Each 15 mm monolith has been cut in 5X3 mm long sections.

5.1.4 Monolith surface decoration with carboxylic acid functions by click chemistry approach

In order to form a comparison material able to show the brush enhancement factor expected from the material 3 in Figure 5.4, Inset B, the bare EDMA-co-GMA monolith is chemically modified at its surface with carboxylic functions. Indeed, in this way, two materials exposing the same chemical groups are compared. On one hand, a porous monolith with a nano-brushed poly (methacrylic acid) surface, on the other hand, a porous monolith with a carboxylic acid covered surface. In Figure 5.13 the reaction sequence used to form the system 5 is detailed.

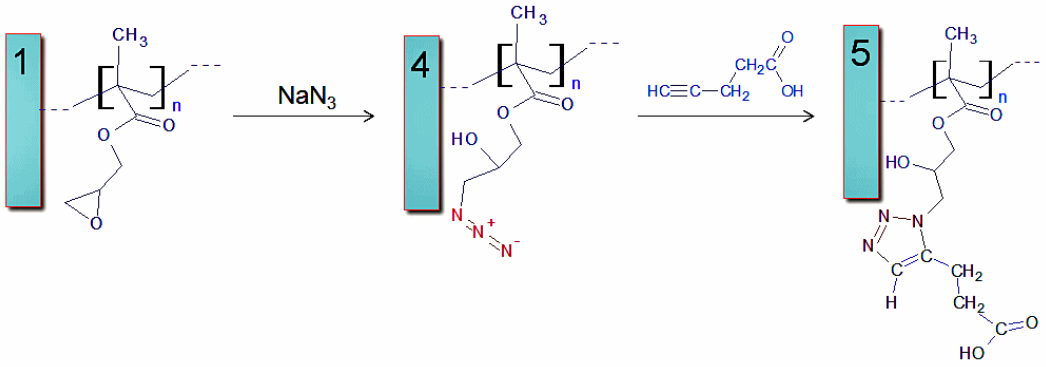

Figure 5.13: Formation of carboxy-modified monolith (see material 5) by click chemistry: The two step click-chemistry approach is here used to form the material 5 used as reference for the material 3, Inset B, Figure 5.4.

In Figure 5.14 there is the comparison of the ATR-IR spectra before (see material 1, Figure 5.13) and after (see material 4, Figure 5.13) the reaction with the sodium azide. The azido signal at 2100 cm^{-1} (see Figure 5.14, Inset B, peak b.1) at the end of the reaction is clearly visible. The second step of the sequence is a classic click reaction. In this case, a suspension of Copper(I) iodide (CuI) and N,N,N',N'',N''-pentam-ethyl-diethylene-triamine (PMDETA) is used as catalytic system. The experimental set up is similar the just described dynamic approach (see Figure 5.5) but, to prevent any abrasion of the porous monolith surface, a low reactants flow rate (500 µL/hour) was applied.

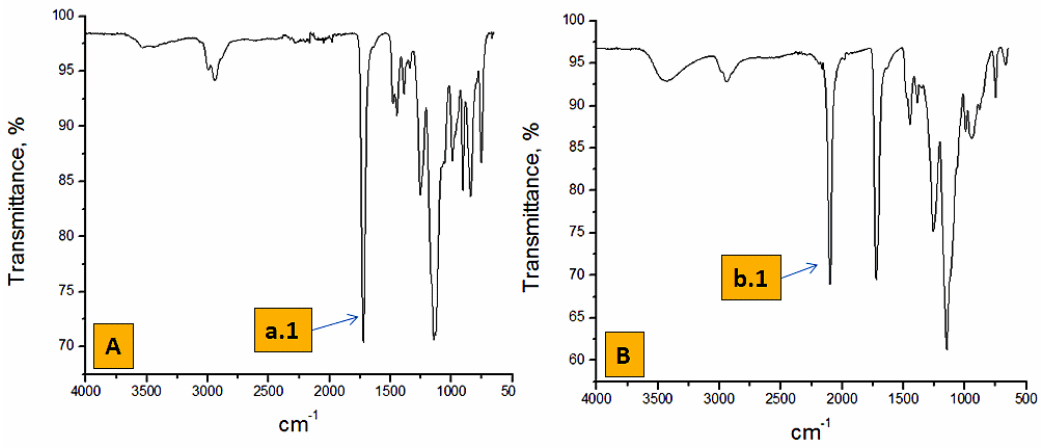

Figure 5.14: ATR-IR spectra of bare EDMA-co-GMA monolith (see material 1, Figure 5.13) before (Inset A; carbonyl signal at 1730 cm^{-1}; peak a.1) and after reaction with sodium azide, (Inset B; azido signal at 2100 cm^{-1}; peak b.1).

In Figure 5.15 there is the direct comparison of the azido peak at 2100 cm^{-1} before and after reaction. The reaction has been performed on three identical monoliths under identical conditions and it was found that after three days no further reaction occurred. From the IR spectra a maximum yield of ca. 70 % can be estimated (Integration of the peak areas using Origin 8.5®). This is probably due to steric hindrance on the monolith surface.

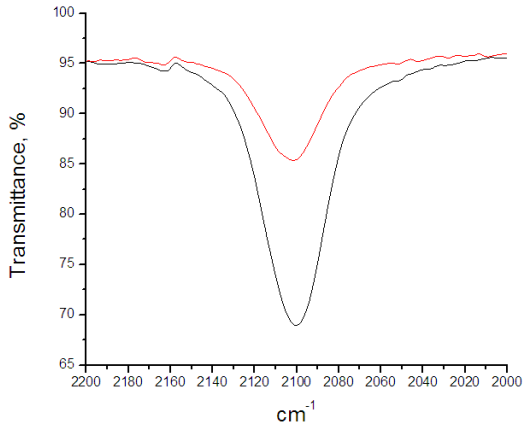

Figure 5.15: Black line: ATR-IR peak at 2100 cm-1 (azido signal; see peak b.1, Figure 5.14) of the azido treated EDMA-co-GMA monolith. Red line: the ATR-IR peak at 2100 cm-1 (azido signal) of the EDMA-co-GMA monolith after click reaction lasting three days.

5.2 Comparison of extraction capacity of functional monoliths

The description of the decoration process and its geometrical aspects on one hand (see the paragraph 5.1.1) and the discussion about the monolith chemical modifications on the other hand (see the paragraphs 5.1.2-4), naturally drive the attention on the central point of this paragraph: The measure of the brush enhancement effect during solid phase extractions.

In this study, four specific SPE tests are considered. Each of the two selected analytes of interest is tested, one at a time, on two EDMA-co-GMA derived monoliths. The reasons for choosing these materials are clarified in the following.

The nano-brushed monolith (see material 3, Inset B, Figure 5.4), featuring the carboxylic groups in the poly(methacrylic acid) brush and the surface carboxy-decorated monolith (see material 5 in Figure 5.13) are the two SPE devices here considered. Based on the substantial equivalence of the chemical groups involved in the materials 3 and 5, the extraction processes will be ruled by the same kind of analyte-solid phase interactions and the eventual extraction performance enhancement, due to the presence of the electrostatically trapped nano-brush on the monolith surface of the material 3, will be easily determined by direct comparison with material 5. This comparison, of course, relies on the proven stability of the cooperative nano-brush/monolith electrostatic interactions of the material 3 who can withstand the presence of charged species, as the data from Table 5.1-2 implies, without expulsion of brushed nano-particles being the pH ranging from 4.5 to 9.5.

Myoglobin and Blue Dextran are the analytes specifically used in this study. The rationale for the use of these two analytes is based on the fact that while they have a large mass difference (Myoglobin 16,951 Da; Blue Dextran 2,000,000 Da), their iso-electric points are very close (Myoglobin, pI=7.2[42]; Blue Dextran, pI=7.1[43]). On this premises, the nature of the analytes-solid phase interactions (typically electrostatic and permanent/induced dipole-dipole interactions) is directly linked to the mass of

the analyte if the same buffer solution (i.e., the same pH) is used during the extractions. The smaller Myoglobin, with weaker solid phase interactions, will tend to be less strongly retained in the extraction device with respect to the bigger Blue Dextran, which will be more strongly retained. The evaluation of the brush enhancement factor will be derived by the comparison of the data obtained from the two kinds of monoliths. Indeed, these selected "standard" analytes are expected to have a significantly different behavior during extractions involving materials 3 and 5 if the presence of the polymeric nano-brushes impacts the analyte-solid phase interactions.

An analysis of the theoretical principles ruling the SPE would be out of the scope of this discussion and here only the definitions and the laws used to cast the final conclusions will be detailed. The theoretical principles ruling liquid chromatography are applicable for the description of the SPE processes and commonly used to develop methods in this field.[44-48] The data-derived extraction parameters, breakthrough volume (V_B), number of theoretical plates (N), the retention factor (k) and the recovery (r), will be here used to quantify the analytes-solid phase interactions.

- The breakthrough volume (V_B), for a given analyte at known concentration and extraction flux conditions, is defined as maximum sample volume which can be loaded in the extraction tool without loss of the analytes.[49] The higher the V_B is, the higher will be the biggest possible concentration of the sample in the SPE tool.
- The concept of theoretical plate (N) was historically born in the context of the theory of distillation.[50] Indeed, a rectification column used during some distillation processes is formed by a number of adjacent superimposed and interconnected chambers where, while the system is boiling, in each chamber the condensed falling liquid film equilibrates with its ascendant vapors. Due the equilibration between the liquid phase and the gas phase (Raoult's law, Dalton's law, and Henry's law are currently used to describe these interactions), each chamber (or plate) host a vapor richer in compound with lower boiling point if compared to the directly inferior chamber. A distillation

column with a higher number of plates would be able to distillate and separate two liquids featuring closer boiling points. A modified concept of plates, used for the general theory of the liquid chromatography as well, is also used in the SPE context. A theoretical plate is the smallest imaginary portion (disk) of monolith allowing equilibration of the analytes between the solid phase and liquid phase. In the specific case of the systems under study, the solid phase is the buffer conditioned monolith surface of the materials 3 and 5 and the liquid phase is the flushed buffer solution. Myoglobin and Blue Dextran in the flowing solution will participate to equilibria between these two phases during the extraction process. The number N, in the specific SPE context, is important to define as it quantifies how the extraction would be able to purify and/or concentrate a complex matrix. A higher N, SPE can separate more complex analytical matrixes.

- The retention factor (k) is the ratio of the amount of moles of analyte adsorbed in the solid phase and the amount of mole present in the mobile phase. A SPE featuring a bigger retention factor implies stronger interactions with the solid phase.[51]
- The recovery (r) is the amount of the analyte that can be recovered after the SPE and it is expressed as the percent of analyte amount in the starting sample.[52]

The analyte-solid phase interactions are the element under discussion and, for these reasons, four distinct SPE tests are here discussed along with the relative extraction parameters (V_B, N, k and r). The experimental data of these four extractions allows defining four respective breakthrough curves (BCs). During the extraction process, the concentration of the analyte in the effluent can be measured by UV spectroscopy. The dependence between the concentration of the analyte in the effluent at the monolith outlet and the volume of the sample passed through the monolith gives the BC curve.[53]

Specifically, four buffer pre-conditioned monoliths (see details in the experimental section), two for material 3 and two for the material 5, are separately flushed with Myoglobin or Blue Dextran standard solutions at the known concentrations C_0(M)

and C_0(BD) respectively. For each of the four SPE tests, a set of 50 effluent samples (each with a volume of 0.5 mL) is collected, diluted and the respective absorbance values are read at λ_{MAX}= 409 nm for Myoglobin or λ_{MAX}= 619 nm for Blue Dextran. Each UV derived value is then normalized dividing by the respective absorbance of the Myoglobin or the Blue Dextran standard solutions at the pertinent λ_{MAX}. The best mathematical function used to fit the experimental data is the Boltzmann curve.[54] A_1, A_2, x_0 and dx is the set of the four regression parameters pertinent to each BC curve.

In Figure 5.16 there is a theoretical example of BC curve. The values of V_B, V_R and V_E from the statistically derived curves ideally divide the curve in three zones. From V=0 to V=V_B, the analyte is quantitatively trapped in the monolith, from V=V_E to bigger volumes, the analyte is not absorbed at all as the monolith has reached the saturation conditions and the analyte concentration at the monolith inlet (in this study, C_0(M) or C_0(BD)) is the same as at the monolith outlet. The zone between V= V_B and V=V_E feature the retention volume V_R where the outlet concentration is at 50 % of the inlet analyte concentration.

The whole upper area of the curve in Figure 5.16 represents the maximum sample load for each specific SPE test. The V_B, V_R and V_E values and the measured void volume V_M (the volume of the solvent inside the monoliths during the extractions; see experimental part for the details), are used to calculate the four values of interest in this study: V_B, N, k and r. The Table 5.3 briefly details the formulae used in this study.

Table 5.4 shows the normalized experimental data pertinent to the four SPE tests performed in this study: SPE 1, 2, 3 and 4. Table 5.5 shows the regression parameters for the four sets of experimental data: the reduced R^2 close to 1 (see Origin 8.5 Fit sigmoidal help file), and the close to zero chi-square values confirm the quality of the fit under the variance null hypothesis (data ruled by Gaussian distribution) being the four fit curves depicted in Figure 5.17 (Inset A for system 5 SPEs, Inset B for system 3 SPEs).

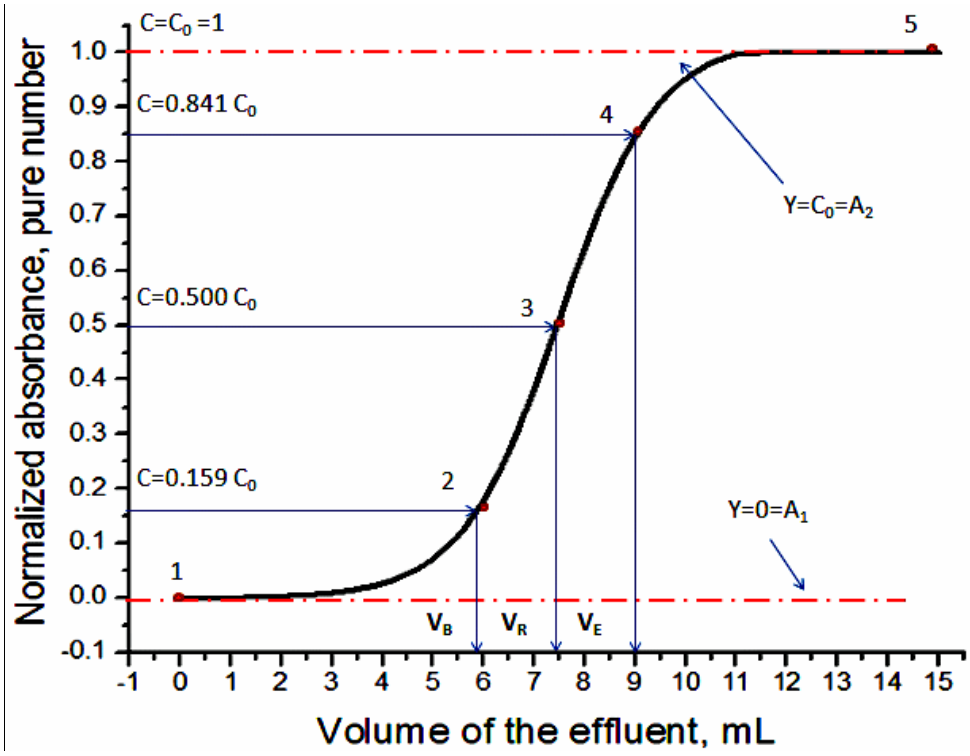

Figure 5.16: Example of a Boltzmann curve used to fit the experimental data; a solution of the analyte of interest at concentration C_0 is flushed in the buffer conditioned monolith and constant volume effluent samples are collected (e.g., 0.5 mL each). The x scale represents the cumulative volume of the effluent in mL. Each sample is UV scanned after being diluted (using the same dilution factor for all the effluent fractions): each respective absorbance value at a λ_{MAX} for the specific analyte of interest is divided by the absorbance at the same λ_{MAX} of the solution used for the extraction (diluted under the same conditions of the samples) (this is the normalization respect to C_0). The sample dilution is aimed at working in the linear spectrometer conditions (to read absorbance values between 0.2 and 1.0). The values V_B, V_R and V_E, are derived from the curve at y=0.159, 0.500 and 0.841 respectively corresponding to the points 2, 3 and 4 on the curve. A_1 and A_2 are parameters deriving from the statistical fit.

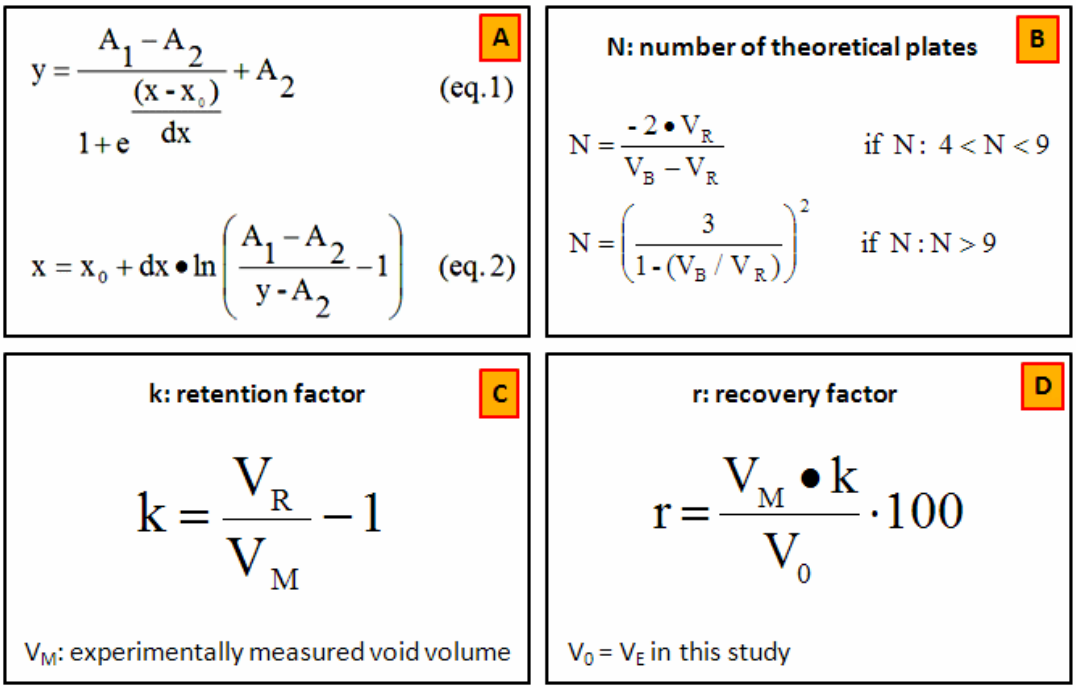

Table 5.3: Inset A: the Boltzmann function and its four parameters A_1, A_2, x_0, xd (eq. 1); the re-arranged Boltzmann equation in the eq. 1, to calculate points on the x scale (to determine for example the values V_B, V_R and V_E as detailed in Figure 5.16) in correspondence of y values of interest. Inset B: the formulae for the determination of the number of theoretical plates N (see reference 53). Inset C: the determination of the retention factor k; for the determination of the void volume of the SPE monoliths, see the experimental part.[55] Inset D: the formula for the determination of the retention factor. In this study, the total SPE volume V_0 is in each test equal to the V_E value pertinent to each process being the residual volume (25 –V_E mL) of course not considered to determine the recovery factor.

The nano-brushed surface has a strong impact on the analytical SPE performances as can be visually seen from the Figure 5.17. As anticipated at the start of this paragraph, the retention volumes (V_R in correspondence of y=0.5) for both the analytes of the nano-brushed monolith SPEs (system 3, Inset B, Figure 5.4) increase if compared to the case of the just surface decorated monolith (system 5, Figure 5.13). Indeed, V_R for Myoglobin in the SPE 1 is bigger if compared to for Myoglobin in the SPE 2 (see Figure 5.17) and the same considerations apply in the case of Blue Dextran and SPE 3 and 4. Moreover, it can be noticed how the retention volumes pertinent to this couple of analytes for the system 3 are more spaced-out if compared to the system 5.

Table 5.4: Normalized UV data for the 4 sets of samples. 50 samples (V=0.5 mL each) are collected at the monoliths outlet being the Myoglobin (pink columns) or the Blue Dextran (blue columns) standard solutions flushed. Experiment SPE1: Material 5 tested on Myoglobin solution. Experiment SPE2: Material 3 tested on Myoglobin solution. Experiment SPE3: Material 5 tested on Blue Dextran. Experiment SPE4: Material 3 tested on Blue Dextran solution. l_{MAX}=409 nm for Myoglobin; l_{MAX}=619 nm for Blue Dextran; C0(M) =C0(BD)= 2 mg/mL. Myoglobin UV sample dilution factor: 1/20 V/V. Blue Dextran UV sample dilution factor: ½ V/V. Dilutions, monoliths conditioning and UV blank are in 0.1 M Phosphate Buffer Saline solution, pH=7.40. The final values of 25 mL have been used as a prudential value in common for all the four SPE.

Sample number	mL	Material 5 (SPE 1)	Material 3 (SPE 2)	Material 5 (SPE 3)	Material 3 (SPE 4)	Sample number	mL	Material 5 (SPE 1)	Material 3 (SPE 2)	Material 5 (SPE 3)	Material 3 (SPE 4)
1	0.500	0.092	0.022	0.041	0.001	**26**	13.000	1.000	1.000	1.000	0.999
2	1.000	0.049	0.094	0.061	0.001	**27**	13.500	1.000	1.000	1.000	1.000
3	1.500	0.302	0.060	0.051	0.003	**28**	14.000	1.000	1.000	1.000	1.000
4	2.000	0.679	0.050	0.004	0.003	**29**	14.500	1.000	1.000	1.000	1.000
5	2.500	0.987	0.095	0.343	0.005	**30**	15.000	1.000	1.000	1.000	1.000
6	3.000	0.997	0.011	0.605	0.006	**31**	15.500	1.000	1.000	1.000	1.000
7	3.500	0.998	0.043	0.954	0.005	**32**	16.000	1.000	1.000	1.000	1.000
8	4.000	0.999	0.082	0.999	0.006	**33**	16.500	1.000	1.000	1.000	1.000
9	4.500	1.000	0.309	1.000	0.007	**34**	17.000	1.000	1.000	1.000	1.000
10	5.000	1.000	0.663	1.000	0.009	**35**	17.500	1.000	1.000	1.000	1.000
11	5.500	1.000	0.921	1.000	0.010	**36**	18.000	1.000	1.000	1.000	1.000
12	6.000	1.000	0.989	1.000	0.009	**37**	18.500	1.000	1.000	1.000	1.000
13	6.500	1.000	0.999	1.000	0.009	**38**	19.000	1.000	1.000	1.000	1.000
14	7.000	1.000	1.000	1.000	0.008	**39**	19.500	1.000	1.000	1.000	1.000
15	7.500	1.000	1.000	1.000	0.006	**40**	20.000	1.000	1.000	1.000	1.000
16	8.000	1.000	1.000	1.000	0.010	**41**	20.500	1.000	1.000	1.000	1.000
17	8.500	1.000	1.000	1.000	0.009	**42**	21.000	1.000	1.000	1.000	1.000
18	9.000	1.000	1.000	1.000	0.011	**43**	21.500	1.000	1.000	1.000	1.000
19	9.500	1.000	1.000	1.000	0.012	**44**	22.000	1.000	1.000	1.000	1.000
20	10.000	1.000	1.000	1.000	0.015	**45**	22.500	1.000	1.000	1.000	1.000
21	10.500	1.000	1.000	1.000	0.047	**46**	23.000	1.000	1.000	1.000	1.000
22	11.000	1.000	1.000	1.000	0.361	**47**	23.500	1.000	1.000	1.000	1.000
23	11.500	1.000	1.000	1.000	0.686	**48**	24.000	1.000	1.000	1.000	1.000
24	12.000	1.000	1.000	1.000	0.966	**49**	24.500	1.000	1.000	1.000	1.000
25	12.500	1.000	1.000	1.000	0.998	**50**	25.000	1.000	1.000	1.000	1.000

Table 5.5: Regression parameters A_1, A_2, x_0 and dx for the SPE 1, 2, 3 and 4 SPE tests. From the regression curves it is possible to calculate the values of V_B, V_R and V_E , in correspondence of y= y=0.159, 0.500 and 0.841 respectively (see Inset A, eq. 2, Table 5.3).

Test		Value	Standard Error	Reduced Chi-Square	Adjusted R-Square
SPE 1	A1	0.00806	0.01478	1.55E-04	0.9964
	A2	1.00092	0.00187		
	x_0	1.73946	0.01974		
	dx	0.34482	0.01545		
SPE 2	A1	0.03104	0.00656	3.06E-04	0.99768
	A2	1.00048	0.00280		
	x_0	4.75145	0.01709		
	dx	0.26061	0.01427		
SPE 3	A1	0.03621	0.01133	3.51E-04	0.99524
	A2	1.00058	0.00287		
	x_0	2.73857	0.02176		
	dx	0.30786	0.01841		
SPE 4	A1	0.00581	0.00176	6.08E-05	0.99974
	A2	1.00109	0.00154		
	x_0	11.22856	0.00800		
	dx	0.31920	0.00693		

Table 5.6: The V_B, V_R and V_E values derived from the regression curve (see Inset A, eq. 2, Table 5.3). Using these three values and the formulae in Table 5.4, the N (see Table 5.4, Inset B), k (see Table 5.4, Inset C) and r (see Table 5.4, Inset D) values are calculated. The monoliths void volumes (see experimental part for details) V_M are used as well. The V_B, N, k and r values on each line (SPE 1, 2 for Myoglobin and SPE 3, 4 for Blue Dextran) are used to calculate the brush enhancement factors as in Table 5.7.

	Test	V_B	V_R	V_E	N	k	r
Myoglobin	**SPE 1**	**1.147**	1.733	2.309	**5.911**	**4.9110**	**52.568**
	SPE 2	**4.261**	4.734	5.175	**528.014**	**527.0136**	**79.804**
Blue Dextran	**SPE 3**	**2.146**	2.715	3.237	**120.417**	**119.4166**	**65.749**
	SPE 4	**10.685**	11.224	11.756	**2289.214**	**2288.2135**	**88.629**

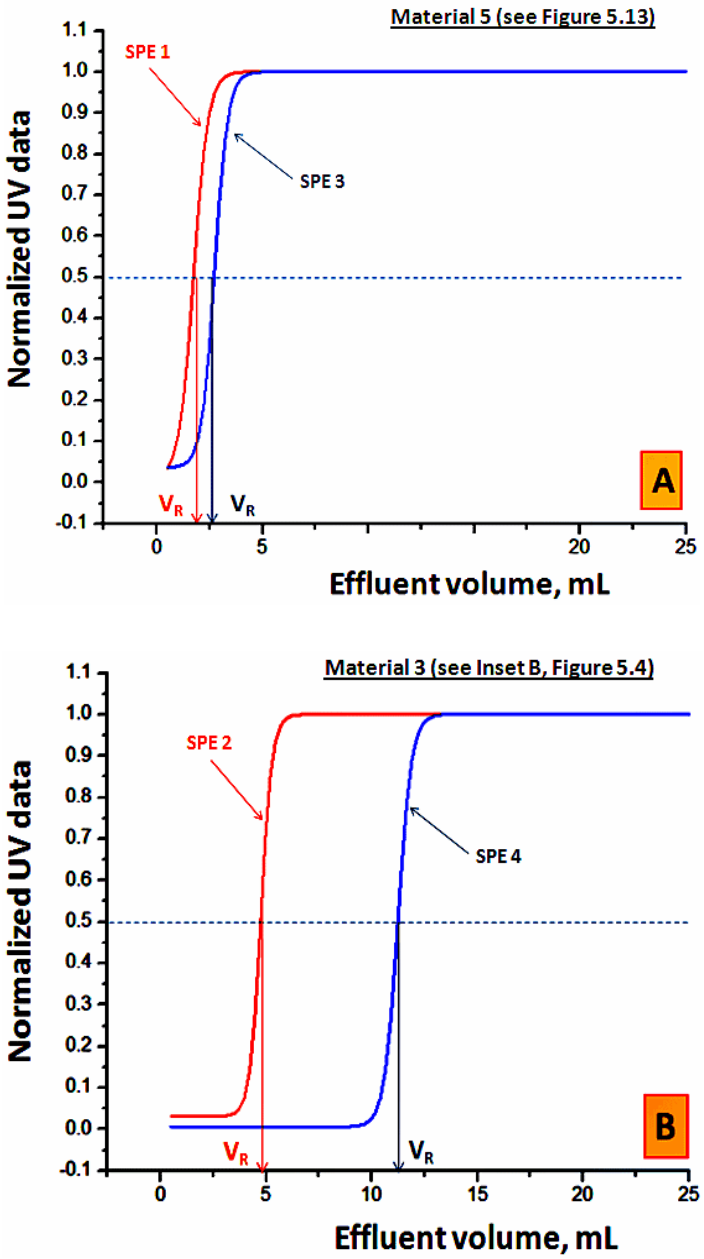

Figure 5.17: Inset A: The best fit curves for the SPEs performed using the Myoglobin (in red) and the Blue Dextran (in blue) for the system 5 (see Figure 5.13). Inset B: The best fit curves for the SPEs performed using the Myoglobin (in red) and the Blue Dextran (in blue) for the system 3 (see Inset B, Figure 5.4). The direct visual comparison on Inset A and B allows to see the effect of the nano-brushed monolith (see Inset B) on the V_R (x values corresponding to y=0.5). Indeed, for Myoglobin V_R for the test SPE2 is bigger than the V_R for the test SPE1 and, accordingly, for Blue Dextran V_R for the test SPE4 is bigger than the V_R for the test SPE3. The beneficial impact of the brushed nano-surface have now been proved and quantified.

The brush enhancement factor (BEF) for each of the SPE parameters (V_B, N, k and r) pertinent to Myoglobin and Blue Dextran can be numerically expressed as ratio

$$\mathrm{BEF} = \frac{\text{SPE parameter, System 3}}{\text{SPE parameter, System 5}},$$

as the Table 5.7 shows.

Table 5.7: The brush enhancement effects of the four SPEs studied parameters. Each value in this table is the ratio of the respective parameters in the Table 5.6 for brushed/not brushed monoliths (Material 3/Material 5).

	V_R	N	k	r
Myoglobin	**3.72**	**89.33**	**107.31**	**1.52**
Blue Dextran	**4.98**	**19.01**	**19.16**	**1.35**

The data in Table 5.7 shows the impressive impact of the nano-brushed surface on the SPE relatively to all the four studied parameters. For the first time, it is possible to see how this enhancement effect is not linear but more pronounced for smaller Myoglobin (see, for example, the 89.33 times increment in the value of N) being less pronounced for the bigger Blue Dextran (see, for example, the 19 times increment in the value N). A similar consideration applies to the retention factor k. This data is perfectly coherent with the systems under study: the minimum radius of the sphere containing Myoglobin is ~ 25 nm[56] and this value must be compared to the 40 nm brush thickness. The comparison of these two values indicates that the globular protein Myoglobin can be totally brush embedded and so it is possible to argue that the brush enhancement effect is maximized. The same it is not true for the bigger (and not globular) Blue Dextran where the minimum radius of the containing sphere is ~ 125 nm.[56]

As a concluding remark, it is interesting to position these calculated SPE performances in the more general SPE performances landscape. The SPE technique was developed as an ancillary sample pre-treatment step for concentration and cleaning of complex matrices to be used in HPLC or mass spectrometry tools. Even the more evolved commercial versions typically features N values from 5 to 20 depending on the analyte, complexity of the starting sample and SPE elution conditions.[57] In this new simple, cheap and easy to manufacture device, the

increment of the number of theoretical plates increases 20 to 90 times these values while exhibiting a better recovery of the analyte.

5.3 Conclusions

Detailed and robust protocols for the nano-brushed surface decorated EDMA-co-GMA porous polymeric monoliths are presented. In particular a new modified approach for the encapsulation approach is used to mold the monolith. The all-in-one molding approach produces polymeric porous monoliths with stable electrostatically trapped brush nano-particles. The positive influence of the nano-brush decoration on the extraction performances (the brush enhancement factor) is introduced from geometrical considerations and then measured. A new versatile, cheap and powerful solid extraction tool is described.

5.4 Experimental procedures

Materials

Raw Materials: Trimethylamine hydrochloride, 98%; Sodium azide, *ReagentPlus*®, ≥99.5%, sodium nitrite, ACS reagent, ≥97.0%; sulphuric acid, ACS reagent, 95.0-98.0%; 4-pentynoic acid, 95%; copper (I) iodide, 99.999% trace metals basis ; *N*,*N*,*N'*,*N''*,*N''*-Pentamethyldiethylenetriamine (PMDETA), 99%; Sodium hydroxide BioXtra, ≥98% (acidimetric), pellets (anhydrous); Hydrochloric acid 36.5-38.0%, BioReagent, for molecular biology ; *N,N*-Dimethylformamide anhydrous (DMF) , 99.8%; Phosphate buffered saline (BPS), tablet: One tablet, dissolved in 200 mL of deionized water, yields 0.01 M phosphate buffer, 0.0027 M potassium chloride and 0.137 M sodium chloride, pH 7.4, at 25 °C. All chemicals were purchased from Sigma-Aldrich and used without any further purification unless otherwise stated.

In-home prepared materials: Brush poly (MAA) core FITC silica nano-particles from the same batch of the Sample No. 4, Table 3.1 Chapter 3 (De-protected version); Standard Bare poly (EDMA-co-GMA) polymeric monolith as described in Chapter 4.

Methods

A Perkin-Elmer Spectrum 100 was used for collecting attenuated total reflectance Fourier transform infrared (ATR-FTIR) spectra in the spectral region of 650–4000 cm^{-1}. The spectra were obtained from 2064 scans with a resolution of 2 cm^{-1}. A background measurement was taken before the sample was loaded onto the ATR unit for measurements. Spectrometric studies were carried out using a Perkin-Elmer Lambda 900 spectrometer (Foss, Ireland), Euthech Instruments PH510 pH meter, Hitachi S3400n SEM microscope, World Precision Instruments (WPI) SP120PZ syringe pump for laboratory use.

Preparation of the tetra-methyl-ammonium modified EDMA-co-GMA monolith (material 2, Inset B, Figure 5.4) by static and dynamic approach

Static approach: A poly (EDMA-co-GM) porous polymeric monolith (Length 1.5 cm) (see in-home prepared material section in Material paragraph of this Chapter) is washed with distilled water (Volume used: 5 mL) using a 1 mL plastic syringe and a syringe pump (Flow rate: 2500 µL/hour). A solution of trimethylamine hydrochloride TMA HCl (0.5 g, 5.23 10^{-3} mol) in iPrOH/water 20/1 wt/wt (5 mL) (solution A) is pumped through the monolith using a 1 mL plastic syringe and a syringe pump (Flow rate: 2000 µL/hour) and the eluates are discarded. The so formed reactant filled monolith is then Teflon tape sealed and left standing in a beaker in an oven at 100 °C during 24 hours. The system is then, at RT and once free of its seals, washed with distilled water (Volume used: 15 mL) using a 1 mL plastic syringe and a syringe pump (Flow rate: 2000 µL/hour). The last mL of eluate is monitored to see if it has a neutral pH. The system is left 3 days in a vacuum desiccator then the cartridge is stored in a sealed N_2 purged vial at RT. The dynamic approach is performed by flushing the solution A at a flow rate of 500 µL/ hour. No other parameter is changed referred to the static approach.

Preparation of the azido modified EDMA-co-GMA monolith (see material 4, Figure 5.13) under static and dynamic reaction conditions

A poly (EDMA-co-GMA) porous polymeric monolith (Length 1.5 cm) is washed with distilled water (Volume used: 5 mL) using a 1 mL plastic syringe and a syringe pump (Flow rate: 2500 µL/hour). A 5 mL EtOH/Water 10/1 V/V solution of sodium azide (0.136 g, 2.096 10^{-3} mol) and ammonium chloride (0.026 g, 4.82 10^{-4} mol, used as a reaction catalyst) is flushed trough the monolith using a 1 mL plastic syringe and a syringe pump (Flow rate: 2000 µL/hour) and the eluates are collected in a recovery flask. The Teflon tape sealed cartridge is then placed in an open vial and left in an oil bath at 110 °C during 3 days under an efficient fume hood . The system is then, at RT and once free of its seals, washed with distilled water (Volume used: 15 mL) using a 1 mL plastic syringe and a syringe pump (Flow rate: 2500 µL/hour) being the exhaust solution collected in a recovery flask. The system is left 3 days in a vacuum desiccators then the cartridge is stored in a sealed N_2 purged vial at RT. The dynamic approach is performed by flushing the same solution (EtOH/Water 10/1 V/V solution sodium azide (0.136 g, 2.096 10^{-3} mol) and ammonium chloride (0.026 g, 4.82 10^{-4} mol) using a 1 mL plastic syringe and a syringe pump (Flow rate: 2000 µL/hour) and no other parameter is modified.

Sodium azide treatment: the sodium azide residual/exhaust solutions collected during this synthesis, are water diluted at 5% NaN_3 wt/wt are put into a three-necked flask equipped with a stirrer, a dropping funnel, and an outlet with plastic tubing to carry nitrogen oxides to the laboratory chemical fume hood. A 20% aqueous solution of sodium nitrite containing 1.5 g (about 40% excess) of sodium nitrite per gram of sodium azide is added with stirring. A 20% aqueous solution of sulphuric acid is then added gradually until the reaction mixture is acidic to pH paper. The chemical reactions involved are:

$$2\ NaNO_2\ (l) + H_2SO_4\ (l) \rightarrow 2\ HNO_2 + Na_2SO_4$$

$$2\ NaN_3\ (l) + 2\ HNO_2 \rightarrow 3\ N_2\ (g) + 2\ NO\ (g) + 2\ NaOH\ (l)$$

This order of addition is essential. If the acid is added before the nitrite, poisonous volatile HN_3 will be evolved.) When the evolution of nitrogen oxides is over, the acidic solution is tested with starch-iodide paper; if it turns blue, an excess nitrite is present and decomposition is complete. The reaction mixture can safely be washed down the drain. Note that the solution must be neutralized with dilute NaOH solution to pH 6-

9 prior to discharge. This simple, safe and green approach to the sodium azide residuals treatment is adopted to avoid accumulation of potentially dangerous sodium azide residual solution in the laboratory.

Preparation of the carboxyl modified EDMA-co-GMA monolith by click chemistry (see material 5, Figure 5.13) under static and dynamic reaction conditions

A suspension in DMF (5 mL) of 4-pentynoic acid (0.174 g, 1.77 10^{-3} mol), CuI (61 mg, 3.20 10^{-4} mol), PMDETA (1 mL, 0.83 g, 4.79 10^{-3} mol) (suspension A) is magnetically stirred in a rubber septum sealed vial during 15 min. N_2 bubbling (a purge outlet needle is connected to a Dreschel bottle filled with mineral oil (h=10cm)). In an AtmosBag properly modified to host a syringe pump, a poly(EDMA-co-GMA) porous polymeric monolith (Length 1.5 cm) is washed with N_2 purged (15 min.) distilled water (Volume used: 5 mL) using a 1 mL plastic syringe and a syringe pump (Flow rate: 500 µL/hour). Then the washed device is flushed using a 1 mL plastic syringe and a syringe pump (Flow rate: 500 µL/hour) with the suspension A. The system is Teflon tape sealed under N_2 in the AtmosBag. The sealed system is left at 85 °C during 3 days. The system is then, at RT and once free of its seals, washed with 7M NH_3 in MeOH (Volume used: 3 mL) using a 1 mL Teflon syringe and a syringe pump (Flow rate: 2000 µL/hour). Then washed with distilled water (Volume used: 15 mL), HCl 0.1 M (Volume used: 15 mL), distilled water (Volume used: 15 mL) using a 1 mL Teflon syringe and a syringe pump (Flow rate: 2000 µL/hour). The system is left 3 days in a vacuum desiccator then the cartridge is stored in a sealed N_2 purged vial at RT.

The equivalent dynamic approach is performed flushing the N_2 bubbled oxygen free suspension A in a washed monolith (using N_2 purged (15 min.) distilled water (Volume used: 5 mL) -Flow rate: 2000 µL/hour; the outlet tubing is left water flooded to avoid contact with air). The flow rate during the reaction is 500 µL/hour to avoid damaging the monolith surface. No other parameter is changed respect the static approach.

The electrostatic trapping technique (see material 3, Inset B, Figure 5.4)

100 mL of the milky yellowish suspension (0.5 mg/mL of brush poly (methacrylic acid) core FITC fluorescent silica nano-particles, diameter: 200 nm, brush thickness: 40 nm; see in-home prepared material section in Material paragraph of this Chapter) are prepared and flushed in a buffer pre-wetted 15 mm long ammonium modified poly (EDMA-co-GMA) monolith (10 mL of distilled water at 1000 µL/h using a syringe pump and a 1 mL syringe as syringes bigger in diameter would generate a lot of back pressure). Initially, 5 mL of this suspension are flushed at 1000 µL/h, then 70 mL are flushed at 2000 µL/h. Each 5 mL of flushed suspension, the flux direction is changed in order to have better decoration uniformity by plaguing the syringe alternatively at the monolith inlet/outlet. For the first 60 mL, the eluted is just clear colorless water then, the eluted suspension becomes cloudier. In this phase further 25 mL are flushed. The end of the process is signaled by the fact that the charged milky suspension and the eluted suspensions have the same cloudiness (in principle, the fluorescent intensity or the UV spectrum of an optically matched suspension of the effluents could be measured as well to monitor this saturation plateau). The 15 mm washed (15 mL distilled water) and dried nano-particles decorated monolith (5 days at RT, 0.010 mBar) shows a mass increment respect to the starting ammonium decorated monolith of 32 mg (15 tests gave the same numbers).

The encapsulation approach with details to prepare the bare EDMA-co-GMA porous polymeric monolith

The standard EDMA-co-GMA monolith manufacture as detailed in the Chapter 4 is the following.

In a glass vial are transferred Azobisisobutyronitrile (AIBN) (3 mg, 1.83 10^{-5} mol), water (70 mg, 3.88 10^{-3} mol), ethylene dimethacrylate (75 mg, 3.78 10^{-4} mol), glycidyl methacrylate (225 mg, 1.58 10^{-3} mol), 1-4 butanediol (280 mg, 3.11 10^{-3} mol), 1-propanol (350 mg, 5.82 10^{-3} mol). The vial is sealed with a rubber septum and well mixed by a vortexing table and N_2 is gently bubbled through the system (the vial is connected to a Dreschel bottle filled with mineral oil, h=15 cm) during 15 minutes. Then the PP tubes with Luer locks at the ends, the septum vial with the

monomers/porogens pool, 1 mL syringes to be used as stoppers are transferred inside an AtmosBag© and 3 cycles N_2 / Vacuum are applied. Then, the tubes are filled with the solution and sealed under inert atmosphere. The filled cartridges are left vertically standing in a oven at 70°C for 22 hours and then, at RT, washed with MeOH.

To the standard bare poly (EDMA–co-GMA) monolith mixture, are added brush nano-particles used in this study at a final batch concentration of 50 mg for a 15 mm long monolith. For a final blend volume of 10 mL, 210 mg of nano-particles are needed. The system is then ultra-sonicated for 5 min to form a stable dense suspension (stable for 2 hours without any detectable precipitation). Then, a previously prepared ammonium modified EDMA-co-GMA monolith is grinded to a fine powder and mixed to this suspension at 50 mg/mL. The system is ultra-sonicated for 5 minutes and the stable suspension is transferred to a sealed vial and gently nitrogen purged for 15 minutes. This oxygen free suspension is then transferred in the polypropylene housing (see Chapter 4) in nitrogen purged AtmosBag as for a classic bare monolith manufacture. This oxygen free suspension is then transferred in the polypropylene housing (see Chapter 4) in nitrogen purged AtmosBag as for a classic bare monolith manufacture. This is a very delicate stage as great care must take in order to avoid the presence of bubbles in the dense liquid mixture. After attaching syringes at both ends the mixture is moved back and forth a number of times to assure the absence of voids. Then the monolith is thermally cured as usual.

The solid phase extraction procedure

Monolith conditioning: 5 mL of 0.1M of phosphate buffer saline solution (PBS) at pH=7.4 are flushed trough the monolith at a flow rate of 1000 µL/hour

Sample flushing: For the Myoglobin: a solution in 0.1 M PBS at pH=7.4 (2mg/mL) is flushed at a flow rate of 1000 µL/hour; the same conditions apply to the Blue Dextran solutions.

Sample elution: a water solution of HCl (pH=5.4) is flushed at a flow rate of 1000 µL/hour. The Myoglobin is eluted flushing 1.6 mL while the Blue Dextran is eluted

flushing 2 mL (the elution completion is signaled by the absence of color inside the monoliths).

Note: the pH = 5.4 assure the compatibility of the specific proteic material used as per specifications from the vendor.

Experimental determination of the monoliths void volumes

The determination of the void volume V_M (the volume occupied by the liquid phase during the SPE), presents both theoretical and practical difficulties and it still remains an open question in the liquid chromatography field. [58] [59] [60]

In this study on SPE, the determination of the void volume is made by flushing ten previously dried system 3 and ten system 5 monoliths with distilled water over night (3 days at 0.05 mBar at RT) and tare weighted. The weight of the water full system is determined (extreme care is used in eliminating residual water in the free Luer Lock inner space). The difference in weight is expressed in mL (0.001 mL=1mg). In Table 5.5 there are the experimental results.

Table 5.8: the Void Volume determination for system 3 and 5

Sample No.	System 3, mg	System 5, mg
1	33.010	33.079
2	33.036	33.047
3	33.017	33.023
4	33.035	33.061
5	33.024	33.028
6	33.099	33.004
7	33.020	33.009
8	33.047	33.063
9	33.031	33.093
10	33.011	33.097
Mean	33.033	33.050
Standard deviation	0.026	0.034

The experimental results are not showing any substantial difference for the two systems and the void volume is assume to be 0.033 mL .[61]

5.6 References

[1] Chiang, C. K.; Chen, W. T.; Chang, H. T. *Chem. Soc. Rev.* **2011**, 40, 1269

[2] Lucena, R.; Sinomet, B. M.; Cardenas, S.; Valcarcel, M. *J. Chromatogr. A* **2011**, 1218, 620

[3] Jacobs, C. B.; Peairs, M. J.; Venton, B. J. *Anal. Chim. Acta* **2010**, 662, 105

[4] Agui, L.; Yanez-Sedeno, P.; Pingarron, J. M. *Anal. Chim. Acta* **2008**, 662, 11

[5] Wang, F.; Hu, S. S. *Microchim. Acta* **2009**, 165, 1

[6] Luo, X.; Morrin, A.; Killard, A. J.; Smith, M. R. *Electroanalysis* **2006**, 18, 319

[7] Huang, X.; Jain, P. K.; El-Sayed, I. H.; El-Sayed, M. A. *Nanomedicine* **2007**, 2, 681

[8] Beveridge, J. S.; Stephens, J. R.; Williams, M. E. *Annu. Rev. Anal. Chem.* **2011**, 4, 251

[9] Wu, C. S.; Lui, F. K.; Ko, F. H. *Anal. Bioanal. Chem*, **2011,** 399, 103

[10] Trojanowicz, M. *Trends Anal. Chem.* **2006**, 25, 480

[11] Scida, K.; Stege, P. W.; Haby, G.; Messina, G. A. *Anal. Chim. Acta* **2011**, 691, 6

[12] Connolly, D. ; Currivan, S.; Paull, B. *Proteomics* **2012**, 12, 2904

[13] Bandari, R.; Buchmeiser, M. R. *Catal. Sci. Technol.* **2012,** 2, 220

[14] Lui, D.; Lei, J. H.; Guo, L. P.; Yan, X. M. *J. Sol-Gel Sci. Technol.* **2008**, 46, 57

[15] Blomberg, L. *Anal. Bioanal. Chem*. **2009**, 393, 797

[16]Liu, J.; White, I.; De Voe, D. L. *Anal. Chem.* **2011,** 83, 2119

[17] Yao, K.; Yun, J.; Shen, S.; Wang, L. *J. Chromatogr. A* **2006,** 1109, 103

[18] Yao, K.; Yun, J.; Shen, S.; Wang, F. C. *Biochem. Eng. J.* **2007,** 36, 139

[19] Krenkova, J.; Foret, F. *J. Sep. Sci.* **2011**, 34, 2106

[20] Connolly, D.; Twamley, B.; Paull, B. *Chem. Commun.* **2010***,* 46, 2109

[21] Xu, Y.; Cao, Q.; Svec, F.; Frechet, J. M. *Anal. Chem.* **2010**, 82, 3352

[22] Lee, A.; Dubinsky, S.; Tumarkin, E.; Moulin, N. *Adv. Funct. Mater.* **2011**, 21, 1959

[23] Tobal, K.; Guerre, O.; Rolando, C.; Le Gac, S. *Mol. Cell. Proteomics* **2006**, 5, S278

[24] Hsieh, H. C.; Sheu, C.; Shi, F. K.; Li, D. T. *J. Chromatogr. A* **2007**, 1165, 128

[25] Xu, P.; Yao, Y.; Shen, S.; Yun, J. *Chin. J. Chem. Eng.* **2010**, 18, 667

[26] Krenkova, J.; Lacher, N.; Svec, F. *Anal. Chem.* **2010,** 82, 8335

[27] Li, Y.; Chen, Y.; Xiang, R.; Ciuparu, D. *Anal. Chem.* **2005**, 77, 1398

[28] Chambers, S. D.; Svec, F.; Frechet, J. M. J. *Anal. Chem.* **2011**, 83, 9478

[29] Chambers, S. D.; Holcombe, T. W.; Swec, F.; Frechet J. M. J. *Anal. Chem.* **2011**, 83, 9478

[30] Wang, M. M.; Yan, X. P. *Anal. Chem.* **2012**, 84, 39

[31] Hilder, E. F.; Svec, F.; Frechet, J. M. J. *J. Chromatogr. A* **2004,** 1053, 101

[32] Hutchiston, J. P.; Hilder, E. F.; Shellie, R. A.; Smith, J. A. *Analyst* **2006**, 131, 215

[33] Chambers, S. D.; Svec, F.; Frechet, J. M. J. *J. Chromatogr. A* **2011,** 1218, 2546

[34] Xu, Y.; Cao, Q.; Svec, F.; Frechet, J. M. J. *Anal. Chem.* **2010,** 82, 3352

[35] Mo, Y.; Turner, K. T.; Szulfarska, I. *Nature* **2009**, 457, 1116

[36] Svec, F.; Tennikova, T; Deyl, Z. *J. Chromatogr. Libr.*, Elseiver: Amsterdam, p 26, **2003**

[37] Smith, M. B.; March, J. *March's advanced chemistry,*6th ed., Wiley Interscience Inc., Hoboken: Canada, Chapter 10, paragraph 35, pp 562-565, **2007**

[38] Mendham, J.; Denney, R. C.; Barnes, J. D.; Thomas, M. J. K. *Vogel's Quantitative Chemical Analysis,*6th ed., Prentice Hall: New York, **2000**

[39] Seidl, J.; Malinsky, K.; Dusek, K.; Heitz, W. *Adv. Polym. Sci.* **1967**, 5, 113

[40] Guyot, A.; Bartholin, M. *Progr. Polym. Sci.* **1982**, 8, 277

[41] Okay, O. *Polym. Sci.* **2000**, 25, 711

[42] http://www.sigmaaldrich.com/catalog/product/sigma/m9267?lang=fr&region=FR (accessed 06.07.2013)

[43] Walker, J. R. L. *Biochem. Educ.* **1992**, *20*(1), 42

[44] Pawliszyn, J. *Sampling and Sample Preparation Techniques for Field and Laboratory*, Elsevier: Amsterdam, **2002**

[45] Poole, C. F.; Gunatilleka, A. D. ;Sethuraman, R. *J. Chromatogr. A* **2000**, 885, 17

[46] Hennion, M. C.; Cau-Dit-Coumes, C.; Pichon, V. *J. Chromatogr. A* **1998**, 823, 147

[47] Poole, C. F.; Poole, S. K.; Seibert, D. S.; Chapman, C. M. *J. Chromatogr. B* **1997***,* 689, 245

[48] Seibert, D. S.; Poole, C. F. *J. High Resolut. Chromatogr.* **1998***,* 21, 481

[49] Poole, C. F. *TrAC, Trends Anal. Chem.* **2003**, 22, 6

[50] Towler, G.; Sinnott, R. K. *Chemical Engineering Design: Principles, Practice and Economics of Plant and Process Design,* Butterworth-Heinemann: Burlington, MA, U.S.A., **2007**

[51] Hennion, M. C. *J. of Cromatogr. A.* **1999**, 856, 3

[52] Poole, C. F.; Gunatilleka, A. D.; Sethuraman, R. *J. of Cromatogr. A.* **2000**, 885, 17

[53] Bielicka-Daszkiewicz, K.; Voelkel, A. *Talanta* **2009**, *80*(2), 614

[54] Bacalum, E.; Radulescu, M.; Iorgulescu, E. E.; David, V. *Rev. Roum. Chim.* **2011,** *56*(2), 137

[55] Malik, A.; Jinno, K. *Chromatographia* **1990**, *30*(3-4), 135

[56] Erickson, H. P. *Biol. Proced. Online* **2009,** *11*(1), 32

[57] Thurman, E. M.; Mills, M. S. *Solid Phase Extraction Principles and Techniques*, John Wiley & Sons: New York, **1998**

[58] Knox, J. H.; Kaliszan, J. C. *J. Chromatogr.* **1985,** 349, 211

[59] Slaats, E.; Markovski, W.; Fekete, J.; Poppe, H. *J. Chromatogr*. **1981,** 207, 299

[60] Levin, S.; Grushka, E. *Anal. Chem*. **1989**, 61, 2428

Chapter 6: Conclusion

A general model for diameter growth and mass content during the Stöber and seed growth methods was presented in the Chapter 2. The rate of nuclei growth and minimum diameter achievable for given experimental condition were derived and the impact of operative mistakes on the solution/suspension components discussed in case of deviations from the ideal process. This offers a new way to generate diagnostic and corrective strategies and robust synthetic protocols for the synthesis of silica nano-particles. The elucidated model for the synthesis of this silica based colloidal systems has the potential to be automated with computer controlled reaction processing using automated chemical injectors/auto-samplers and on-line DLS and titration tools. The elements of novelty are the definition of a statistical model to fix reaction parameters of the Stöber method in function of the desired diameter and a way to numerically monitor the quality of the batches. Based on these two tools, the synthesis of these systems was rationalized during their planning and during the synthesis itself featuring final stock suspensions (colloid) with a rigorously defined shelf life.

The synthesis of polymer brush decorated silica nano-particles was demonstrated by ARGET ATRP grafting of poly(t-butyl methacrylate) in the Chapter 3. ATRP initiator decorated silica nano-particles were obtained using a novel trimethylsiloxane derivatised ATRP initiator obtained by click chemistry. This synthesis is fast, cheap and simple to perform and suitable for chemists not necessarily specialized in organic chemistry. These features, along with the flexibility of modifications to make other specific initiators, make this strategy different to all the other silane coupling agents used to promote ATRP processes from a silica surface. Comparison of de-grafted polymers with polymer obtained from a sacrificial initiator demonstrated good agreement up to 55 % monomer conversion. Subsequent mild de-protection of the t-butyl ester groups using phosphoric acid yielded highly colloidal and pH stable hydrophilic nano-particles comprising approximately 50 % methacrylic acid groups. The successful bio-conjugation was achieved by immobilization of Horseradish Peroxidase to the polymer brush decorated nano-particles and und the enzyme activity

demonstrated in a conversion of o-phenylene diamine dihydrochloride assay. This provides a robust protocol for the synthesis of PBMA polymer brushes on well-defined Si-NP using ARGET ATRP with high colloidal and pH stability.

In Chapter 4 an in-depth investigation of the synthesis of porous polymeric EDMA-co-GMA monoliths in an inexpensive polypropylene housing was presented. Special emphasis was given to the analysis and optimization of the anchoring layer on the PP surface that allows the formation of homogeneous monoliths fully attached to the PP wall. The SEM analysis of the final polymeric monolith demonstrated the presence of the expected globules, clusters and pores in the final monolith. The element of novelty of this chapter is the possibility to build a solid phase extraction device with simple and chip raw materials. Moreover, this device allows monitoring very easily, by ATR-IR and electronic microscopy, the chemical uniformity of the anchored polymeric solid phase and its physical continuity with the housing.

In Chapter 5, detailed and robust protocols for the synthesis of nano-brushed surface decorated EDMA-co-GMA porous polymeric monoliths were presented. In particular, a new modified encapsulation approach was used to mold the monolith. The all-in-one molding approach produces polymeric porous monoliths with stable electrostatically trapped brush nano-particles. The positive influence of the nano-brush decoration on the extraction performances (the brush enhancement factor) is introduced from geometrical considerations and then measured. A new versatile, cheap and powerful solid extraction tool is described. The element of novelty in this chapter is the use of the nano-brushes to decorate solid phase extraction porous polymeric monoliths.